Bioinspired microstructured adhesives for medical applications

Dissertation

zur Erlangung des Grades

des **Doktors der Ingenieurwissenschaften**

der Naturwissenschaftlich-Technischen Fakultät

der Universität des Saarlandes

von

Gabriela Moreira Lana

Saarbrücken, Oktober 2022

Tag des Kolloquiums:	28. Februar 2023
Dekan:	Prof. Dr. Ludger Santen
Berichterstatter:	Prof. Dr. Eduard Arzt
	Prof. Dr.-Ing. Stefan Diebels
	Prof. Dr. Alfred J. Crosby
Akad. Mitglied:	Dr.-Ing. Frank Aubertin
Vorsitz:	Prof. Dr. Roland Bennewitz

Abstract

Adhesives for interaction with human skin and tissues are needed for multiple applications, from wearable electronics to medical devices for diagnostics and therapy. Bioinspired fibrillar structures, initially developed for robotics, were upgraded for adhesion to biological surfaces to solve problems in medicine. Using a fibrillar array topped by a soft skin adhesive (SSA) layer, the film-terminated design exhibits effective adhesion to skin-like rough surfaces compared to unstructured samples. The glue-free, reliable adhesion to skin opens a large spectrum of possibilities for applications in biomedicine. Moreover, we investigated the adhesion of the microstructure to explanted mouse eardrums for application as wound dressing for eardrum perforations. The subsurface microstructure was also found to dampen any impact, protecting the sensitive membrane during application. Animal tests showed promising results to replace current surgical approaches with a less invasive and more effective treatment with microstructured adhesives.

Kurzzusammenfassung

Adhäsive für die Interaktion mit menschlicher Haut und menschlichem Gewebe werden für zahlreiche Anwendungen, von Wearables bis zu medizinischen Geräten für Diagnostik und Therapie, benötigt. Bioinspirierte fibrilläre Mikrostrukturen, die ursprünglich für die Robotik entwickelt wurden, wurden hier für die Haftung an biologischen Oberflächen weiterentwickelt, um innovative Anwendungen in der Medizin zu bieten. Unter Verwendung eines fibrillären Arrays, das mit einer Schicht aus einem weichem Polymer (SSA) bedeckt ist, zeigt das filmterminierte Design, im Vergleich zu unstrukturierten Proben, eine effektive Haftung auf hautähnlichen rauen Oberflächen. Die klebstofffreie, zuverlässige Haftung auf der Haut eröffnet ein breites Spektrum an Verwendungsmöglichkeiten in der Biomedizin. Darüber hinaus untersuchten wir die Haftung der Mikrostruktur an explantierten Maus-Trommelfellen zur Anwendung als Verschlussmaterial bei Trommelfellperforationen. Es wurde auch festgestellt, dass die Mikrostruktur unter der Deckschicht zusätzlichen Druck dämpft und die empfindliche Membran während der Applikation schützt. Tierversuche zeigten vielversprechende Ergebnisse zum Ersatz aktueller chirurgischer Eingriffe durch eine weniger invasive und effektivere Behandlung mit mikrostrukturierten Pflastern.

‘‘A few lines of reasoning can change the way we see the world..’’

Steven E. Landsburg [1]

Acknowledgments

The research that led to this thesis was conducted at the INM – Leibniz Institute for new materials, in the Functional Microstructures group, between 2019 and 2022 under the scientific guidance of Prof. Eduard Arzt.

I would like to thank all of those who supported me during this path on the dreamed career and title.

Most importantly, I would like to thank my supervisor, Prof. Eduard Arzt, for the opportunity to work in the exciting field of bioinspired materials, and for the valuable mentoring and inspiration to pursue an academic path.

I sincerely thank Klaus Kruttwig, who supervised the first half of my Ph.D., for the energic and motivating work environment, and from whom I learned a lot about developing a medical product. For the supervision of the final stages of my work and the rich scientific insights, I would like to thank René Hensel and Xuan Zhang. It was a pleasure learning from all of you.

I am pleased for all my time at the institute and for the colleagues and friends I have encountered over the last few years. To Peter Oliveira, who gave me the opportunity to join the INM back in 2016, I am grateful for the opportunity and the trust. A special thanks to Katharina Sorg for the great teamwork. And also thank you to the team of the “eardrum project”, Angela Rutz, Gisela Heppe, and Pamela Kalmes, I enjoyed our work and time spent together. To Christian Müller, I am grateful for the rich discussions that turned out to be such an important contribution to my work. And to the students that I had the pleasure to supervise, Julian Weiss and Isaac Blaya.

I also would like to acknowledge my dear FM colleagues, Joachim Blau, Yue Wang, Fabian Faller, Haocheng Quan, Shirui Zhang, Lena Barnefske, Andreas Weyand, Marius Weiler, and Sylvia de Graaf. To the colleagues from other groups at INM, always ready to help, thank you to Peter König, Petra Herbeck-Engel, Bruno Schäfer, Dirk Beckelman, Marlon Jochum, and Robert Drumm. Thank you to Prof. Anette Kraegeloh, Yannic Brasse, and Silke Kiefer for

their support in the biological experiments. I also would like to thank my colleagues in Homburg for the great project we conducted together and their receptiveness, Prof. Bernhard Schick, Prof. Gentiana Wenzel, and Larissa Schatteburg.

Finally, to Henrique, my greatest motivator, and to my family, for the utmost love.

Abbreviations and Symbols

Materials and material properties

ETO	Ethylene oxide
HA	Hyaluronic acid
PCL	Poly(caprolactone)
PDMS	Polydimethylsiloxane
PET	Polyethylene terephthalate
PLA	Poly(lactic acid)
PSA	Pressure-sensitive adhesives
SSA	Soft skin adhesive

Theory and definitions

CON	Control sample
ECG	Electrocardiogram
ENT	Otolaryngology (Ear, nose and throat speciality)
EVR	Epoxy Vitroskin rough
FT	Film-terminated microstructure
JKR	Johnson-Kendall-Roberts theory
M	Malleus
PF	*Pars flaccida*
PSD	Power spectrum density
PT	*Pars tensa*
TM	Tympanic membrane
TMP	Tympanic membrane perforations
U	Umbo
VdW	Van der Waals

Methods

ABR	Auditory brain response
AFM	Atomic force microscopy
ANOVA	Analysis of variance
DPOAE	Distortion product otoacoustic emissions
FE, FEM	Finite element method
FEA	Finite element analysis
SEM	Scanning electron microscope

Parameters

C	System compliance
C(q)	Power spectral density
D	Fibril diameter

E	Young's Modulus
E*	Effective modulus
f	Frequency
F_{peel}	Peel force
G, G'	Storage modulus
G''	Loss modulus
h	Fibril height
H	Hurst exponent or roughness scaling factor
h(x)	Height of a surface at a point x(x,y)
h_{film}	Sample/film thickness
I	Second moment of inertia of a circular pillar
L	Sound level
n	Number of fibrils
n.s.	Non-significant
P	Normal contact pressure between surfaces
p	p-value, statistics variable
P_b	Euler's critical buckling load
q	Wavevector, defined by $q=2\pi/\lambda$
R	Fibril radius
R_a	Arithmetic average height (roughness)
R_q	Root mean square roughness
R_z	Mean peak-to-valley distance (roughness)
s	Displacement of pivotable table
tan δ	Damping factor
ũ	Displacement amplitude
V_{el}	Energy of elastic deformation
α	Constant depending on boundary conditions
θ	Peel angle
λ	Surface wavelength
μ	Friction penalty coefficient
ν	Poisson ratio
τ_{fric}	Maximum friction stress

Contributions of Co-authors

Details of the contributions of all co-authors to the individual chapters are acknowledged. Chapters 4 and 5 were published in peer-reviewed journals. Chapter 6 was a patent granted by the DPMA (German Patent and Trade Mark Office).

Chapter 4

Moreira Lana, G.; Zhang, X.; Müller, C.; Hensel, R.; Arzt, E. Film-terminated fibrillar microstructures with improved adhesion on skin-like surfaces. ACS Applied materials & interfaces, 2022

The publication is an open access article published under an ACS AuthorChoice License, which permits copying and redistribution of the article or any adaptations for non-commercial purposes. The article is available under:
https://pubs.acs.org/doi/10.1021/acsami.2c12663

Enquiries about the permissions related to the content of the publications should be directed to ACS.

Authors contributions: Conceptualization G.M.L., X.Z., R. H., E.A.; Sample fabrication, adhesion measurements, microscopy G.M.L.; Establishment of simulation model X.Z.; Writing – original draft G.M.L., X.Z., C. M.; Review and editing – G.M.L., X.Z., C.M., R. H., E.A. The manuscript was written through contributions of all authors. All authors have given approval to the final version of the manuscript.

Acknowledgements: The authors thank Klaus Kruttwig for discussions in the pre-conceptualization and the previous work on film-terminated microstructures. Lars Pastewka is thanked for helpful discussion on the roughness and power spectrum analysis. Martin Müser is acknowledged for valuable input on the analytical discussions. Yue Wang and Julian Weiß are thanked for fabrication of rough surfaces. Joachim Blau is thanked for building the adhesion measurement setup. The authors thank Biesterfeld Spezialchemie GmbH (Hamburg, Germany) for providing polymers. Dr. Xuan Zhang acknowledges support by a Humboldt Research Fellowship for Postdocs. The research leading to these results has received funding from the European Research Council under the European Union's HORIZON-EU.1.1 program/ ERC PoC Grant Agreement No. 842 613, Advanced Grant “Stick2Heal” to E.A.

Chapter 5

Moreira Lana, G.; Sorg, K.; Wenzel, G. I.; Hecker, D.; Hensel, R.; Schick, B.; Kruttwig, K.; Arzt, E. Self-adhesive silicone microstructures for the treatment of tympanic membrane perforations. Adv. NanoBiomed Res. 2021, 1, 2100057.

This is an open access article under the terms of the Creative Commons Attribution License, which permits use, distribution and reproduction in any medium, provided the original work is properly cited. The article is available under:
https://onlinelibrary.wiley.com/doi/10.1002/anbr.202100057

Copyright Wiley-VCH Verlag GmbH & Co. KGaA. Reproduced with permission.

Authors contributions: G.M.L. and K.S. contributed equally to this work. Conceptualization G.M.L., K.S., G.I.W., K.K., E.A.; Roughness and adhesion investigation G.M.L.; Ex-situ adhesion investigation G.M.L., K.S., K.K.; Hearing investigation K.S., K.K.; Statistical analysis K.S.; Writing – original draft: G.M.L., K.S. Writing: – Review and editing: G.M.L., K.S., G.I.W, D.H., R.H., K.K., B.S., E.A.

Acknowledgments: The authors acknowledge Joachim Blau for technical support and for designing the ex vivo measurement setup. Julian Weiß is acknowledged for confocal microscopy measurements and Dr. Lena Barnefske for the microfabrication of the master structures. Dr. Xuan Zhang is thanked for the support in mechanical calculations and Angela Rutz, for her laboratory assistance. The authors thank Biesterfeld Spezialchemie GmbH (Hamburg, Germany) for providing the polymers and Isaac Ayala Design for the design of the schematic TM graphic shown in Figure 2. The research leading to these results has received funding from the European Research Council under the European Union's HORIZON2020– EU.1.1 program/ ERC PoC Grant Agreement No. 842 613, Advanced Grant "Stick2Heal" to E.A.

Chapter 6

This chapter was published on 25.08.2022 under the international publication number WO002022175150A1 at the German Patent and Trade Mark Office: "Krafttollerante Struktur" DE 102021103895 A1, Offenlegungsdatum 18.08.2022 Prioritätsdatum 18.02.2021

The inventors are: Kruttwig, K.; Moreira Lana, G.; Moh, K.; Arzt, E.

Table of Contents

Chapter 1. Introduction

Adhesion is a vast subject involved in most theoretical and applied fields, from molecular interaction to materials formulation, design, and structural engineering. The importance of adhesion forces is also easily found in micro- and nano-level mechanical, electrical, electronic, and optical devices; and in biological systems, cell structure and interactions, transport, cell division, and colloidal systems.[2] [3]

Natural structures from animals like geckos and ladybugs have inspired the development of new technologies for dry, reversible adhesion. With hierarchically built fibrillar structures at the tip of the toes, geckos can climb on various surfaces. In recent years, artificial ‘‘Gecko adhesives’’ have already been successfully applied in industrial robots and handling systems, and their adhesion mechanism has been widely explored in the literature.[4] [5] We propose using such microstructuring solutions to solve problems in a far more complex and exigent environment: the human body.

Adhesives in medicine and healthcare are needed for multiple applications, from external use, such as for wearable electronics, to those requiring contact with open wounds or for internal medicine, for instance, in sutures, wound dressing, and many sensors. As indicated in Figure 1, the rising global market for medical adhesives[6] indicates the increasing demand for attachable devices with reliable yet delicate interactions with biological surfaces. [7]

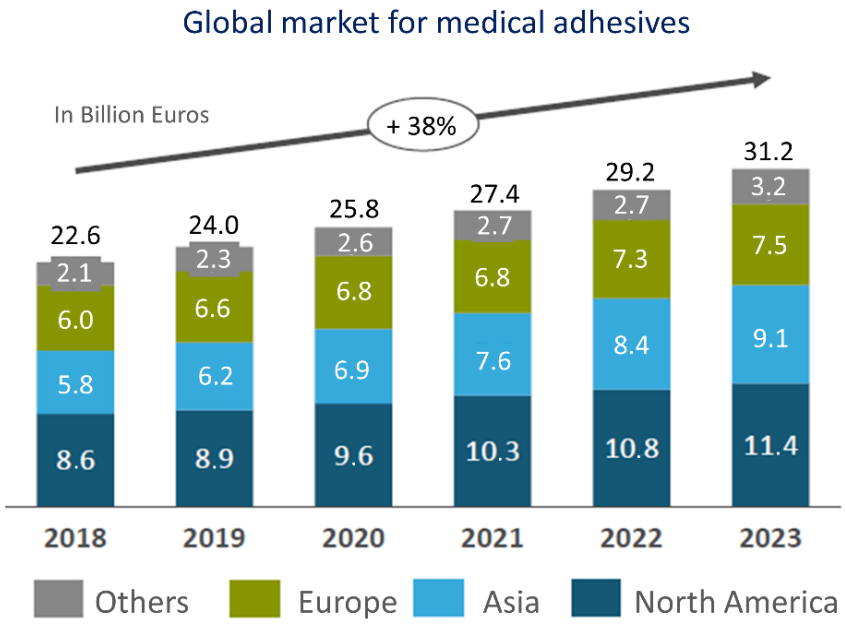

Figure 1.1: Global Market for medical adhesives. Adapted from [6]

As biological structures are complex surfaces to stick to, microstructured adhesives have been gaining space as they can compensate for this complexity through highly compliant designs. Also, they offer a solution that relies only on physical interactions, therefore not leaving residues and avoiding damage and allergic reactions, common issues when it comes to chemical adhesives.[8]

This work aims to investigate biomedical microstructured adhesives on two fronts: adhesion to highly rough surfaces as the skin, and patches for the treatment of eardrum perforations.

The skin was taken as a reference for investigating microstructured adhesives on complex surfaces. A precise grasp of the effect of adhesion on the skin opens a large spectrum of applications in biomedicine. Chapter 4 investigated the adhesion of a fibrillar microstructure terminated by a soft, continuous layer on different rough surfaces. The improved adhesion of such design on skin-like roughness was demonstrated and, supported by FEM simulations, a model was presented to understand its contact formation and detachment and why it is advantageous compared to equivalent unstructured control samples.

The second application, the treatment of eardrum perforations, presented in Chapter 5, tackles a recurrent medical issue that requires a more efficient and less invasive alternative. A self-adhesive patch is presented to support wound healing without the need to pack the outer ear canal, the current state of the art for treating this pathology. A reliable adhesion is achieved using the film-terminated design, which offers additional advantages: (i) a safety mechanism of the microstructure that protects the eardrum against further damage; (ii) immediate closure of the wound through the continuous terminal layer, protecting the middle ear against the entrance of pathogens; and (iii) immediate improvement of hearing function (tested *in vivo*).

Lastly, Chapter 6 discloses the mentioned safety mechanism of the fibrillar microstructure with a terminating layer. The effect was observed by applying a compressive load; through buckling, the fibrils avoid the transference of force directly to the countersurface without loss in adhesion performance.

Solutions for two biomedical applications using bioinspired microstructured dry adhesives are presented. The first branch contributes to a deep understanding of the mechanics of adhesion on rough, skin-like surfaces and proposes a viable system for skin adhesives. The second application of this thesis provided a substantial contribution to the translation phase of the eardrum patches to clinical applications.

Chapter 2. Literature Background

This section provides an insight into the state of the art of bioinspired microstructured adhesives and medical applications of such structures, focusing on two cases: application to skin and treatment of eardrum perforations. Accordingly, we present a background on bioinspired adhesive systems and the related mechanics, followed by the motivation behind the mentioned applications in biomedicine.

2.1 Bioinspired adhesive microstructures

Millions of years of evolution and natural selection have led to structures found in nature to reach very efficient designs for reduced drag underwater,[9] [10] self-cleaning,[11] flight, [12] penetration,[13] and reversible adhesion.[14] [15] [16] Many of those properties are achieved due to intricate surface patterns, which have inspired scientists in the last decades to create and improve a material's functionalities by changing its architecture.[4]

Adhesion in nature can be found in various forms. For the purpose of this work, we will go into detail on reversible, temporary forms of attachment inspired by biological systems.

The fascinating ability of insects, spiders, and lizards to climb walls and ceilings of different compositions and textures puzzled observers for centuries. In the early 2000s, Autumn and co-workers[15] explained, based on experiments, that this effect is due to finely structured elements at the tips of the locomotion parts.[16] This observation motivated the development of artificial systems based on microfibrils, which interestingly create sticky surfaces out of intrinsically non-sticky materials.

Similarly to the gecko multiple setae, bioinspired fibrillar adhesives have the contact surface split into many individual contacts, enabling intimate interaction with the surface and enhancing adhesion through short-range van der Waals forces.[17–19] Such physical interactions are unspecific and, to some extent, insensitive to surface chemistry. The advantage of smaller contact elements was described by both Hertzian[20] and the Johnson-Kendall-Roberts (JKR)[21] theories in the late 1970s and 80s.[3] Yao and Gao[22] later combined those theories to explain the interaction and local elastic deformation of two spherical surfaces brought into contact

under loading and basically state that adhesion strength scales inversely with the radius of the spheres. A further point brought by their solution, which is relevant to this work, is that softer microstructures might be advantageous in the case of lower contact areas, i.e., rough surfaces.

In addition to facilitating physical interactions with the countersurface, split contact requires the interface crack to re-initiate at each subsequent fibril, which also accounts for improved adhesion. This effect of intermittent propagation and arrest of the crack front is known as crack trapping.[23] More specifically, such effects of contact formation and fracture mechanics can be tuned by design and experimental conditions at the fibril level (size,[22] aspect ratio,[24–26] shape,[27] elastic modulus,[28] humidity[29,30]) and the array level (backing layer,[31] preload,[32] spacing). Variations of the simple fibrillar design to further improve adhesion or add other functionalities include softer tips,[33 34] mushroom,[35,36] cup,[37–39] spatulae or slanted shapes,[40] and termination using an intermittent[41] or continuous layer.[42] The latter is also helpful when limitations of an array of fibrils arise, such as a drop in adhesion through buckling and lateral collapse of fibrils.

Besides split contact to increase adhesion and obstruction of crack propagation, microstructured surfaces present a lower effective Young's modulus, which increases compliance to rough surfaces,[43] conforming to different degrees of bumpiness with less strain energy penalty.[44 45] This effect can also be obtained by making the fibrils small enough[46] or creating an elastic modulus gradient (i.e., softer tips).[47 48] That way, materials that are a priori, relatively stiff can go below Dahlquist's criterion for stickiness and conform to different surfaces.[49] This criterion describes that soft materials stick by simple contact below a modulus threshold of 100 kPa measured at 1Hz.[50 51]

In this work, a film-terminated fibrillar design was identified as a promising alternative for adhesion to rough surfaces, particularly due to a more distinct intimate contact surface attributed to both local and global compliance of the microstructure. The system, introduced by Glassmaker in 2006,[42] consists of terminating a fibrillar array using a continuous layer. The Jagota Group explored the use of this microstructure for enhanced friction[52 53] and adhesion to smooth[54 55 56] and rough surfaces,[57] using a terminal layer of the same material as the

fibrils. Later, the Group of Boxin Zhao published studies of the film-terminated design using a soft terminal layer.[58] [59] The hybrid graded structure is able to combine contributions from the soft film and the elastic fibrillar array. However, the authors introduced a softer material by changing the mixing ratio of the polymer, which can be critical in our case of interest: medical applications. By doing so, composition deviates from the standard defined by the manufacturer, making the changes in reactivity and curing conditions hard to predict. Hence, in this work, to create the graded structure we used a certified biomedical material that already have lower Young's modulus with the approved composition.

Crack trapping is the main tenet attributed to the adhesion performance of film-terminated microstructures. The local stress energy release rate becomes a periodic function due to the absorption of energy by the microstructure during retraction, followed by sudden energy release when the crack propagates to where the next fibril is positioned.[41,42] The energy is at its minimum when the detachment front is located between the fibrils, where the crack is "trapped".[54]

Allied to the crack trapping effect, the subsurface microstructure is responsible for an effect called "contact pinning". It means that, in an adhesion experiment, the contact does not immediately start to decrease while retracting the countersurface, as it occurs in unstructured samples. In fact, the deformation of the fibrils underneath the film "pins" the contact area while absorbing the energy, which increases the pull-off force and work of separation.[42] Fibrillar spacing influences both effects (crack trapping and contact pinning) in the sense that it changes the rate in crack advance, although it does not necessarily improve adhesion performance. [54]

To set the stage for the discussion on how microstructured adhesives can be applied in medicine, it is important to understand how adhesion is measured and what parameters might influence adhesion data. Several methods can be used to this end, the most common being peel and normal tack test.

2.1.1 Adhesion testing

A peel test is based on a thin adhesive strip backed with a stiff layer peeled at a constant velocity by a force F_{peel}, usually from a rigid substrate, as presented in Figure 2.1a. It is a standard test in the industry, performed at a constant peel angle θ (90° or 180°), and can be useful to study steady-state propagation. However, it is affected by the bending stiffness and deformability of the adhesive and is limited in cases of more complex geometries.[60]

The normal tack test, used in this work, provides different information on the adhesive. It consists of compressing the specimen with the desired substrate until a certain load, holding them in contact then retracting the substrate in the normal direction, as presented in Figure 2.1b. Information such as pull-off stress (maximum force measured during retraction, divided by the area of the surface) and work of separation (area under the stress-displacement curve) is obtained.[60] The displacement is corrected with the machine's compliance to compensate for the eventual elastic deformation of the equipment's parts.[61 62] A schematic representation of the measuring setup is presented in Figure 2.1c. Force and displacement (s) are recorded during the measurement.[63]

The substrates used as countersurface can vary in material, roughness, and geometry. We used randomly rough or model designs, but all nominally flat surfaces. Many reports in the literature use spherical substrates, although tack testing with spherical objects is basically turning the normal tack test into a peeling test. [4] Besides the indentation object, other testing conditions affect the adhesion data, such as compressive preload, retraction speed[54 64] and time in contact with the object.[65 66] Those parameters are even more relevant if a viscoelastic material is used.[67]

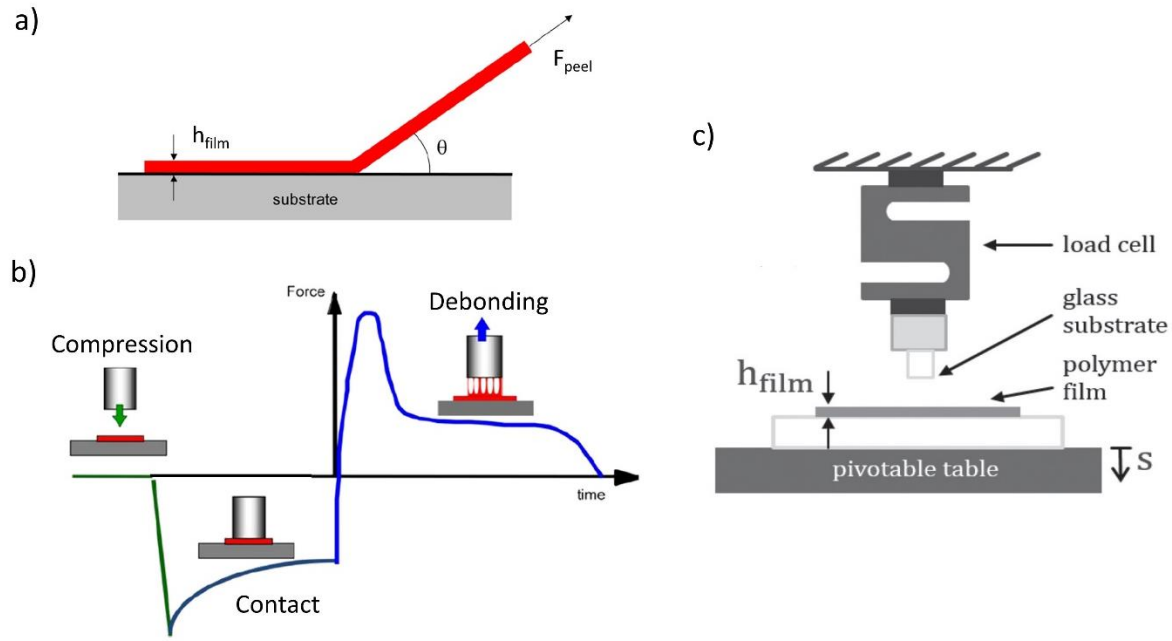

Figure 2.1: Schematic representation of adhesion tests. a) Peel test, b) Normal tack test performed with a flat probe.[60] *c) Measuring setup for tack tests. h is the sample thickness and s is the displacement of the pivotable table.*[63]

The obtained results for both peel and tack tests provide global results about the system (adhesive, countersurface, and testing conditions) but do not reveal details about the debonding mechanism.[60] For a detailed understanding of contact formation and detachment mechanisms, in addition to experimental data, other scientific tools can be used, such as FE simulations and theoretical models, as we propose in chapter 4 of this work.

Bae and co-workers[41] describe the difference between tack and peel mechanisms for a film-terminated design, as presented in Figure 2.2. The authors describe that, by pulling the adhesive in the normal direction, a higher adhesion force can be obtained due to crack trapping between the fibrils; on the other hand, peeling the adhesive facilitates the crack propagation through the layer that bridges the fibrils. Still, a higher adhesive force on a smooth surface was measured compared to the simple fibrillar structure.

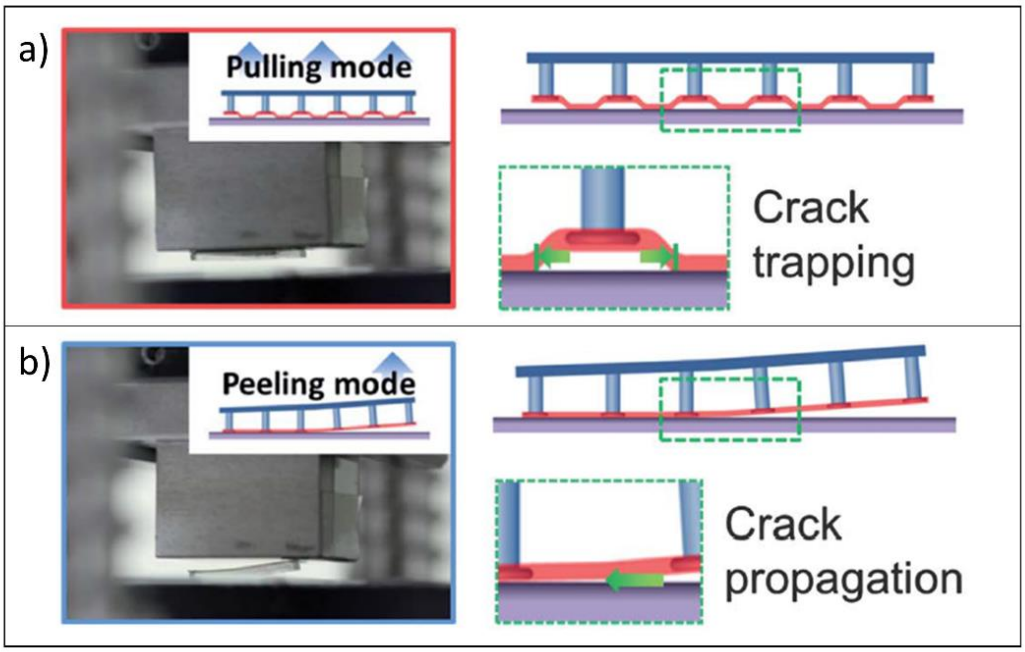

Figure 2.2: Film-terminated design submitted to normal (a) and peel (b) pull-off modes, and respective detachment mechanisms. Adapted from [41]

2.2 Medical adhesives

Adhesives in medicine are needed for many applications. The first sticky plaster that comes to mind is the Band-Aid, a simple combination of rubber adhesive and fabric used to treat minor wounds, first developed in the early 1920s.[8] More critical wound dressings needed for burn treatment and drug delivery are more complex regarding design and material. Some challenges for these materials that have direct contact with wounds and exposed tissues are secondary damages, cytotoxicity, insufficient adhesion, undesired degradation, and allergic reactions. [68]

For external use, devices that go in contact with skin are used for sports, for the fixation of devices and sensors, or new generation wearable electronics.[69–75] In this case, adhesion must be high enough to secure the device, but remain under a maximum threshold to avoid damaging the skin.[7]

This work explored two medical applications: adhesion to the skin, within which a new variety of applications arise, and an adhesive patch as wound dressing for eardrum perforations.

2.2.1 Skin applications and its challenging surface properties

The human skin is composed of three layers: the epidermis, dermis, and hypodermis, and it has a variable thickness of around 60-100 μm.[76 77] The dermis is primarily composed of elastin and collagen, the latter being the source of the skin's elastic properties.[78] The epidermis, the most external layer, is also composed of different tiers, being the stratum corneum the outer one, responsible for the barrier function and prevention of unregulated water loss.[79] The barrier function is attributed to the tight, multi-layered composition of cells and lipids that provides a tough and resilient structure.[80]

Disruption to the barrier function can occur by damage through tape-stripping, some skin diseases (e.g., psoriasis and dermatitis[80]), and burns, which can be a life-threatening condition, depending on the extension of the skin surface affected. In critical circumstances, the survival rate can be increased by applying an artificial barrier to the burnt area.[81] The goal of burn dressings and other wound bandages is to prepare the area for healing and control the growth of microorganisms to avoid infections. In some cases, growth factors or drugs are integrated to wound dressing to make the process more efficient and reduce the discomfort to the patient.[81]

Other applications of adhesives that go in contact with the skin are used for the affixation of devices such as ostomy bags,[82,83] sensors such as ECG (electrocardiogram)[75] and oximeter (oxygen saturation),[84,85] or wearable electronics for health monitoring in daily life.[74 86–88] Although essential, monitoring systems usually have low patient acceptance, low accuracy and reliability, as they are typically bulky, wired devices that often require conductive gels[89] and clamping mechanisms. Extensive effort to overcome such problems has been done in soft bioelectronics in the past years[69,88,90–92] but are beyond the scope of this work.

Currently, skin patches are generally based on PSAs (pressure-sensitive adhesives), of which low Young's modulus and viscoelasticity combine fluid behavior for bonding and solid

behavior for debonding resistance. However, their too strong adhesion often causes damage to the skin in the removal process. Moreover, they are designed for single use and leave residues on the skin.[7] They are particularly problematic in adhesives for delicate skin, such as those of the elderly and newborns, as their fragile skin is more susceptible to tear and irritation.[8 93 94]

Thereby, bioinspired microstructures with tunable dry adhesion arise as a promising solution. Kwak et al. pioneered this idea by presenting fibrillar microstructures with up to 15 kPa adhesion to skin. [95] Compared to rigid surfaces, adhesion to skin was around two orders of magnitude inferior but enough to hold ECG sensors for two days.

Many medical adhesives interact with skin; still, it is a challenging surface when it comes to adhesion, especially when a sensitive, controlled, and tunable bonding is needed. In addition to being a dynamic surface, it has many complex properties: multiscale roughness, the presence of hairs, follicles, impurities, fluids (e.g., sweat, oil), etc.[7] Roughness, viscoelasticity, and humidity will be discussed in turn.

a. Roughness

Roughness is a classic restrictive factor for dry adhesion, even on a small scale,[96] as it reduces effective contact area,[43] hindering short-range interactions.[2 45] It is also very relevant in other scientific and engineering fields, such as friction, wear, and biocompatibility.[97]

Surface topography is expressed as roughness, waviness, and form, [98] as represented in Figure 2.3a. It can be characterized using two-dimensional methods, such as profilometry, or three-dimensional approaches, such as atomic force microscopy (AFM) or confocal microscopy. For a comprehensive characterization, some methods are even combined and expressed as a 3D reconstruction or a solution based on multiple descriptors.[97 99]

Different descriptive parameters can be obtained from those measuring methods. Some of those parameters,[100] most found in the literature, are schematically represented in Figure 2.3b:[101]

- Arithmetic average height (R_a): also known as center line average, is the average of the absolute deviation of the roughness. Gives a good description of height variations but not wavelength.
- Root mean square roughness (R_q): also designated RMS, indicates the standard deviation of the height distribution R_a.
- Mean peak-to-valley distance (R_z): gives the average summation of the highest peaks and lowest valleys.

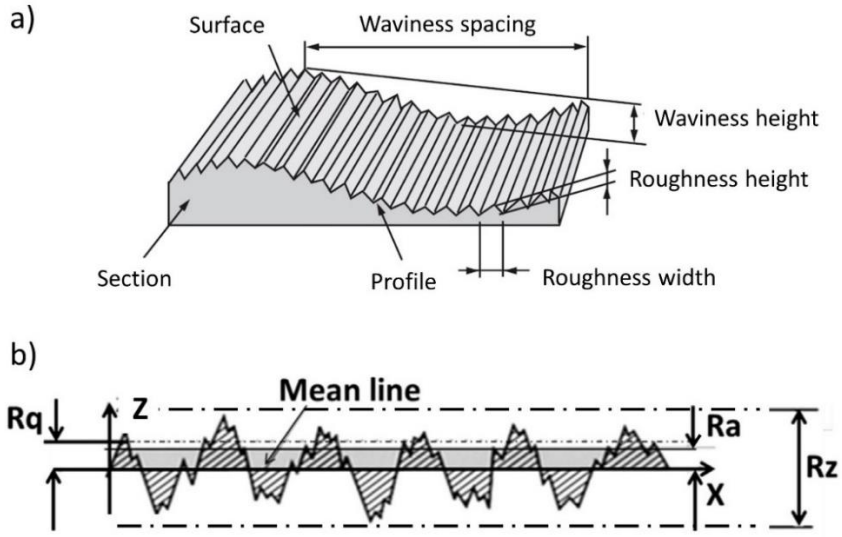

Figure 2.3: Schematic representation of roughness. a) Surface structure with roughness, waviness and form. Adapted from [98] *b) Surface roughness parameters R_a, R_q and R_z. Adapted from* [101]

Parameters that rely only on height for roughness information, such as those listed above, give a fundamental insight about the surface but might not be enough to describe some areal contacts. Albeit more demanding, power spectrum density (PSD) is one of the most far-reaching roughness descriptors, as it captures more of the surface features at its complexity. It is defined mathematically by the Fourier transform, assuming the rough surface as a superposition of sin waves with different wavelengths. As presented in Equation 1, it describes the height $h(x)$ of a surface at each point $x(x, y)$, as a function of the wavevector q.[43,102,103] The magnitude of the wavevector, in turn, is defined by $q = 2\pi/\lambda$.

$$C(q) = \frac{1}{(2\pi)^2} \int d^2x \langle h(x)h(0) \rangle \, e^{-iqx} \quad (1)$$

Considering a self-affined surface (i.e. a fractal pattern that repeats itself in different scales), the power spectrum behaves as a power law, as expressed in Equation 2.

$$C(q) \approx q^{-2(H+1)} \quad (2)$$

H is the Hurst exponent, or the roughness scaling factor. H below 0.5 indicates more continuous features, while $0.5 < H < 1$ suggests a more inhomogeneous roughness distribution, i.e., abrupt value changes along the surface.[104]

The roughness power spectrum is important to define which wave vectors contribute to adhesion since elastic energy to conform two surfaces is dominated by larger wavelength undulations, namely smaller q (for the case of $0.5 < H < 1$).[105 106]

Skin roughness can be measured using different measuring methods and parameters. Also, skin is susceptible to variations by aging, body location, environmental conditions, and skin diseases.[77] Using combined methods, Kovalev and co-workers defined the power spectrum of the skin roughness of a wrist, with wavevector from 10^3 m^{-1} to 10^{10} m^{-1}. A corresponding R_{ms} roughness amplitude is circa 22 μm.[107]

Trojan et al.[77] and Kottner et al.[108] measured R_z of around 60 to 70 μm using a non-contact optical method on forearm sites. Both studies' R_a data is distinct, around 38-46 μm and 7 μm, respectively. Aged skin is reported to be rougher and more heterogeneous.[77] Bloemen and colleagues[109] report even higher variance of scarred tissue on different locations, R_z = 267 ± 90.3 μm and R_a = 19.6 ±5.4 μm.

Barreau and co-workers correlated fibrillar adhesion to surface roughness. Fibril diameter should be small to take advantage of the contact splitting effect, but not smaller than the mean spacing between the surfaces' protrusions.[110]

A useful artificial model to investigate skin surface used in the literature is the Vitroskin,[111] which has roughness R_a = 13.55 μm and R_z = 84.2 μm. Respective epoxy replica of such surface presents R_a = 9.48 μm and R_z = 49.66 μm; the difference to the original surface is attributed to materials shrinkage.[112]

b. Viscoelasticity

Viscoelasticity refers to materials with both elastic and viscous character. Hence, those materials are defined by two moduli: storage modulus (G', elastic component), and loss modulus (G'', viscous component).[113,114]

Skin presents complex non-linear viscoelastic and anisotropic properties.[115] It depends on the thickness of the epidermal layer and stratum corneum, as well as the deformation behavior of the different anatomical sites. For example, mechanical properties vary in a stretched or flexed arm, leading to a change of up to 25% of induced strain.[76] The non-linear behavior is characterized by the fact that, under low applied load, a large deformation occurs, followed by an increased stiffness due to the alignment of the collagen fibers.[116,117]

Although studies of human skin have been extensively described in the literature, many consider the individual skin layer separately[118,119] or are performed ex vivo on excised skin.[115] [117] These results are helpful for a scientific insight into the mechanical behavior of skin but can deviate considerably among them and from real applications. Different testing techniques (tension,[120] [117] indentation,[121] shear[115]) or sampling factors (anatomical position,[122] hydration,[107] gender,[122] and age[13] [123]) contribute to the spread data found in the literature. Moreover, although described as viscoelastic, mechanical studies of skin report only elastic properties, as the following examples.

Regarding different body parts, for instance, the elastic modulus of excised back skin, measured by tensile tests, is reported by Annaidh et al.[117] to be 83.3 ± 34.9 MPa. In comparison, excised forehead skin was evaluated using tensile tests by Jacquemoud et al.[124] and presented a modulus of 3MPa ± 1.5 MPa.

Studies performed *in vivo* present significant variations expected for biological, complex specimens. Yet, given the particularities of each application, they can represent the heterogeneous character of the skin in real conditions with more veracity.

Tensile measurements in forearms[125] indicate Young's modulus of about 350-500 kPa. Indentation tests present an advantage, compared to tensile tests, that it does not require pre-stressing the skin and allows the determination of bulk properties.[121] Using indentation methods, Young's modulus assessment of forearm skin range between 4.5 and 8 kPa,[121] while reports of aged skin (55-70 years), on forearms,[13] give 8.5 $\pm$ 1.4 kPa. Elastic modulus is known to increase with age, as a consequence of the reduced capacity of deformation due to less collagen.[123] Investigation of mushroom-shaped polyurethane microstructure adhering to a flat, compliant surface show improved adhesion compared to stiff surfaces.[126]

c. Humidity

Humidity affects skin properties directly, as it can absorb water and swell. It can stem from the environment, sweat, or moisturizing creams. Moreover, unabsorbed water at the surface (e.g., air humidity above 55%) serves as lubricant making it slippery.[111]

Increasing water content on the skin decreases its elastic modulus; Kovalev et al.[107] report *in vivo* Young's modulus of human wrist of 7 MPa in wet state and 1 GPa in dry state. As for the texture, moisture is reported to decrease skin roughness.[111] Therefore, it affects the contact mechanics and, consequently, the adhesion. Moreover, while the water evaporates, changes in capillarity and friction arise.

Mechanical strength is also compromised in the presence of humidity. Hydrated skin has reduced delamination energy for debonding cells, a process known as "desquamation".[13] For example, this can be problematic in case of moisture trapped under a skin adhesive.

In a situation of fibrillar structures adhering to smooth surfaces, the additional effect of humidity generates capillary forces in addition to the van der Waals interactions.[8 127] It differs

from underwater adhesion though, in which van der Waals interactions are strongly reduced and suction effects become dominant.[4] [128]

Examples of changes in adhesion to skin surfaces due to the presence of humidity are reported in the literature.[129] [130] The presence of humidity should be considered with caution. Regarding the complexity of attachment to biological tissues, properties are interconnected, so each case should be evaluated to determine if humidity will be a factor in increasing or hindering adhesion.

To overcome effects caused by skin humidity, the Karp group reported strong adhesion of fibrils to both dry and wet tissues by adding a thin layer of biodegradable tissue-reactive glue (dextran) over the fibrillar array. [131] Similarly, Lee and co-workers present a PDMS fibrillar structure coated with poly(dopamine methacrylamide-co-methoxyethyl acrylate) for chemical adhesion to wet surfaces.[132] However, such solutions would leave residues on the surface.

Other residue-free, bioinspired solutions for wet environments come from cephalopod micro-suction cups. Baik and co-workers report robust adhesion to pig skin (≈25 kPa) and even wet wounds using dome-like protuberances.[133]

2.2.2 Eardrum perforation and therapeutic approaches

A second medical application addressed in this work is the treatment of eardrum perforations. The tympanic membrane (TM), commonly known as the eardrum, is a thin tissue that separates the middle ear from the outer environment, as presented in Figure 3. It is responsible for capturing external sound waves and transforming them into mechanical motion for the hearing process. The vibrations are subsequently transmitted through the ossicular chain (malleus, incus, and stapes) to the cochlea in the electro-mechanical sensory system in the inner ear.[134]

The human TM consists of an oval, cone-shaped structure of around 8-10 mm in diameter, and it has an angle of 132-137° at its apex, where the membrane is affixed to the ossicular

chain through the manubrium ("handle") of the first ossicle, the malleus.[135] The membrane is composed of a tri-laminar epithelial tissue. One of the layers (lamina propria) is formed of a vascularized intricate collagen network with radial, circumferential and parabolic orientations, as indicated in Figure 3b. It is divided into two regions: the *pars flaccida*, a slack region in the superior part of the TM, and the *pars tensa*, the major portion that is firmly anchored to the surrounding bone and, therefore, more stretched. The membrane presents different thicknesses and elastic properties in different zones, critical factors for vibrational properties and, consequently, for hearing function. Although precise characterization is complex, due to measuring methods and variability between individuals, an acceptable average of the *pars tensa* thickness lies between 80 and 110 μm.[135] [136]

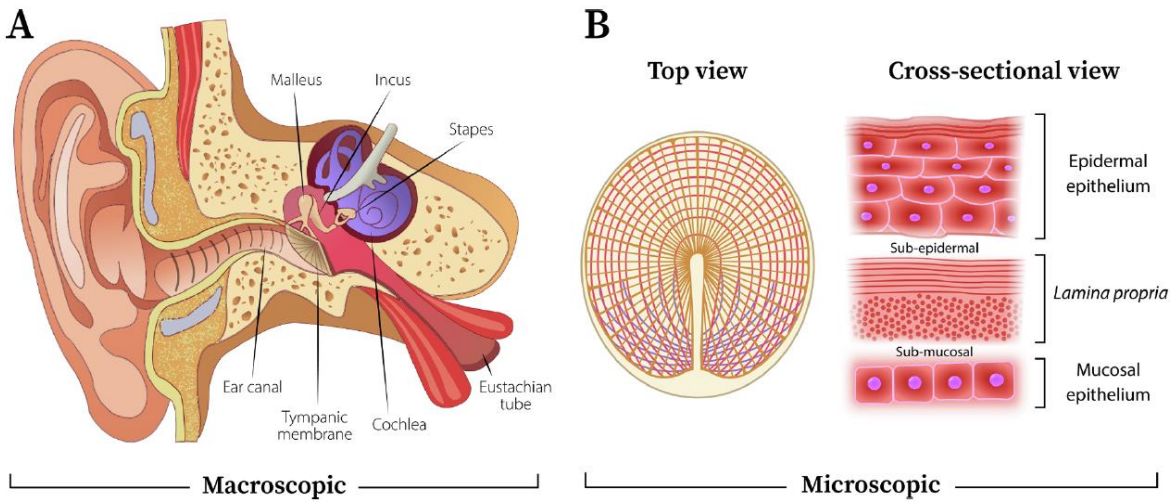

Figure 2.4: Schematic representation of the hearing system (a) and the eardrum structure in top and cross-section view. Adapted from [134]

Tympanic membrane perforations (TMP) are the most common damage to the human ear and can be caused by infections, trauma, rapid pressure changes, or insertion of foreign bodies through the ear canal.[137,138] TMPs have a direct impact on the hearing function as the sound conducting mechanism created by the TM is strictly diminished by the perforation.[139] The TM has an inherent ability to heal itself in a substantial proportion of acute cases, but chronic lesions and large perforations[140] require a surgical approach. [138]

An injured tissue typically undergoes several stages for healing that can be simplified into inflammation, proliferation, and remodeling.[141] For most tissues, the proliferation only takes place after the formation of a granulation tissue bed, an anchorage protein network that serves as a platform for cell growth and reepithelization. For the eardrum, however, in the case of extensive injuries and chronic cases, tangible support to bridge the wound is nonexistent, hindering the necessary cell migration and proliferation.[138 142 143] Even in cases of spontaneously healed TMs, the newly formed membrane might not be optimal, causing acoustic deficiency and being more susceptible to the formation of retraction pockets and reperforation.[144] Thus, reconstructive options are needed in various cases.

If untreated, TMPs cause foremost conductive hearing loss, tinnitus and infections in the middle ear due to entrance of pathogens. In more severe cases, it can cause life-threatening conditions such as cholesteatoma (an abnormal growth of epithelial tissue from the TM that can erode the bones in the middle ear and infiltrate the inner ear and hearing nerve, inducing the need for complex surgery) and extended complications to the brain. Long-term, impaired hearing has more far-reaching consequences, such as diminished quality of life and mental health [145], affected speech and socialization.

Tympanoplasty is the standard procedure to provide the needed support for the migrating epithelium of an injured eardrum and overcome the conductive hearing loss by patching the perforation. Tympanoplasty type I (also called myringoplasty), is performed in case of small TMPs if the perforation is not affecting the ossicular chain. It consists of applying a grafting material to the perforation. It is done under local anesthesia, and the graft (typically a silicone foil) is kept in position by packing the outer ear canal with cotton. In case of larger perforations, i.e., the erosion reached the ossicular chain, a more complex reconstruction called tympanoplasty type II-IV is needed. [146]

There are many studies on tympanoplasty introducing novel techniques and a variety of graft types available.[137,147–151] The most common autologous grafts are temporalis fascia and perichondrium, [137,148] which are parts of the patient's own connective tissue.

Grafting with autologous tissue is a well-established approach with a high success rate. It has the advantages that the material is readily available and has less chance of infections, which is often the case for homo- and xenografts (tissues from donors or animals). However, it requires high capital investment for an operation room, anesthesia, and a surgeon with microsurgical skills.[137,144] Also, due to the different mechanical properties of the applied graft, hearing can remain partially impaired, and multiple revision surgeries are often needed, in which case the available tissue might be a limiting factor.[138 150]

As an attempt to simplify the procedure and the costs of a tympanoplasty, synthetic materials have been used to patch eardrum perforations. Unfortunately, for chronic perforations microsurgery remains necessary even for synthetic materials, as the margins of the perforation should be ruptured as a means of stimulating healing, usually done by mechanical removal or chemical cautery.

Typical synthetic materials, in this case, are gel foams and paper patches, but they show a poor success rate, as they are easily detached and are prone to infections. To keep them in the proper position, it is still required to pack the outer ear canal with foam and cotton, leaving the patient's hearing impaired for several weeks. To stimulate healing, some studies present the positive influence of an additional integration of growth factors to the patch in contact with the remanent TM.[152–154] A clinical study presented a PDMS foil coated with collagen with a 70% closure rate and improved hearing ability *in vivo*, as an alternative material for tympanoplasty type I. However, this approach would still require packing the outer ear canal, as it does not adhere to the TM.[155]

Most recently, there has been an increasing number of studies towards tissue engineering therapies for TM reconstruction. Scaffolds in tissue engineering are 3D structures with integrated bioactive stimuli (growth factors) and cells, that work as a template for tissue restoration.[134 137 156] Novel tissue-engineered materials, either as cellular or acellular patches, offer the advantages of easy application, more uncomplicated surgeries, improved hearing after the treatment, and fewer incidence of re-perforations. [134]

The scaffolds are fabricated, for example, using 3D manufacturing[151,157] or electrospinning,[158,159 160] attempting to match form and properties of the native tissue. A variety of materials have been explored, synthetic such as PDMS,[157] Poly(caprolactone) (PCL),[142 159 160 161] poly(lactic acid) (PLA),[162] or naturally derived polymers, as silk,[160] gelatin, [163] and collagen.[157 164] Natural compounds such as hyaluronic acid (HA)[165 166] can be interesting to regulate the orientation of the fibroblasts and collagen fibers of the *lamina propria* during closure, but they are susceptible to batch variability and can induce inflammatory reaction and rejection.[167] The use of polymeric materials offers superior control over the structural and mechanical properties of the scaffold. Also, the use of synthetic graft was shown to reduce operation time and avoid an extra incision to harvest the graft.

More complex architectures of TM grafts can involve a combination of different polymeric materials (PMDS, PLA and PCL), in a 3D printed design following the pattern of the collagen fibers observed in a native TM.[157] However, in scaffolds that serve as a matrix for tissue formation, the structure, if not biodegradable, remains inside the TM and, if not precisely matched with the membrane, the TM will not have its properties restored as before the perforation.

Finally, other patient-specific factors remain a challenge in TM reconstruction, such as size and location of the perforation or the presence of other pathological complications.

Chapter 3. Scope of this work

This work addresses the current need for optimal adhesives in biomedicine, and the results are presented as follows.

First, in Chapter 4, we presented the adhesion of the film-terminated microstructure on different surfaces: randomly distributed roughness (glass smooth up to skin-like) and then to sinusoidal model surfaces. The goal was to understand the contact formation and adhesion of the microstructure and its superior performance compared to flat, unstructured samples.

Then, in Chapter 5, a second biomedical application was tackled: an alternative solution for treating eardrum perforations is proposed. Several studies report the need for mechanical support for the migration and proliferation of epithelial cells in the healing process of the eardrum. To reduce costs, patients' discomfort, and hearing impairment after treatment, we proposed a simple approach using a microstructured adhesive to support cell growth. This project followed previous studies from our group for wound dressings and adhesion to the eardrum, but using unstructured samples.[63,168] Here, we demonstrated the microstructured patch's adhesion on stiff, rough substrates and to mouse eardrums by *ex vivo* tests. Also, using *in vivo* hearing tests, we evaluated the effects of patch application on hearing properties. *Ex vivo* and *in vivo* tests were performed in collaboration with the ENT Clinic at Saarland University.

Finally, the mentioned safety mechanism that protects the tissue against further damage was described in Chapter 6. Any additional force applied goes to buckling the subsurface fibrils, not being directly transferred to the countersurface, and not interfering with the adhesion performance.

Chapter 4

Film-terminated fibrillar microstructures with improved adhesion on skin-like surfaces

Chapter 4. Film-terminated fibrillar microstructures with improved adhesion on skin-like surfaces*

4.1 Abstract

Adhesives for interaction with human skin and tissues are needed for multiple applications. Micropatterned dry adhesives are potential candidates allowing for a conformal contact and glue-free adhesion based on van der Waals interactions. In this study, we investigate the superior adhesion of film-terminated fibrillar microstructures (fibril diameter 60 µm, aspect ratio 3) in contact with surfaces of skin-like roughness (R_z 50 µm). Adhesion decays only moderately with increasing roughness, in contrast to unstructured samples. Sinusoidal model surfaces adhere when their wavelengths exceeded about four fibril diameters. The film-terminated microstructure exhibits a saturation of the compressive force during application, implying a pressure safety regime protecting delicate counter surfaces. Applications of this novel adhesive concept are foreseen in the fields of wearable electronics and wound dressing.

4.2 Introduction

Skin-attachable adhesives are experiencing rising demands in healthcare, where potential applications range from flexible and wearable electronics for monitoring and diagnosing biological signals[95 86 94] to therapeutic devices and wound dressings.[168 169] Biological surfaces and tissues are challenging counter surfaces to stick to, as surface roughness is one key factor for reduced adhesion.[95] This is primarily due to the difficulty of achieving fully conformal contact, which decreases the real contact area and causes heterogeneous stress distributions at the interface.[170] Roughness requires high local deformations and hence counteract the

*This chapter was published in ACS Applied Materials and Interfaces:

Moreira Lana, G.; Zhang, X.; Müller, C.; Hensel, R.; Arzt, E. Film-terminated fibrillar microstructures with improved adhesion on skin-like surfaces. ACS Applied materials & interfaces, 2022. https://pubs.acs.org/doi/10.1021/acsami.2c12663

short-range adhesive molecular forces.[34 171] As a consequence, new adhesives for reliable yet delicate interaction with skin-like surfaces are urgently required.

The efficiency and versatility of several attachment systems in nature, e.g., in geckos, beetles, spiders, or snails, has been a source of inspiration to materials scientists and engineers: in many cases, their outstanding locomotion and clinging ability, to various smooth and rough surfaces, is due to patterned micro and nanostructures on their contact organs. The bioinspired microfibrillar patterns derived from these examples have been widely studied in the past years.[5,172,173] More recently, they have proven to be potential candidates as dry and glue-free adhesives to skin. Current solutions for skin adhesives offer too strong adhesion causing damage while being removed,[174,175] in addition to being of single use and leaving residues that can cause skin irritation and allergies. Therefore, a reliable adhesive with sensitive detachment is needed.[7 8]

Dry adhesion is mediated by conformal contact, enhanced by a low effective elastic modulus, and Van der Waals (VdW) interactions, both of which contribute to useful adhesion even to rough surfaces.[63,176–178] For skin applications, a film-terminated design was proposed which modifies the microfibril array by adding a continuous terminal layer made of softer material. This modified microstructure has shown enhanced adhesion by modulating the interfacial stresses and generating a crack trapping mechanism; the result is an interesting synergy between the subsurface microstructure and the soft, thin terminal layer.[42,56,57,178] The added layer also performs auxiliary functions: in wound dressings, it can aid in the closure of the wound; and in the treatment of eardrum perforations, it closes the fissure in the membrane, which is important to block pathogens from entering the middle ear during the treatment.[169 179]

As the largest organ in humans, the skin presents an especially complex topography, which can vary over several orders of magnitude. The detailed structure depends on many factors such as body location, age, and humidity.[180–182] Explicit studies that take into account the roughness of skin when optimizing skin adhesives have rarely been published in the literature.

In this paper, we aim to investigate the adhesion mechanism of novel film-terminated microstructures designed to adhere specifically to rough skin without the need for chemical glues, thus, not leaving residues on the surface or causing adverse reactions. We conduct a systematic investigation of such microstructures, consisting of two biomedical silicones, on a series of surfaces with random and single-wavelength roughness. Adhesion is analyzed in comparison to unstructured films as control samples. We evaluate experimentally and numerically the effect of the terminal layer thickness and the role of the fibrillar microstructure on the adhesion performance. In this way, we provide a scientific base for this new class of micropatterned skin adhesives.

4.3 Experimental Section

Fabrication of film-terminated and control samples

Film-terminated microstructures were fabricated, and respective unstructured samples with terminal layer were used as a control to investigate the effect of the subsurface microstructure on adhesion.

Arrays with fibrils of nominal height of 180 µm and diameter of 60 µm (aspect ratio 3) were fabricated by replica molding. The fibrils were arranged hexagonally with center-to-center distances of 120 µm (surface density approximately 23%). A silicon master template (Institute of Semiconductors and Microsystems, TU Dresden, Germany) was used to prepare the negative silicone mold (Elastosil M4601 A/B silicone, Wacker Chemie AG, Munich, Germany). The pre-polymer was mixed (ratio 9:1) and poured on the master template. The silicone was then cured in an oven at 75°C for 3 h. The silicone mold was treated by air plasma (Atto low pressure plasma system, Electronic Diener, Ebhausen, Germany) for 3 min and then coated with tridecafluoro-1,1,2,2-tetrahydrooctyl-trichlorosilane (AB111444, ABCR, Karlsruhe, Germany) through vapor deposition at 3 mbar for 45 min. The microfibrillar array was made from the biomedical grade elastomer MDX4-4210 (Dow Silicones, Midland, Michigan, USA). The pre-polymer was mixed in a ratio 10:1, poured on the Elastosil mold and degassed for 5 minutes. The mold was then spun at 3000 rpm for 2 min (Spincoater Laurel l WS 650 MZ–23NPPB, North Wales, Pennsylvania, USA) and then placed on a glass substrate, which was

previously plasma treated and coated with MDX4 silicone (3000 rpm for 2 minutes). The whole set was placed in an oven at 95 °C for 1 h. Finally, the mold and the glass were gently demolded. For the unstructured control samples, a foil of the MDX4-4210 was prepared using spin coating at 500 rpm for 2 minutes, to achieve a thickness comparable to the sum of backing layer and fibril height for the fibrillar microstructure.

In a second step, the microfibrillar array, or the respective flat film, was film-terminated. Accordingly, a soft skin adhesive film, SSA MG7-1010 (Dow Silicones, Midland, Michigan, USA), was used. Previous reports use a softer material by changing the mixing ratio of the "stiffer" silicone. [58] [183] However, this approach makes the product unsuitable for medical applications, as the manufacturer does not predict the reactivity and curing conditions, being, therefore, not medically certified. The SSA was coated on a release foil (Siliconature, SILFLU S 75 M 1R88002 clear) at 800, 2000, and 6000 rpm. The SSA layer was cured at 95 °C for 1 h. To combine the microfibrillar array with the SSA layer, fibril tips were dipped in an uncured MDX4-4210 layer (spun on a glass substrate at 400 rpm) and placed on the cured SSA film. The unstructured control sample was terminated using the same method, dipping the film in an uncured MDX4 layer before placing on the cured SSA layer. Upon curing in an oven at 95 °C for 1 h, the final specimen was peeled from the release foil. The fibril height increased from 180 to 200 µm (and the aspect ratio from 3 to 3.3) due to the fabrication described above. Considering biomedical applications, only certified medical products MDX4-4210 and MG 7-1010 were used.

Specimens were characterized using an optical microscope (Eclipse LV100ND, Nikon, Tokyo, Japan) and a scanning electron microscope (FEI Quanta 400 ESEM, Thermo Fisher, USA). The specimens were analyzed under low vacuum at 100 Pa and 10 kV voltage for the latter.

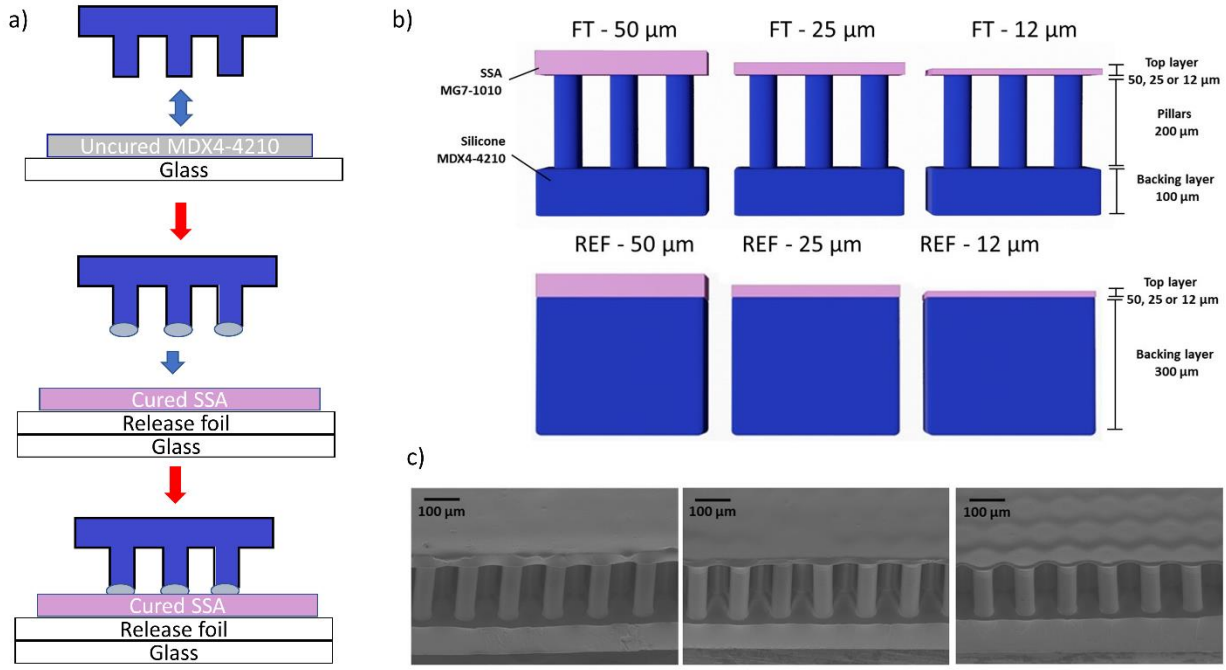

Figure 4.1: Film-terminated microfibrillar samples. (a) Representation of the film-terminated microstructure fabrication process by integrating an SSA film with a microfibril sample. The tips of the fibrils are dipped in an uncured film, then placed on a cured SSA layer. (b) Schematic cross-section of a soft skin adhesive (SSA) film (pink) terminating a silicone microfibrillar array of MDX4-4210 (blue) and of the unstructured control samples. The terminating film has various thicknesses of 12, 25, and 50 µm. (c) Representative scanning electron micrographs of the different samples.

Figure 4.1a presents a summary of the fabrication process of the film-terminated microstructure. The fibrils are fabricated by replica molding and yield precise copies by a relatively inexpensive method. Unlike simple porosity, the fibrils offer an additional advantage of a controlled, periodic structure suitable for subsequent integration of other systems. The cross-sections of the film-terminated and respective control samples are illustrated in **Figure 4.1b**. The MDX4-4210 fibrillar array (in blue) consisted of a 100 µm backing layer and fibril arrays of 200 µm height and 60 µm diameter, and the SSA MG7-1010 terminating layer (in pink) varied in thickness 12, 25, and 50 µm. The chosen materials are medically certified for wound dressings and implantable devices, widening the possibility of application of these microstructured adhesives in different purposes, including wound

dressings. For brevity, we denote the samples according to their terminal layer thickness, for instance, FT – 12 µm for the film-terminated microstructure with a 12 µm thick terminal layer. The respective unstructured reference samples were fabricated with MDX4-4210 backing layer of 300 µm and terminal layer equivalent to the microstructures (12, 25 or 50 µm thickness). In addition, microfibrils without the thin film as terminal layer were also used for control measurements. Scanning electron microscopic (SEM) images of different samples are presented from 45°-tilt side view (**Figure 4.1**c). We observe that the thinnest film is slightly deformed due to stress relaxation.

Rheometry

Frequency-dependent storage and loss moduli (G', G'') and the damping factor $\tan\delta = G''/G'$ of the polymers were determined using a rheometer (Physica MCR-300, Anton Paar, Graz, Austria) equipped with a cone/plate setup (diameter 25 mm, gap height 0.054 mm). The pre-polymer mixture of components A and B (in mixing ratio 10:1 for MDX4-4210 and 1:1 for the SSA) was placed on the device. The polymer was cured between the plates at 90 °C for 30 minutes. Upon cooling to 25 °C, a frequency sweep measurement from 0.01 to 100 Hz at a constant amplitude of 0.1% was carried out.

The Young's modulus, E, for both materials was calculated from the measured storage modulus in shear, G, considering $E = 2G\ (1 + \nu)$, with ν = 0.5. The elastic modulus values obtained were $E_{MDX4-4210} = 1.01\ MPa$ and $E_{SSA} = 0.102\ MPa$. Overall, the terminating film was made from a softer silicone than the microfibrillar array.

Adhesion measurements

Probe tack tests, in which a flat probe is retracted from the adhesive in perpendicular direction, were performed using a custom-built adhesion testing device.[63,184] Specimens and counter surface were approached at a rate of 30 µm/s until a pre-determined compressive preload or displacement was reached. Contact was held for 1 s followed by retraction at a rate of 10 µm/s. Measurements were performed at three different positions on each surface. Mean values and standard deviation (error bars) were reported. Counter surfaces were

always smaller than specimens; therefore, stresses were calculated by dividing force values by the area of the counter surface. All surfaces were made from epoxy (Résine Epoxy R123, Soloplast-Vosschemie, Fontail-Cornillon, France), as described in previous reports, [112,185] to keep surface chemistry constant. Epoxy replicas were made from smooth and frosted glass slides (Marienfeld, Lauda Königshofen, Germany) and the front and back sides of Vitro-skin foil (IMS inc., Portland, ME, USA). Vitro-skin foil was chosen as it mimics the topography of the human skin. [186 187]

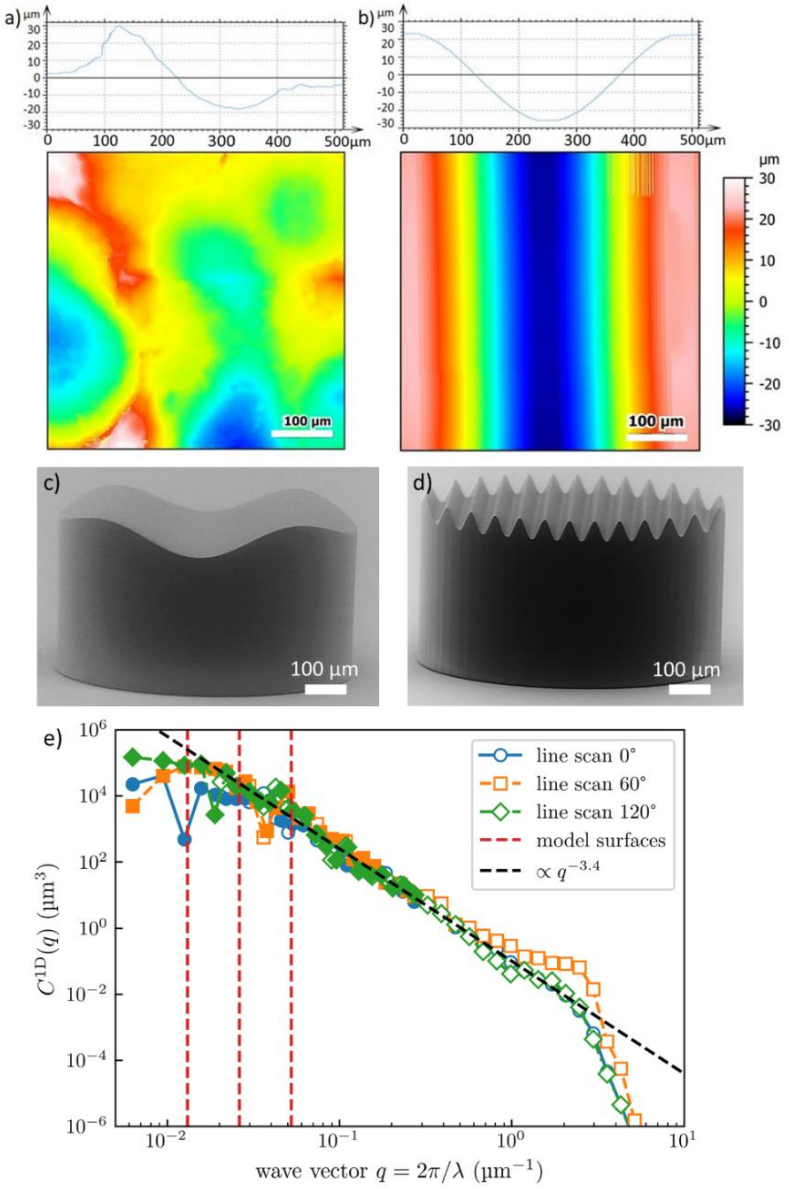

Figure 4.2: Surface profile and topography of counter surfaces. (a) Scan of skin-like rough surface, in comparison to (b) sinusoidal model surface with 480 µm wavelength. (c) and (d)

SEM micrographs of the printed surfaces with the sinusoidal model surface of wavelength 480 µm and 60 µm, respectively. (e) Power spectral density (PSD) of the Vitroskin surface, determined from line scans along different surface directions. Solid markers indicate reliable data, while empty markers indicate unreliable data as limited by the tip radius.[188] The isotropic one-dimensional PSD (C^{1D}) is defined as given in Ref. [114]. The dashed vertical red lines represent the wavelengths of the model surfaces.

A contour map of the skin-like surface and a cross section profile are depicted in **Figure 4.2a.** It presents arithmetic roughness (R_a) of 9.48 µm and a peak-to-valley distance of ~50 µm in accordance with the statistical value $R_z = 50\ \mu\text{m}$. Adhesion to such high roughness has not yet been described in literature; for film-terminated microstructure adhesion has only been reported in literature against the roughness of maximal R_a 2.3 µm. [57] A sinusoidal model surface of wavelength 480 µm is depicted in **Figure 4.2b**. The surfaces were imaged using a confocal microscope (MarSurf CM explorer, 50x objective, Mahr, Göttingen, Germany). At constant peak-to-valley distance of 50 µm, corresponding to the skin-like surface, the following different wavelengths were chosen: λ= 480, 240, 120 and 60 µm. The model surfaces were fabricated using two-photon lithography (Photonic Professional GT2, Nanoscribe, Eggenstein–Leopoldshafen, Germany). SEM images of the printed sinusoidal model surfaces are presented in **Figure 4.2c** and **d**.

In order to rationalize the choice of model surface wavelengths, we analyzed the Vitroskin topography using a Profilometer (SURFCOM 1500SDS, ACCTee Software, Ostfildern, Deutschland) with a tip of 2 µm of diameter and measuring speed of 0.3 mm/s, and characterized by the Surface Topography Analyzer. [189] The corresponding power spectral density (PSD) is shown in **Figure 4.2e**, where the reliability of data points was explicitly determined from the curvature of the profilometer's tip radius. [188] Since line scans along different directions look very similar, the surface can be considered isotropic. Assuming a self-affine fractal topography, the slope of the curve would suggest a Hurst exponent of approximately 1.2, outside the range of [0,1], indicating that the surface is not in fact fractal. Recently, Gujrati et. al. connected an exponent of -4 in the PSD to macroscopic patterns in

surface coatings[97]. The exponent -3.4 could indicate the presence of similar features overlapping with a self-affine power law. Regardless of the exact interpretation, a decrease with a large exponent equivalent to H > 0.5 still indicates that long wavelength features within this range have a much more significant influence on the contact mechanics than short wavelength features. [190] The sinusoidal model surfaces are chosen close to the roll-off point on the left end of the spectrum, where the graph transitions from the power law behavior to being almost constant. This range is decisive for the elastic energy to contact nominally flat surfaces, as we use in normal tack tests. This condition for the choice of the model surface is explained in more detail in section 4.3.

Finite element analysis

Finite element analyses (FEA) were carried out using Abaqus (Dassault Systems, Simulia Corporation, RI, USA). [191] The two-dimensional model consisted of an elastic film-terminated sample meshed with a CPS4R element and a rigid sinusoidal surface meshed with R2D2 elements. The dimensions of the model remained the same scales as in the experiments, i.e. (all dimensions are normalized by the fibril diameter of 60 μm) fibril height = 3, center-to-center distance = 2, terminal-layer thicknesses = 1/5 or 5/6, sinusoidal amplitude = 5/6, and wavelengths = 4 and 8, separately. Both fibrils and the terminating film were modeled as incompressible neo-Hookean elastic solids with Young's moduli of 1.1 MPa and 0.102 MPa, respectively. Two relative configurations of the fibrils and sinusoidal surface were considered: fibrils were either centered on the maxima or shifted by 60 μm. The interaction property between the film-terminated sample and the wavy surface was defined as "*Hard contact*" for normal contact and "*Friction with Penalty*" for tangential contact. To avoid slippage after the contact, the penalty coefficient μ was set to 0.5, corresponding to the friction coefficient in the Coulomb friction law, $\tau_{fric} = \mu P$, where *P* is the normal contact pressure between the contacting surfaces. The step "*dynamic, implicit"* was used to calculate the actual deformation by uniaxial loading, during which only the vertical displacement of the top surface of the backing layer was set while other translational degrees of freedom were fixed to mimic the constraint of the backing layer in the experimental sample.

4.4 Results

Adhesion to smooth counter surfaces

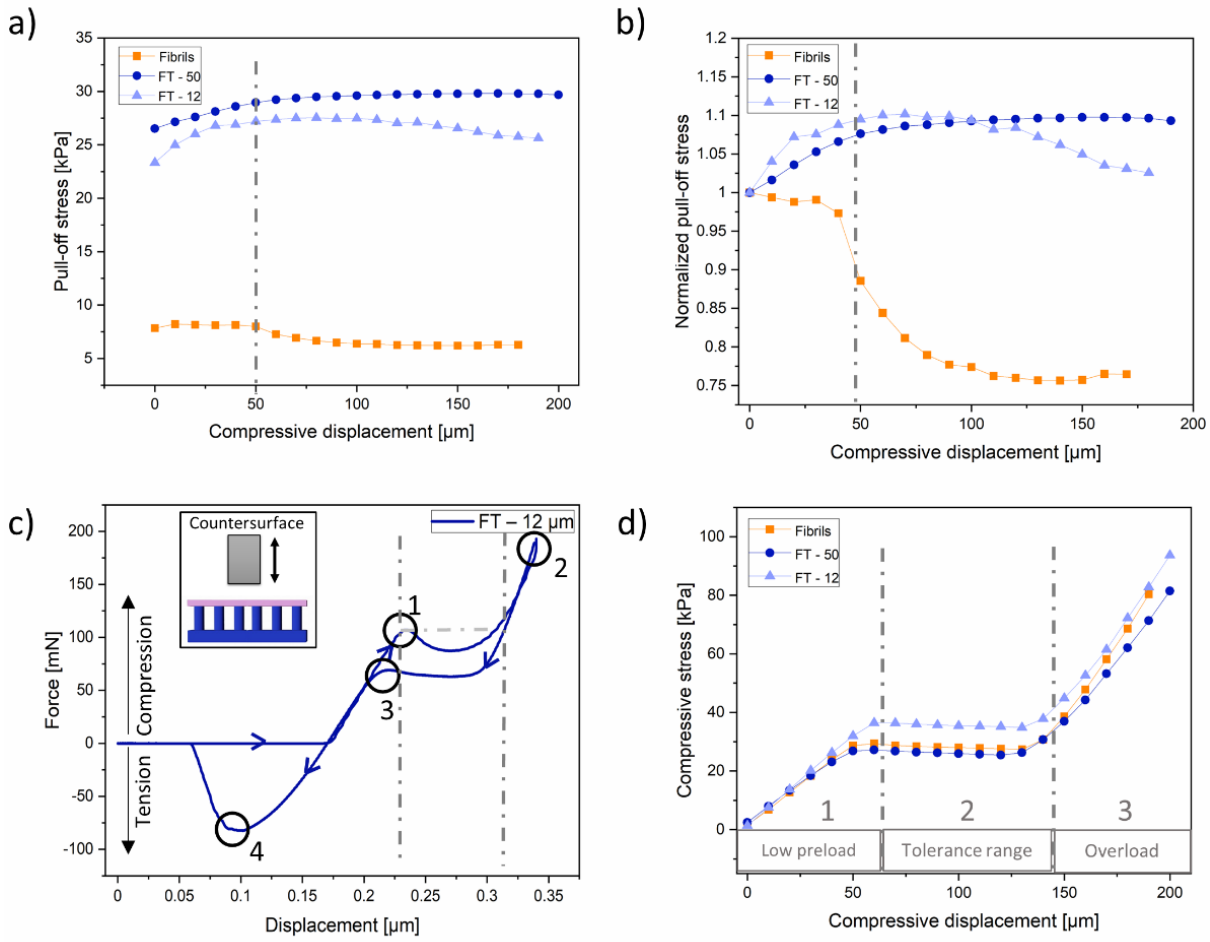

Figure 4.3: Results of adhesion tests against a smooth epoxy surface. (a) Pull-off stress and (b) normalized pull-off stress (by the pull-off stress at zero compression) as function of maximum compressive displacement for film-terminated (FT) microfibrils (blue) *in comparison to non-terminated fibrillar array (orange). The dashed-dotted line indicates the onset of fibril buckling. (c) Force vs. displacement display of a measurement of the film-terminated sample with 12 µm thick film, and a schematic representation of the measurement principle. Points highlight fibril buckling (1), maximum compression (2), unbuckling of fibrils (3) and maximum pull-off force (4). (d) Compressive stress as function of compressive displacement. Dashed-dotted lines mark 3 regimes: 1) low preload; 2) compression-tolerant regime and 3) overload regime, and correspond to the lines in (c).*

Figure 4.3 shows a summary of adhesion results of the FT – 12 μm, FT – 50 μm and fibril samples without terminal layer, against a smooth flat epoxy surface. In **Figure 4.3a**, the adhesion of the FT samples ranged between 24 and 30 kPa, which was 3 to 5 times larger than samples without a terminating layer. The FT – 50 μm sample consistently led to a higher pull-off stress than that of the FT – 12 μm sample, which could be attributed to the vastly reduced influence of the much stiffer fibrils, in comparison to the terminal layer.

Compressive load is an important factor for adhesion in order to achieve optimal contact with the countersurface.[59] We observe that the microfibrils without terminating film exhibited a substantial reduction in adhesion at about 50 μm maximum compressive displacement (dashed-dotted line). This reduction is even clearer in **Figure 4.3b**, where the pull-off stress was normalized by its value at zero compression. The initial buckling position (point 1) is shown in an example of force-displacement curve on the FT – 12 μm sample in **Figure 4.3c**; located at a compression displacement at 50 μm, it corresponds to the position with the large drop in adhesion in **Figure 4.3b**. After buckling, the decrease of the compressive force is attributed to the postbuckling instability.[25,192] When the deformed fibrils topple over and contact the backing layer, the compressive load increases again until the maximum compressive load is reached (point 2). Point 3 in the graph marks the elastic recovery of the buckled fibrils. The hysteresis between points 1 and 3 can most likely be attributed to viscoelastic properties of the materials. Finally, detachment occurred, and the pull-off force was obtained from the maximum in the tensile force (point 4).

The evaluation of the compressive load in terms of the maximum compressive displacement is depicted in **Figure 4.3d**. Three regimes can be identified: a low preload, a force tolerant, and an overload regime. In the first regime, the pull-off force increases linearly with increasing displacement; the force saturates in regime 2, where the compressive force is insensitive to the displacement; and in regime 3, the compressive force increases linearly again with a higher slope, indicating densification of the fully compressed fibrils.

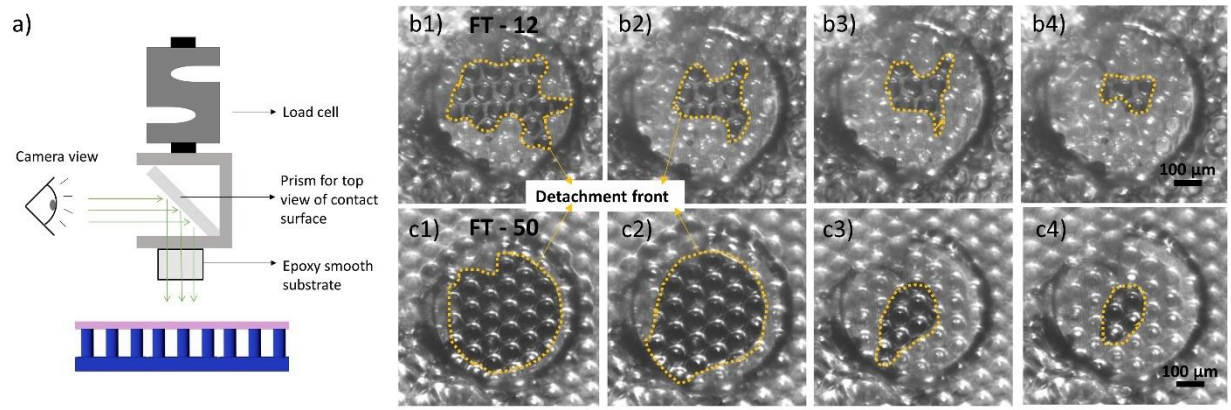

Figure 4.4: Contact surface imaging during detachment from smooth surface. (a) Schematic representation of the experimental setup, in which a prism for observation of the contact surface is mounted on the load cell. (b) Screenshots of contact surface of FT – 12 (above) and FT – 50 (below) against a smooth surface during detachment (left to right). The detachment front is highlighted by the yellow dotted line.

The experimental setup, as well as the detachment process of the film-terminated structure from the smooth epoxy surface can be seen in **Figure 4.4**. The large circular margin in **Figure 4.4b** illustrates the surface position and darker regions enclosed by the dashed lines represent the edge of the contact area. The crack initiates from the edge of the counter surface and moves inwards for both samples. The crack path (dashed lines) is more tortuous for the thinner backing layer (FT – 12 µm) and reflects the underlying the fibrillar structure.

Adhesion results to surfaces with random roughness

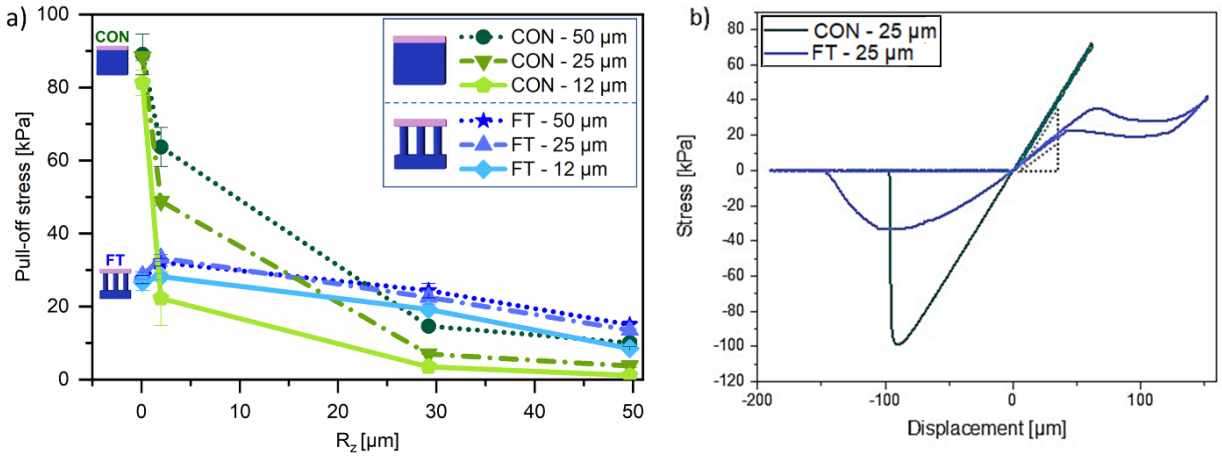

Figure 4.5: Adhesion against rough surfaces. (a) Pull-off stress of film-terminated microstructure and control samples, as function of roughness R_z of the counter surface, from smooth ($R_z = 0.1\ \mu m$) to skin-like roughness ($R_z = 50\ \mu m$) at preload of 10 kPa and hold time 1 s. (b) Example of stress-displacement curve of FT – 25 µm and of reference CON – 25 µm, subjected to larger compressive preload.

Next, adhesion tests on randomly rough surfaces were conducted to investigate the advantage of the terminal layer design. **Figure 4.5a** shows the pull-off stress in terms of the surface roughness R_z (mean peak to valley distance) ranging from 0.1 to 50 µm. The pull-off stresses for the FT samples with different terminal layer thicknesses are all located between 25 and 30 kPa for the smoothest surface (R_z = 0.1 µm). Under the same measurement conditions, the effect of the terminal layer thickness is not distinguishable. The unstructured control samples, on the other hand, present pull-off stresses between 80 and 90 kPa, up to 3 times higher than the microstructure. In **Figure 4.5b**, examples of stress-displacement curves for the microstructured FT – 25 sample and the respective unstructured control are presented.

As the roughness R_z was increased to 1.1 µm, we observed a slight increase of pull-off stress for the microstructured samples, more pronounced for the samples FT – 50 and FT – 25 (27 and 28 kPa to 32 and 33 kPa, respectively) than for FT – 12 (26 to 28 kPa). The control samples,

on the other hand, showed an reduction in pull-off stress (88 kPa to 64 kPa for FT – 50 and 81 to 22 kPa for FT – 12).

Further increase in surface roughness led to a decline in pull-off stress for all samples. The decay for the control samples was, however, much more substantial: for roughness R_z = $50\ \mu m$ (skin-like), CON – 50 had the adhesion reduced by 88%, going from 88 kPa to around 10 kPa, and CON – 12 had a reduction by 98%, reaching 1.1 kPa at high roughness. Microstructured samples, on the other hand, had a less pronounced decay; FT – 50 went to 15 kPa, losing around 43% of the adhesion performance in comparison to a smooth counter surface, and FT – 12 went to around 8.5 kPa, a reduction to 32% of its initial value.

Adhesion results to sinusoidal model surfaces

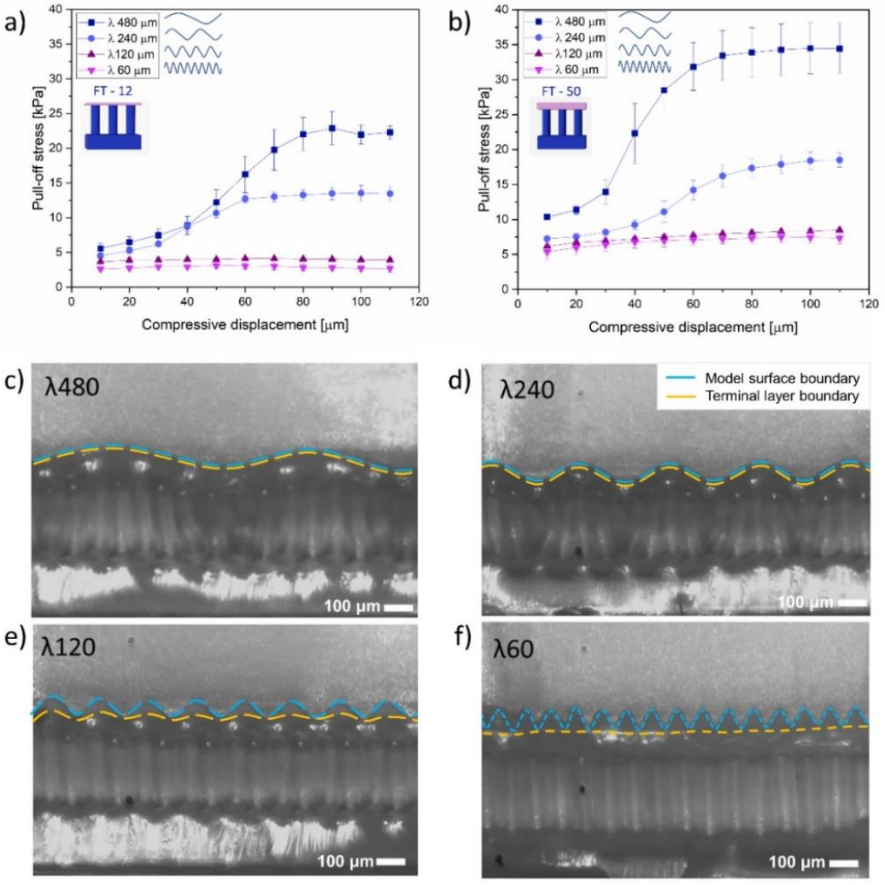

Figure 4.6: Adhesion of film-terminated microstructures on sinusoidal model surfaces. Pull-off stress vs. compressive displacement for sample with terminal layer (a) 12 µm and (b) 50

μm, for the surfaces with different wavelengths. Snapshots show sideview of FT – 50 against surfaces with wavelength (c) 480 μm, (d) 240 μm, (e) 120 and (f) 60 μm, in compressed state. Scale bar is 100 μm. Blue dashed lines mark the model surface boundary, and yellow dashed lines indicate the microstructure's terminal layer boundary.

Pull-off stresses as a function of compressive displacement for FT – 12 and FT – 50 μm against the different sinusoidal model surfaces are presented in **Figure 4.6a** and **Figure 4.6b**. As before, the sample with the thicker terminal layer (FT – 50 μm) showed higher adhesion values. The wavelength of the counter surface modulated the adhesive behavior in the following ways:

For wavelengths of 60 and 120 μm, i.e. close to the fibril diameter, the pull-off stress was almost insignificant (around 4 kPa for FT – 12 μm and 7.5 kPa for FT – 50 μm) and increased only slightly with increasing compressive displacement;

For the longer wavelengths of 240 and 480 μm, adhesion was generally higher and increased in a more pronounced way with compressive displacement between 30 and 70 μm. The final plateau values were 13 and 25 kPa for FT – 12 and 17 and 35 kPa for FT – 50.

The transition from low to high adhesion for the long-wavelength surfaces occurred at a compressive displacement of about 50 μm, which corresponds to the amplitude of the sinusoidal surface shape.

In **Figure 4.6c** to **Figure 4.6f**, we present in-situ lateral views of the sample FT – 50 μm in a compressed state against all the counter surfaces. A physical impediment to full contact is observed for the counter surfaces with wavelengths 60 and 120 μm, where contact was achievable only near the surface peaks, even at high compression. By contrast, the terminal layer of the microstructure eventually achieved "full" contact with the counter surfaces of wavelengths 240 and 480 μm. The transition between the two different kinds of adhesion behavior seems to occur at the following empirical condition:

$$\lambda \approx 4D \tag{1}$$

where *D* is the fibril diameter and λ the wavelength. For $\lambda < 4D$, the pull-off stress is low and insensitive to the compressive preload as full contact with the counter surface is always prevented. On the other hand, for $\lambda \geq 4D$, the microstructure could deform almost conformally to the rough surface and the pull-off stress increased with the preload. The performance of the adhesive in the case $\lambda \geq 4D$ was further investigated.

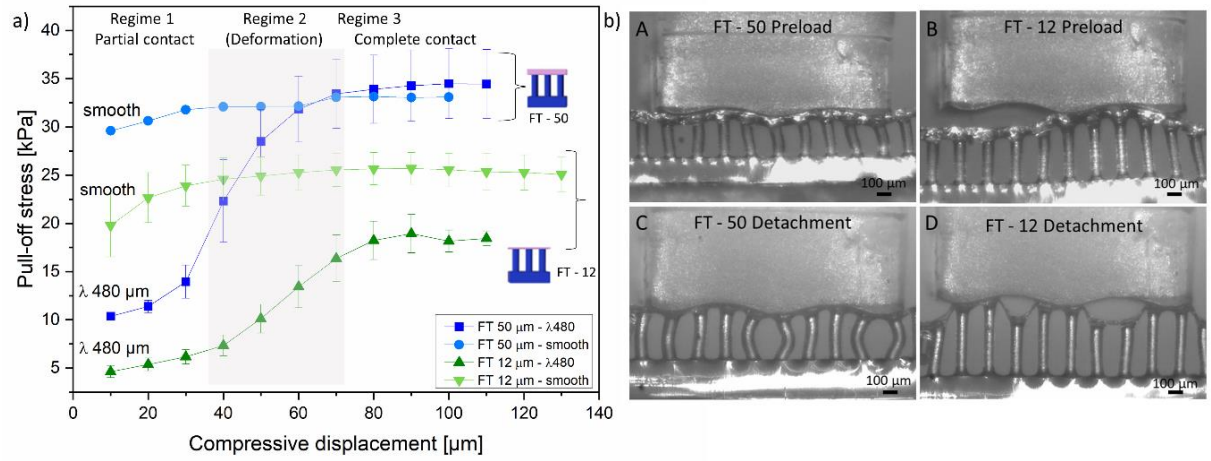

Figure 4.7: Adhesion of microstructures on model surface 480 µm in comparison to smooth surface. a) Pull of stress as function of compressive displacement for FT – 50 and FT – 12 against the smooth surface and model surface of wavelength 480 µm. b) Side view of single row FT – 50 in full contact (A) and detachment (B) and FT – 12 in full contact (C) and detachment (D) against 480 µm wave model. Scale bar is 100 µm.

Figure 4.7a presents a comparison of adhesion results for FT – 12 and FT – 50 samples against the smooth surface and the model surface of wavelength 480 µm. For the smooth surface, the slight increase of pull-off stress, mostly at initial compressive displacement, can be explained by full contact formation and, possibly, by a contribution of the material's viscoelasticity.[110 193] For the sinusoidal model surface, three regimes can be distinguished: In regime 1, the sample and counter surface have low contact; next, in regime 2, the fibrils

undergo bending, which allows them to form progressively more contact with inclined areas of the counter surface and creates higher adhesion; finally, in regime 3, the sample reaches close-to-full contact and adhesion enters a plateau. For sample FT – 12, the plateau stress values amount to approximately 70% of the values obtained for the smooth surface. Interestingly, the FT – 50 sample reaches, within the error margin, similar adhesion as on the smooth surface.

In **Figure 4.7b**, side views of detachment from the model surface with wavelength 480 µm are presented for a single row of fibrils, for better visualization. The ability of the fibrillar microstructure to conform to the wavy counter surface is well illustrated and will be discussed below.

Finite element simulation results

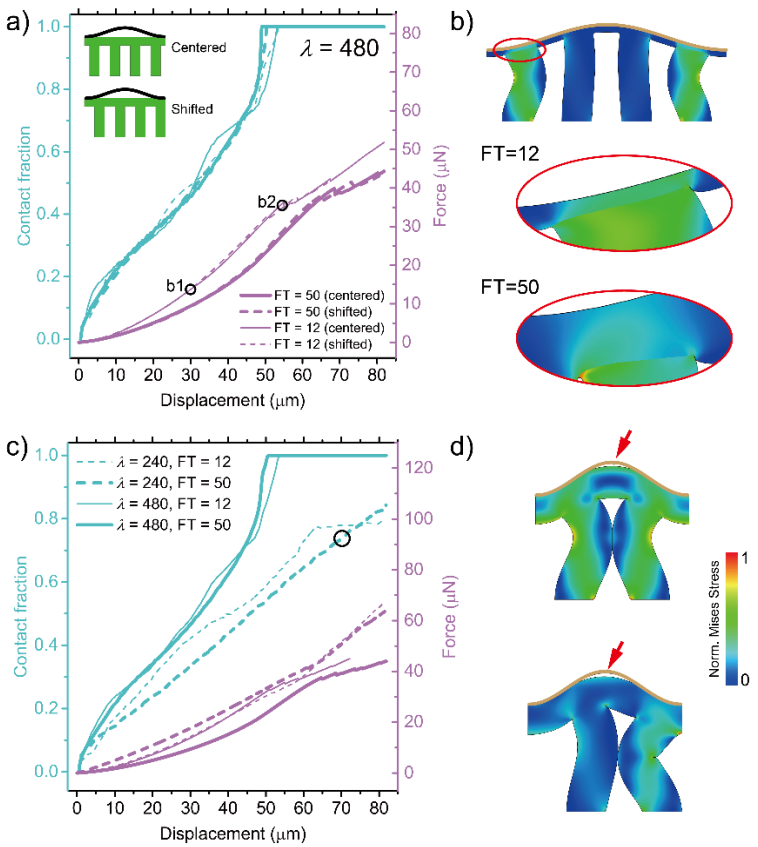

Figure 4.8: Simulation of compressive force and contact fraction for model surface 480 µm (a and b) and surface 240 µm (c and d). a) The relations of contact fraction and compressive

force vs. compressive displacement for FT – 12 and FT – 50 samples with λ=480 μm, in centered and shifted alignment. b) Snapshots of deformation processes of FT – 12, with highlighted region of the terminal layer of both samples in positions marked "b1" and "b2" in a). c) Relationship between the contact fraction and compressive force vs. compressive displacement for surface λ=240 and 480 μm separately. d) Snapshots at a contact fraction of about 70% and a displacement of about 70 μm of the critical deformation moment when the neighboring fibrils touch each other under centered and shifted arrangements when λ=240 μm.

To obtain better quantitative insight of the contact behavior, information not accessible by the experimental setup, we analyzed the numerical results of our finite element simulations for samples FT – 12 and FT – 50 μm in contact with a λ = 480 μm surface. Contact fraction (i.e. percentage contact area of the total surface) and compressive force were calculated with increasing compressive displacement for two different alignments: in one case, a fibril was centered on a wave valley and, in the other, the space between was centered, as indicated in the insets in **Figure 4.8a**. The force results overlapped for displacements smaller than 30 μm and subsequently diverged somewhat; the shifted arrangement produced slightly higher force values, but overall fibril alignment did not strongly affect contact fractions. Full contact was achieved for compressive displacement larger than 55 mm. **Figure 4.8b** presents a snapshot of FT – 12 samples in full-contact configuration, as well as the terminal layer in both cases in the highlighted region. The FT – 12 fibrils underwent severe bending in accordance with the experimental observations in **Figure 4.7**.

Subsequently, we compared the simulation results for the cases λ = 240 μm and λ = 480 μm (**Figure 4.8c**). Here, all the curves represent the average results of the centered and shifted alignments. While, in most cases, the contact area increased monotonically until full contact was reached, significantly higher forces were required for the 240 μm surface. A new event was observed for the λ = 240 μm surface: the contact fraction of the FT – 12 sample levelled off at 77% (at a compressive displacement of 65 μm). The snapshots in **Figure 4.8d**) explain this inability to achieve full contact: at a critical displacement of about 70 μm, severely bent

neighboring fibrils start to impinge, which prevents further contact from forming. Although the optical observation in **Figure 4.7b** (λ = 240 µm) seems to indicate full contact, the numerical result in **Figure 4.8c** reveals that the system may not be able to reach this state in the model topography. This may, to some extent, explain the earlier detachment and lower pull-off stress for λ = 240 µm compared to λ = 480 µm.

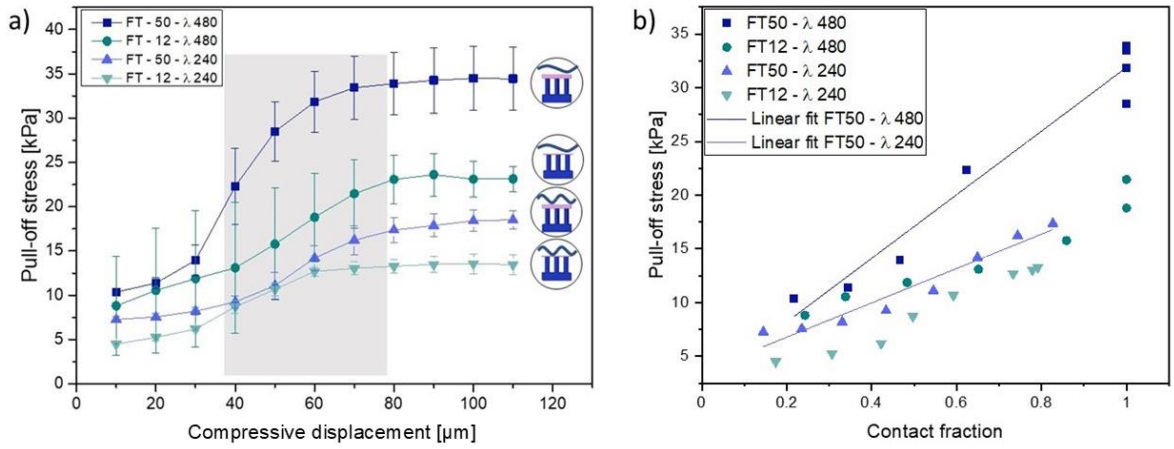

Figure 4.9: Adhesion on model surfaces 480 and 240 µm. a) Pull-off stress for FT – 50 and FT – 12 as function of maximum displacement for the waves of λ 480 and 240 µm. Similar trend is observed for the wave 240 µm, in comparison to the larger one, described in detail in the main text. (b) Measured pull-off stress as function of contact fraction during compression, obtained from the simulations. Linear fit is indicated for the FT – 50 for both surfaces 480 and 240 µm.

Figure 4.9a shows the pull-off stress for FT – 50 and FT – 12 on the counter surfaces of λ 480 and 240 µm. Similarly for all cases the pull-off stress increases with rising displacement and saturates to a plateau value. Although camera images (**Figure 4.6c,d**) suggest that the microstructures have contact with both surfaces, 240 and 480 µm, numerical simulations showed that, in fact, the surface 240 µm only reaches 80% of its full contact surface when the maximum displacement is 80 µm. This could possibly cause the lower pull-off stress values when detaching from the 240 µm surface for both FT – 12 and FT – 50 samples.

The correlations between the contact fraction and pull-off stress are plotted with the help of both experimental and simulation results (**Figure 4.9b**), in which the pull-off stress is obtained from experiments, the contact fraction is only acquired by simulations and the compressive displacement is the bridge. The pull-off stress goes up linearly with the rise of contact fraction in each case. For FT – 12 samples, the pull-off stress at the same contact fraction is not significantly influenced by the wavelength λ. On the contrary, FT – 50 samples show a wavelength λ dependence: larger λ leads to higher pull-off stress.

4.5 Discussion

Envisioning a self-adhesive microstructure for biomedical applications, especially on skin, we propose in this investigation a fibrillar array terminated by a soft, thin film, using biomedically certified materials. Roughness of the counter surface is a well-known obstacle for adhesion because it increases the elastic strain energy penalty in the adhesive attempting to conform to the rough topography. As skin exhibits roughness to various degrees, this paper explores the adhesion of novel skin adhesives to counter surfaces of various roughnesses. The counter surfaces investigated exhibited randomly distributed irregularities, from glass-like to skin-like roughness, complemented by sinusoidal model roughness. The essential observations will now be discussed in turn.

Comparison of smooth vs. rough counter surfaces: the benefit of fibrillar microstructures

A first result of our work is the observation that the microstructure did not always lead to improved adhesion: in contact with smooth counter surfaces, unstructured control samples were about three times more adhesive than fibrillar microstructures (**Figure 4.5a**). As the unstructured films can adapt well to a smooth counter surface, the micropatterning of the film-terminated microstructure does not add any advantage to the adhesive behavior; in the contrary, it may be argued that the reduced areal density of the fibrils (about 22.5% of the nominal area) will reduce the effective contact stiffness by a similar factor. Such a difference was observed in **Figure 4.5b**, where the slope of the stress-displacement data during compression differed by a factor of approximately 2. Additional contributions may be due to

the fibril-induced inhomogeneous stress fields at the interface, which could favor initiation and propagation of interfacial cracks.

The situation changes considerably when a counter surface with roughness is considered. Here, the higher compliance of the micropatterned sample with graded modulus will allow much better conformity to the peaks and valleys of the counter surface; this mechanism is clearly illustrated in the side-view pictures of **Figure 4.6b** for the case of a single-wavelength model surface. It is noteworthy that, for a surface wavelength of 480 μm, the "plateau" value of the thicker terminal layer was about twice that of the thinner layer (**Figure 4.6a**). In the "full" contact state (Figures A and C), the sample with the thinner terminal layer, FT – 12, exhibits more pronounced fibril bending than sample FT – 50. This suggests that the thicker terminal layer contributes more elastic accommodation and requires less fibril bending. As presented in **Figure 4.7b** (B and D), the detachment initiates preferentially in the valley rather than along the surface edges as previously described for the smooth surface. Empirically, it was found that the wavelength must exceed four fibril diameters (Equation 1).

Compressive behavior of microstructures: the benefit of overload protection

The behavior of a skin adhesive during attachment is also decisive for its applicability in a biomedical context. The fibrillar microstructures presented here exhibited a beneficial characteristic (**Figure 4.3d**): during compression, a plateau regime was encountered (marked "regime 2") in which the compressive stress acting on the counter surface was insensitive to compressive displacement. Mechanistically, the force plateau is linked to the buckling instability of the microfibrillar array (**Figure 4.3c** and **d**). Considering a Young's modulus, *E* of 1.1 MPa, *n* = 513 microfibrils, a fibril radius, *R* of 30 μm and the fibril height, *h* of 200 μm, the critical buckling load can be estimated by Euler buckling theory $P_b = \alpha n E \pi^3 R^4 / 4h^2$, where α = 4 for clamping of both ends.[192 25] Thus, P_b = 0.177 N and the buckling stress for the surface of 6.2 mm^2 is 28.5 kPa, which is in the same range as obtained experimentally.

This buckling event creates a "cushioning" or "overload protection", which allows for dissipation of any extra applied force through the deformation of the subsurface microstructure.[194] This effect will protect the counter surface against damage when applying

a medical device on sensitive or injured tissue.[169] The film-terminated design did not show loss of adhesion even after the fibrils were buckled, which is advantageous for reliable adhesion compared to microfibrils without film termination. This behavior differs from simple fibril microstructures, in which an overload can lead to elastic instability of the fibrils and hence detachment from the counter surface.[195 196]

Theoretical considerations of the effects of microstructure and of the terminal layer

It is finally attempted to explain some of our observations in the light of theoretical concepts. It was recently found that rough surfaces, both random and sinusoidal, become sticky when their surface energy is more than half the elastic energy needed to bring the surfaces into conformal contact.[197] Since the elastic energy for contacting nominally flat surfaces is dominated by the surface undulations near the "roll-off" wavelengths,[106] it is sufficient to consider a single representative undulation with a wavelength near roll-off. While exact treatment of a multi-layered system would require complicated transfer-matrix techniques,[198,199] simple scaling arguments are presented here. We approximate the mechanics of the fibril structure (with areal density 22.5%) as a homogeneous elastic medium with a Young's modulus *E* that is 22.5% of that of the bulk and Poisson's ratio of zero. It is further considered that a surface undulation of wavelength λ penetrates roughly a distance $\lambda/_{2\pi}$ into a semi-infinite solid, which is sometimes referred to as Saint-Venant's principle and is backed up by analytical solutions.[200]

Figure 4.10 illustrates two modes to be considered: When λ is small compared to the terminal layer thickness $h = h_{layer}$, the layer deforms elastically as if the body below, with much greater Young's modulus, provided a rigid constraint (**Figure 4.10a**, mode a). Thus, the energy of deformation is given by [201,202]

$$\frac{V_{el,1}}{A_0}(q, h, \upsilon) = \frac{qE^*}{4} c(\upsilon, qh)|\tilde{u}|^2, \tag{3}$$

where $\tilde{u}$ is the displacement amplitude, $E^* = E/(1-\upsilon^2)$ the contact modulus, $q = 2\pi/\lambda$ the magnitude of the wave vector, and *c(υ, qh)* a dimensionless geometric prefactor. At large

wavelengths (relative to the film thickness, **Figure 4.10b**, mode b), the entire sample including the layer is fully deformed and follows the undulation of the counter surface. Since the bottom medium is much stiffer than the layer, we estimate this deformation energy by evaluating Equation (3) only for the bulk/fibril body below the layer. In summary, we obtain

$$V_{el,mode\ (a)}(q) = V_{el,1}(q, h_{layer}, \nu_{layer}) \text{ and } V_{el,mode\ (b)}(q) \approx V_{el,1}(q, h_{bottom}, \nu_{bottom}).$$

Figure 4.10c displays the calculated areal deformation energies as a function of wavelength for the two different terminal layer thicknesses with and without fibril structure. It is generally seen that, with increasing wavelength (decreasing wave vector), the deformation energy decreases at first and then increases again; there is hence a defined wavelength for which adhesion is expected to be optimal. This is a result of the trade-off between higher displacement gradients at low λ and near-incompressibility at large λ. In the experimental wavelength range near the roll-off of the PSD (**Figure 4.2e**), fibril structures are predicted to require less deformation energy; consequently, they will more easily form intimate adhesive contact and exhibit a higher pull-off stress. It is also seen that the difference between 12 and 50 µm layer thickness is more noticeable for control specimens (dashed and dash-dotted line, CON – 12 and CON – 50) than for the fibrillar structures (solid lines FT – 12 and FT – 50), matching the behavior visible in **Figure 4.5a**.

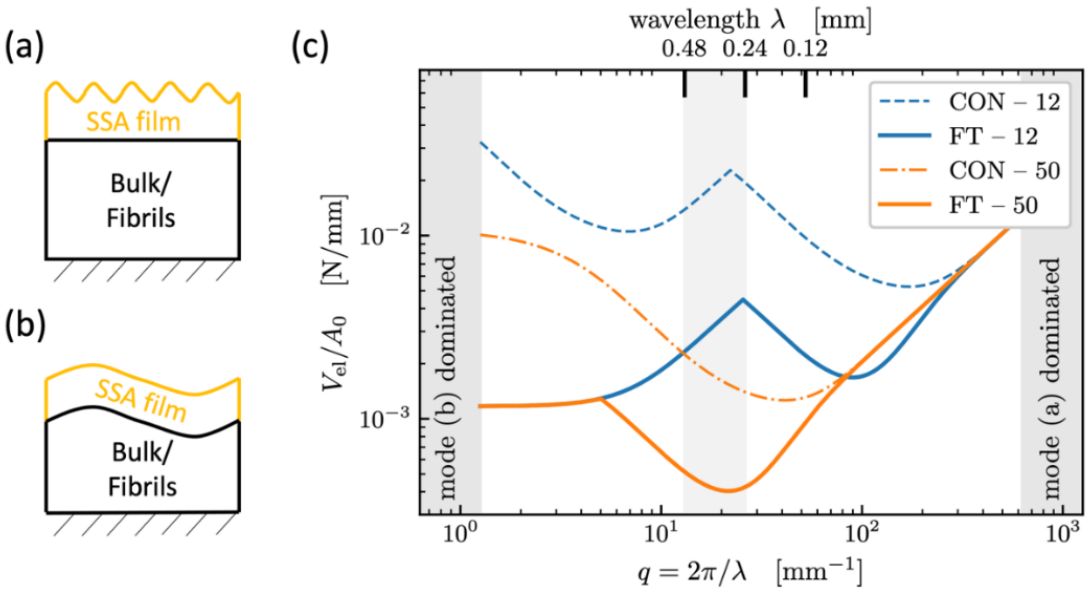

Figure 4.10: Theoretical model cases for elastic bodies with a sinusoidal counter surface. a) Mode a: wavelength λ much smaller than layer thickness, b) mode b: wavelength λ substantially exceeds layer thickness, c) calculated deformation energies (per area) as functions of wavelength λ or wave vector q. The underlying "bulk/fibril" material is assumed to be stiffer than the terminal layer, providing a rigid constraint. In agreement with experiment, the best confirmation to a counter surface with a wavelength between 240 and 480 µm (lowest deformation energy) is predicted for FT – 50 (shaded).

Considering the difference between the 12 and 50 µm film-terminated samples, we have also observed in the finite-element simulations (**Figure 4.8b**) that the thinner terminal layer creates higher stress concentrations reaching the interface to the counter surface. If the counter surface is considered as rigid and the fibrils are treated as flat punches in contact with the film, a thickness of about twice the fibril radius can already be approximated as infinitely thick in linear-elastic theory [201]. This is roughly fulfilled by the 50 µm layer (FT – 50), whereas in the FT – 12 sample the stress concentrations due to the fibrils will favor interfacial crack initiation and hence lead to earlier detachment. The fibrillar structure still improves adhesion in comparison to the control samples because it provides a more compliant background medium.[170,203]

Additionally, we estimated the conditions in which mode a dominates at all wavelengths, [201] i.e., the effect of the patterned background would become negligible. The terminal layer thickness for this condition is approximately 450 µm, which is larger than the fibril length.

4.6 Conclusion

The adhesion of fibrillar microstructures terminated by a soft film was investigated against surfaces of different roughness (from smooth to skin-like), as well as against sinusoidal model surfaces of varying wavelengths, with roughness $R_z = 50\ \mu m$ mimicking the skin. The effects of varying terminal layer thickness and of the subsurface microfibrils were investigated. The following conclusions can be drawn:

Improved tolerance to roughness: The film-terminated fibrillar microstructures exhibit improved adhesion to counter surfaces of finite roughness, typical of skin, in comparison to flat samples. Microstructured samples show decay of up to 43% with increasing roughness, while unstructured control samples have a decay of up to 98%. The reason is the better conformity of the microstructures to the surface topography due to their higher effective compliance. We presented a theoretical model of the interaction with a rough surface.

Threshold wavelength of the counter surface: Our experimental results suggest that, to ensure sufficient contact, the wavelength of the roughness must obey: $\lambda > 4D$, where *D* is the fibril diameter. The empirical threshold is attributed to a geometrical impediment of the fibrils to achieve the furthest point in the countersurface. Above this limit, adhesion can be tuned by increasing the contact area through compressive preload. These results are in agreement with Finite Element simulations, in which contact fraction during compression was evaluated.

Terminal layer thickness effect: A thinner terminal layer creates local stress concentrations and leads to earlier detachment. The thicker terminal layer reduces the influence of the stiffer background material, making the structure more compliant. A simple preliminary model consideration is presented to explain these effects.

Overload protection: When sufficiently compressed, the film-terminated microstructure exhibits elastic instability of the fibrils without loss in adhesion. This mechanism leads to a stress plateau, which protects the counter surface against overload and damage during application, a feature relevant for medical applications.

Chapter 5

Self-Adhesive Silicone Microstructures for the Treatment of Tympanic Membrane Perforations

Chapter 5. Self-Adhesive Silicone Microstructures for the Treatment of Tympanic Membrane Perforations[†]

5.1 Abstract

Inspired by the gecko foot, polymeric microstructures have demonstrated reliable dry adhesion to both stiff objects and sensitive surfaces such as skin. Microstructured silicone patches are here proposed for the treatment of tympanic membrane perforations with the aim of serving as an alternative for current surgical procedures that require anesthesia and ear canal packing. Sylgard 184 PDMS micropillars of 20 µm in diameter and 60 µm in length are topped by a Soft Skin Adhesive (SSA) MG7-1010 terminal layer, of about 25 µm thickness. The adhesion is evaluated by specially designed tack tests against explanted murine eardrums and, for comparison, against a rigid substrate. Functional effects are evaluated using auditory brainstem responses (ABR) and distortion product otoacoustic emissions (DPOAE). The adhesion strength of the microstructure and unstructured controls to explanted murine tympanic membranes is comparable (typically 12 kPa), but the microstructured patches are easier to handle by the surgeon. For the first time, partial recovery of hearing performance is measured immediately after patch application. The novel patches adhere without the need for further fixation, removing the need for ear canal packing. The proposed material design holds great promise for improving clinical treatments of tympanic membrane perforations.

5.2 Introduction

Micropatterning of polymeric materials is a powerful sustainable strategy for enhancing adhesion without the use of chemicals.[4] Such self-adhesive structures allow gentle and

[†] This chapter was published in Wiley Advanced Nanobiomed Research:

Moreira Lana, G.; Sorg, K.; Wenzel, G. I.; Hecker, D.; Hensel, R.; Schick, B.; Kruttwig, K.; Arzt, E. Self-adhesive silicone microstructures for the treatment of tympanic membrane perforations. Adv. NanoBiomed Res. 2021, 1, 2100057.
https://onlinelibrary.wiley.com/doi/10.1002/anbr.202100057

reversible adhesion in industrial robotics applications[5] and have been proposed for improved adhesive contact to human skin.[130,176,204] The principle is derived from the attachment organs of geckos, which can reversibly attach to vertical walls and ceilings.[17,27,34,205] Their adhesion is based on van der Waals interaction strongly enhanced by a compliant microfibrillar ('hairy') structure. The main advantage of such dry adhesives lies in their chemical-free adhesive function, which would allow biomedical application without the need for further attachment agents.

Our research has focused on developing microstructured adhesives specifically for contact with human skin. Depending on many factors, e.g. location, age and strain, skin can exhibit different roughness features. Trojahn and co-authors measured in 4 different skin areas, R_a ranging from 13.9 to 16.2 µm and R_z from 61.5 to 71.9 µm (where R_a is the arithmetic mean deviation from the center line and R_z is the mean roughness depth).[76,77] Roughness is the main factor reducing adhesion due to insufficient molecular contact between the surfaces.[96] To achieve good adhesion under these circumstances, several materials strategies are available: i) the dimensions of elastomeric micropillars can be chosen to optimize adhesion to a specific roughness;[110] ii) a compliant polymer film, when thinner than a critical thickness, can sufficiently conform to the surface irregularities to create reliable adhesion;[112] and iii) composite micropillars with very soft terminal layers can accommodate roughness of the countersurface.[34] Strategies ii) and iii) can be combined by designing a film-terminated structure in which arrays of micropillars are bridged at their terminal ends by a continuous compliant top layer. The mechanics of such film-terminated designs was discussed in detail by Glassmaker et al.[42] and Noderer et al.[206], who attributed their superior adhesion to a crack-trapping mechanism: the interfacial crack "feels" the spatial modulation of the local compliance and is pinned in the space between the pillars, where the energy release rate to drive crack propagation is reduced. Such a microstructure can additionally adhere to surfaces of different degrees of roughness[57] as the real contact area is increased due to the adaptation of the soft top layer and the compliant micropillars.[57,59,207]

The application proposed here for such microstructured films is the treatment of perforated the tympanic membranes (TMs). Currently, tympanic membrane perforations (TMPs), especially in persistent or chronic cases, are treated by costly surgical procedures under

anesthesia, involving the packing of the outer ear canal until the healing process is completed. This therapy impairs the patient's hearing and could implicate surgery complications.[144] Due to these risks of TMP treatments, biomaterials research started to look for promising therapeutic alternatives for TM regeneration, especially for the treatment of large or persistent perforations. Even when perforated membranes heal spontaneously, the repaired membranes can be malformed, acoustically suboptimal, and susceptible to re-perforations.[144] The time of healing and the closure rate of TMPs strongly depend on the type (acute or chronic) and size.[147,208] Recurring and chronic perforations can cause, in addition to hearing loss[209–211], severe health issues due to the risk of infections and of cholesteatoma formation.[212] A fast and mechanically reliable closure of the perforation is therefore indicated.

The TM has an important role in sound transmission to the ossicles and in protecting the middle ear. By collecting vibrations from the incoming sound waves and transforming into mechanical waves as vibrations, the TM is an important factor of the acoustic impedance system. Disturbances in this mechanical system lead to hearing impairment. This can be quantified by recording the auditory brainstem response (ABR) and by measuring the distortion product otoacoustic emissions (DPOAE). ABR signals generated in the auditory cortex can be detected by peripheral electrodes using a standard method for diagnostic purposes in humans and research purposes in laboratory animals, often along with DPOAEs.[213,214] The latter is an important frequency-specific method to detect the functional effects of middle ear disorders, such as otitis media, TMPs and discontinuity of the ossicular chain.[215–217] DPOAE measurements are a very sensitive tool to analyze mechanical alterations in the middle ear, among other things, and therefore can also be used to obtain information about the healing process of the perforated tympanic membrane.[218]

In the clinic, acute clean TMPs that are not very large and present no other complications, e.g. large destruction of the edges or involvement of the ossicular chain, are treated by unrolling, subtle correction of their edges, and overlaying a film, which should protect the middle ear and support the healing process. For larger or persistent TMPs a surgical procedure called myringoplasty, or tympanoplasty, is needed as was first described by Zöllner[219] and Wullstein.[220] An autologous film (perichondrium, cartilage, or fascia) is positioned underneath

the perforation with freshly cleaned margins. For both medical treatments, the newly introduced material needs to be kept in position by packing the outer ear canal, e.g. with a layer of silicon stripes and finally with antibiotic-impregnated gel foam. As an alternative procedure, simple silicone foils can be used to sustain the healing process, reducing the risk of ear infections and possibly improving hearing abilities for small and medium TMPs.[221,222] In a clinical study, polydimethylsiloxane (PDMS) films, in combination with immobilized collagen, were used to treat small TMPs with a success rate of 70 %.[155] We previously proposed the soft skin adhesive SSA MG7-9800 for this purpose due to its reliable but gentle self-adhesion to tissues, enabling secure adherence and atraumatic removal.[168,223] Patching perforated eardrums with self-adhesive materials in humans could therefore improve the treatment for the affected patients and has however, to our knowledge, not been reported so far.

We designed a novel self-adhesive patch in the form of film-terminated microstructured silicone film. For the micropillars, PDMS Sylgard 184 was chosen, whereas the top layer consisted of a soft skin adhesive (SSA MG7-1010). The patches were evaluated, in comparison to non-structured control samples, regarding adhesion to rigid rough substrates and to explanted murine eardrums. In addition, the functional properties for restoring hearing after closing of TMPs by the adhesive patches were evaluated by click ABR and DPOAE measurements. The resulting properties of the novel patch were extremely encouraging and suggest finalizing the preparations for clinical studies.

5.3 Material and Methods

Fabrication of film-terminated and control samples

A new film-terminated microstructure was developed using pillars of approximately 20 µm diameter and 60 µm height (aspect ratio 1:3), with hexagonal configuration and interpillar distance equal to their diameter. The pillar fabrication process consisted of two replication steps. First, a master structure with a 0.5 cm x 0.5 cm pillar array was printed on a 2.5 cm x 2.5 cm silicon wafer using a methacrylate-based resin (Nanoscribe IP-Q Resin) by two-photon lithography (Photonic Professional GT2, Nanoscribe, Eggenstein-Leopoldshafen, Germany).

The master structure was cleaned with isopropanol and gently dried using nitrogen flow. The surface of the master structure was coated with (tridecafluoro-1,1,2,2-tetrahydrooctyl) trichlorosilane (AB111444, ABCR, 97 %) upon activation in an air plasma (Atto low pressure plasma system, Electronic Diener, Ebhausen, Germany) for 5 minutes. Coating occurred via vapor deposition in reduced pressure of about 3 mbar for 15 min. A mold (negative) was thereafter replicated from the master by pouring polydimethylsiloxane (PDMS, Elastomer kit Sylgard 184, Dow Silicones, Midland, MI, USA) onto the microstructure placed in a Petri dish. After curing for 1 h at 95 °C, the mold was gently peeled and silanized using the same process as described above. Sylgard 184 was poured on the mold and degassed for 5 minutes to properly fill the cavities. Then, the excessive polymer was removed by spinning the mold at 1000 rpm for 120 s (Spin coater Laurell WS 650 MZ-23NPPB, North Wales, Pennsylvania, USA). This resulted in a homogeneous backing layer, the base for the pillars. After curing at 95 °C for 1 hour, the pillar array was gently removed from the mold and placed on a polyethylenterephthalat (PET) film to stabilize the microstructure and facilitate handling. For film-termination, first a thin MG7-1010 (Dow Silicones, Midland, Michigan, USA) film was prepared on a fluorosilicone release liner (Siliconature, SILFLU S 75 M 1R88002 clear) at 7000 rpm for 120 s and subsequently cured at 95°C for one hour. On top of this film, a second layer of MG7-1010 was prepared, again using 7000 rpm. The microstructure was placed upside down onto the uncured film and subsequently cured. Upon peeling the entire structure from the release liner, the film-terminated microstructures were used without further treatments.

The unstructured samples (to be referred to as “control sample”) were prepared by first fabricating a Sylgard film on a PET film using a doctor blade (AFA-IV, MTI Corporation, Richmond, CA, USA). The thickness of the Sylgard layer was chosen according to the amount of Sylgard used for the microstructured specimen to match the mass of the sample. The soft skin adhesive layer was added with the same procedure as the film-termination described above. All specimen dimensions were measured using an optical microscope (Eclipse LV100ND, Nikon, Tokyo, Japan) and a scanning electron microscope (FEI Quanta 400 ESEM, Thermo Fisher, USA). For the latter, specimens were sputter-coated with gold and analyzed under high vacuum, below 3 x 10^{-2} Pa, 7 kV voltage and a secondary electron detector.

Roughness of model surfaces and tympanic membranes

The roughness of the substrate surfaces made from epoxy was measured using a confocal microscope (MarSurf CM explorer, Mahr, Göttingen, Germany). Measurements were performed at three positions using a 50x objective. The roughness of the murine TM was indirectly determined by measuring silicone replicas prepared prior to the ex vivo adhesion measurements (see section 2.4). In total, 14 replicas of 7 eardrums were measured, each of them at 3 different positions of the *pars tensa*, using a 50x objective. The surface analysis was carried out using the software "Marsurf MFM Extended" on a surface of dimensions 320 µm x 320 µm. The raw data was fitted with a Gaussian filter having a cut-off length of 2.5 µm, a 7th-order polynomial and a cut-off length of 250 µm.

Adhesion measurements

Tack tests were performed using a custom-built adhesion testing device[63,184]. Normal forces were recorded using a 0.25 N load cell (ME-Meßsysteme GmbH, Hennigsdorf, Germany). The surface used for adhesion measurements was the flat face of a cylinder made from epoxy resin, replicating a frosted glass slide (Marienfeld, Lauda Königshofen, Germany). For details see.[112] Tack tests were performed using a custom-built adhesion testing device.[63,184] Normal forces were recorded using a 0.25 N load cell (ME-Meßsysteme GmbH, Hennigsdorf, Germany). The surface used for adhesion measurements was the flat face of a cylinder made from epoxy resin, replicating a frosted glass slide (Marienfeld, Lauda Königshofen, Germany). For details see.[112]

The measurements were carried out by approaching the sample to the substrate surface at a rate of 30 $m\ s^{-1}$ until a compressive preload of 30 or 60 mN was reached. The sample was held in contact with the surface for 10 seconds, and then retracted with a velocity of 10 $m\ s^{-1}$ until pull-off occurred. Each sample was measured at three different independent positions (error bars represent standard deviation). Displacements recorded were corrected for the system compliance $C = 0.13\ \mu m\ mN^{-1}$.[112] The maximum pull-off stress was calculated by dividing the force values by the nominal contact area of 2.6 mm².[112] The maximum pull-off stress was calculated by dividing the force values by the nominal contact area of 2.6 mm².

Animal experiments

All animal experiments were performed under anesthesia (auditory measurement) or ex vivo on freshly explanted TM specimens. All experiments were performed according to the German Animal Welfare Law following the EU directive 2016/63/EU for animal experiments by qualified persons. The Animal Welfare Officer of the Saarland University was informed in advance and the euthanasia methods were fully appropriate. We ensured the minimizing of discomfort, stress, and pain during the experiments by using proper anesthesia and analgesics. Furthermore, the animals were kept hydrated and the body temperature was maintained using an electric heating pad. For anesthesia, a mixture of ketamine-hydrochloride (80 $mg\ kg^{-1}$ body weight (b.w.) Ursotamin®, Serumwerk Bernburg, Germany) and xylazine-hydrochloride (10 $mg\ kg^{-1}$ b.w.; Xylazin, Serumwerk Bernburg, Germany) was injected intraperitoneally with an injection volume of 10 $ml\ kg^{-1}$ b.w. The anesthesia was maintained by injecting one-third of the initial dose intraperitoneally, typically in 30-40 min intervals. For terminal experiments, the animals were sacrificed in deep anesthesia.

Surface roughness determination and tack tests on explanted mouse TM

To analyze the adhesion of film-terminated microstructures and the non-structured control films on the murine TM, tack tests were performed on explanted TMs. These experiments were performed in accordance with EU directive 2016/63/EU for animal experiments as acute experiments. The Animal Welfare Officer was informed about them and all experiments were performed by qualified persons. The preparation of mouse tympanic membranes was performed as described previously.[168] For the preparation of the specimens, the outer ear canal was trimmed down to the bony part. The bony portion of the ear canal that covered a major part of the eardrum was carefully removed by clipping, keeping enough distance to the eardrum to ensure that the TM would not be affected by the preparation. The petrosal bone, containing the tympanic capsule with the eardrum, the middle ear ossicular chain and the cochlea, was then carefully detached from the skull bone and mounted onto a glass substrate. For the assembly, a two-component methyl methacrylate (Technovit 4004, Kulzer Technik, Hanau, Germany) was used, while ensuring free oscillation of the eardrum. After curing, the glass substrate was mounted to a sample holder. Prior to the adhesion measurements, a negative replica of the membrane was prepared using a two-component silicone (R&S Turboflex.0122996, CFPM, Tremblay-en-France, France). The components were mixed 1:1

and carefully applied onto the TM, ensuring that the whole membrane was covered, especially including the area under the residual bony parts of the outer ear canal. Additionally, it was verified that no residual air bubbles remained. The molding material was cured at room temperature for approximately 5 minutes and then gently removed. This negative mold was used to analyze the surface roughness of the TM.

The adhesion tests for real tissue were performed with a custom-made setup. Adhesive samples were cut under visual control into circular pieces with a diameter of ~1 mm using a biopsy punch and carefully fixed on the customized applicator using double-sided tape. This applicator was connected to the load cell (ME-Meßsysteme GmbH, Hennigsdorf, Germany) of our setup (see section 3.4, **Figure 4 a**). It was aligned to the sample holder under visual control to ensure positioning of the adhesive film parallel to the tympanic membrane surface (**Figure 4 b**). The applicator containing the film was moved towards the TM at a constant speed of 0.03 $mm\ s^{-1}$, until a compressive stress of approximately 25 kPa was reached, held for 10 seconds and then pulled off at 0.1 $mm\ s^{-1}$ until total detachment (**Figure 4 c**). The adhesive force was recorded and analyzed. In total, 5 tympanic membranes were used for the adhesion measurements, in intact and perforated conditions. Seven independently prepared sets of film-terminated and control patches were tested. As further validation, the control patches were tested on both the adhesive and non-adhesive sides. The experiments were performed in a random sequence.

Electrophysiological measurement of auditory function by auditory brainstem responses (ABR) and distortion product otoacoustic emissions (DPOAE) recordings

The auditory recordings were performed in a soundproofed room (*camera silenta*) on a preparation table isolated against vibrations. ABR recordings are a standard method to assess auditory function in both clinical and research setups in humans and laboratory animals.[224,225] The click ABRs were performed as described previously[226,227] to detect the auditory threshold in intact and perforated conditions as well as after applying a patch on the perforation. The auditory threshold was characterized as the lowest intensity where the Jewett´s wave complex consisting of five positive waves was identifiable.[225,228]

DPOAEs were measured with a DPOAE probe, which is used in clinical setup (UGD, Otodynamics, Hatfield, United Kingdom) as described previously.[229] DPOAE signals were elicited by two pure–tone stimuli (with frequency *f1* and *f2*) on two different speakers with a level of L1 = 55 dB SPL, L2 = 45 dB SPL and f2/f1 = 1.22 as described by Engel et al. 2006.[230] Despite a high number of emitted distortion products, current clinical DPOAE devices only make use of the emitted signal at the frequency component *2f2-f1* as a diagnostic parameter. The DPOAE amplitudes were measured between 10 and 18 kHz using 0.5 kHz steps followed by averaging and displayed as signal-to-noise-ratio (SNR).[229,231,232] DPOAE measurements were performed in three different conditions: i) intact TM, ii) perforated TM and iii) perforated TM with a patch in the same animal.

PDMS patches processed as described above were cut manually to ~ 1 mm diameter under microscope control. A perforation was induced in the posterior quadrant of the TM using a suction tube of 1.3 mm outside diameter (KARL STORZ SE & Co. KG, Tuttlingen, Germany). The DPOAEs were recorded intact, with perforation and with a patch covering the perforation. Upon completion of the set of measurements, the animal was sacrificed under deep anesthesia, the petrosal bones were explanted and the size of the TM perforation was analyzed using a microscope (MZ10F, Leica, Wetzlar, Germany) and the respective microscopy software (LASX, Leica, Wetzlar, Germany).

Statistical analysis

For statistical analysis, OriginPro 2020 software was used (OriginLab Corp., Northhampton, USA). The Shapiro-Wilk-test was applied to verify the normal distribution of the data. For the analysis of adhesive strength, the pull-off stresses were compared via a two-sided t-test after ensuring the variance homogeneity between the groups by a Levene´s test. For the analysis of the DPOAEs and the pull-off stresses ex vivo, we used a one-way analysis of variance (ANOVA). For the analysis of the ex vivo pull-off stress, the groups were independent, so ANOVA was performed for normally distributed data. The Bonferroni test was used in case of variance equality for pairwise comparisons. The results of the DPOAEs were analyzed as paired samples. For this purpose, we performed ANOVA with repeated measures for normally distributed data followed by Levene´s test for variance homogeneity. When normal

distribution or variance equality was not given, the DPOAE data were analyzed by Friedman-ANOVA followed by a post-hoc analysis with Bonferroni correction for pairwise comparisons.

5.4 Results

Film-terminated microstructured and control samples

In **Figure 5.1a**, the film-terminated microstructured architecture is schematically illustrated. The scanning electron micrograph presented in **Figure 5.1b** demonstrates that the actual aspect ratio of the pillars supporting the top layer was somewhat smaller than the 3:1 design value because the dipping process required for integration of the MG7-1010 top had created some overlap. Among all sets fabricated, thickness values of the film-terminated microstructures were 43.2 ± 1.9 µm for the backing layer, 44.7 ± 3.0 µm for the micropillars, and 24.9 ± 3.3 µm for the top layer, in total approximately 112 µm (**Figure 5.1c**). The unstructured controls consisted of a 58.9 ± 2.3 µm thick Sylgard 184 layer and a 24.1 ± 1.9 µm thick MG7-1010 top layer, with a total thickness of approximately 85 µm. The mass per area was approximately 0.08 $mg\ mm^{-2}$ for the two specimen types.

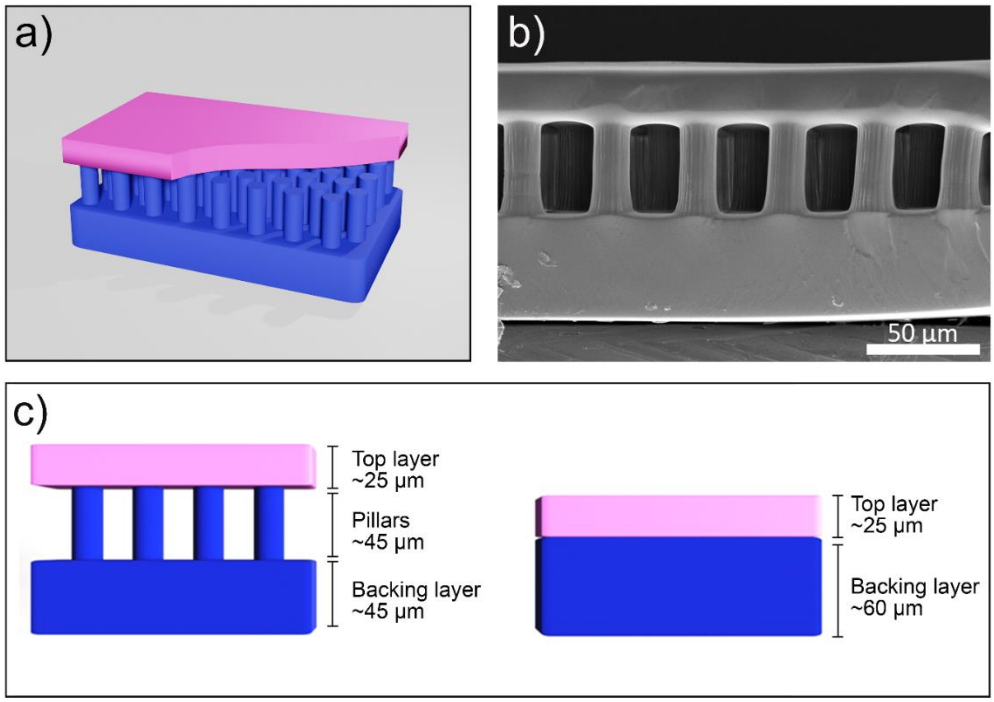

Figure 5.1. Film-terminated microstructure proposed for repair of tympanic membranes. a): 3D representation of the film-terminated design, Sylgard 184 in blue and Soft Skin Adhesive SSA MG7-1010 in pink b): Scanning electron micrograph of an actual microstructure, side view. c): Schematic illustration showing the approximate dimensions of the top layer, pillar portion and backing layer for film-terminated samples in contrast to the top layer and backing layer in the unstructured control sample.

Roughness

According to the measurements by confocal microscopy, the arithmetic mean height (R_a) of the replicas of explanted TMs was 0.14 ± 0.04 µm and 0.41 ± 0.01 µm for the epoxy substrate. Mean peak to valley roughness (R_z) values were 1.18 ± 0.42 µm for the TM replicas and 2.5 ± 0.08 µm for the epoxy substrate. Root mean square (Rms) roughness values were 90 ± 31 µm and 12 ± 1 µm, respectively.

Exemplary surface scans of the TM replicas and the epoxy substrate are presented in **Figure 5.2**. The two measurements of the TM replicas (**Figure 5.2b, c**) show some differences, which illustrate the large deviation between different measurements and will reflect on deviations in adhesion measurements, described later. The scan of the epoxy substrate is shown in **Figure 5.2d**.

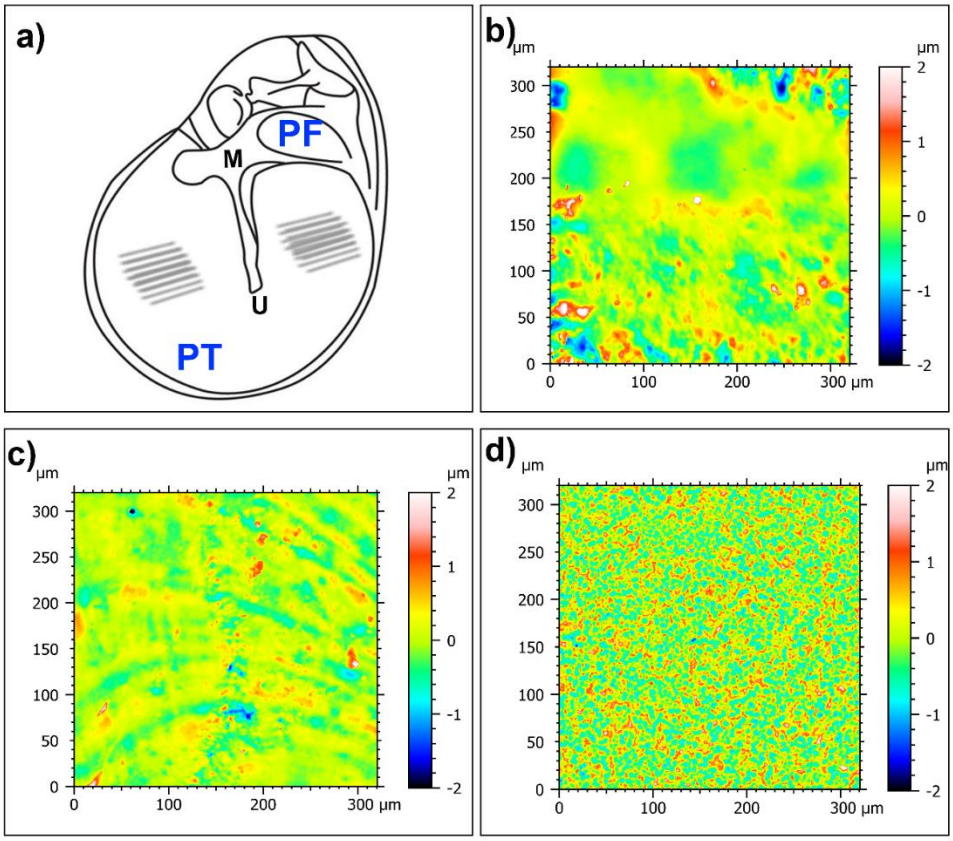

Figure 5.2. Surface roughness of murine TMs and epoxy substrate. a): Measurement locations in the pars tensa (PT), which is separated by the malleus (M) with its lowest part at the umbo (U). PF is pars flaccida. b) and c): Inverse topography scans of tympanic membrane measured on silicone replicas. d): Topography scan of the epoxy substrate. Roughness measurements were obtained from 14 replicas of 7 TMs measured in 3 different positions of the pars tensa, and for epoxy substrates in 3 independent positions.

Pull-off stress against epoxy

Figure 5.3 shows that the microstructured adhesive had a significantly higher adhesion to epoxy than the unstructured control sample: after applying a compressive pre-stress of 11 kPa, the microstructures detached at 72.7 ± 9.4 kPa and the control samples at 39.4 ± 16.5 kPa; the improvement factor was 1.89 (p-value 0.001). For a pre-stress of 23 kPa, the microstructures exhibit similar adhesion values, but the improvement factor went down to 1.27 (p-value 0.03). This was due to the strong increase of the unstructured control samples

by 56 % at the higher pre-stress, presumably due to better conformation to the substrate roughness.

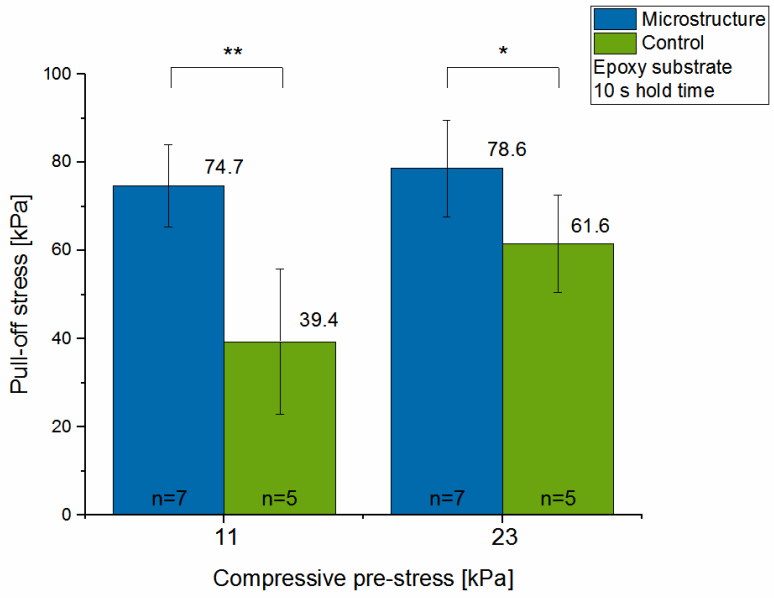

Figure 5.3. Adhesion of film-terminated microstructures and unstructured controls as determined by tack tests against epoxy substrates. The compressive pre-stress was varied from 11 kPa (left) to 23 kPa (right). The hold time at pre-stress was 10 s. Number of experiments: 7 measurements for film-terminated microstructures and 5 measurements for control samples. * characterizes $p < 0.05$ and ** indicates $p < 0.01$.

Adhesive strength against murine TMs using ex vivo tests

In **Figure 5.4a**, an explanted murine petrosal bone is shown with the TM exposed. Three different adhesive patches were tested: i) film-terminated microstructures, ii) control films with its adhesive side (MG7-1010 layer) adhered to the TM, and iii) control films with non-adhesive backside (Sylgard 184 layer). The custom-made sample holder was used to align the explanted TM in a 90-degree angle to the patch applicator, as displayed in **Figure 5.4b, c**. As shown in Figure 4 a, the patches were positioned to fully cover the perforation. Care was taken that the patch had still enough overlap with the remaining membrane to ensure its adhesion. The size of an average perforation was about 700 µm by 500 µm; this amounted to

roughly 10 % of the total area of the murine tympanic membrane (with typical dimensions of 2 mm x 2 mm) and approximately 40% of the patch area (1 mm diameter).

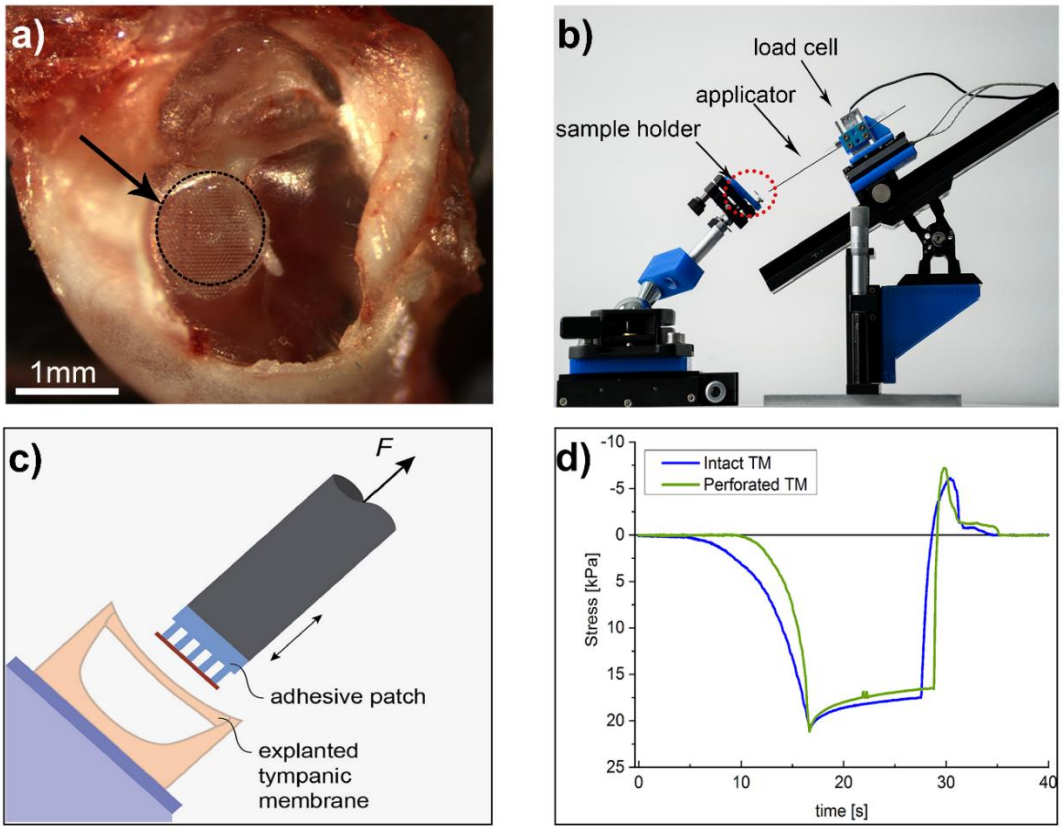

Figure 5.4. Ex vivo adhesion tests on intact and perforated murine TMs. a): Photograph of a film-terminated microstructured patch (indicated by the black arrow + dotted line) covering a perforation in the upper posterior quadrant of the murine TM. b): The measurement setup consisting of an adjustable sample holder to fix the explanted tympanic membrane and the adhesive patch mounted on a motorized applicator equipped with a load cell. c): Illustration of the test procedure indicated in b) as red dotted circle: TMs with petrosal bone mounted on a glass substrate was contacted by the adhesive patch, ensuring parallel contact. d): Exemplary stress vs. time curve: The compressive pre-stress of approximately 25 kPa was held for 10 s and the patch detached completely from the intact (blue line) or perforated (green line) TM at stresses of about 8 kPa. Positive values indicate compressive stress, and negative indicate tensile stress.

Exemplary stress vs. time curves (**Figure 5.4d**) for measurements on intact (blue) and perforated (green) TMs demonstrate the gradual increase in the compressive pre-stress up to a set value of ~25 kPa. The position was held for 10 s, which was accompanied by some slight relaxation possibly due to the soft top layer. Upon retraction, patches detached at various tensile loads. The detachment is typical for tack measurements of soft materials.[60]

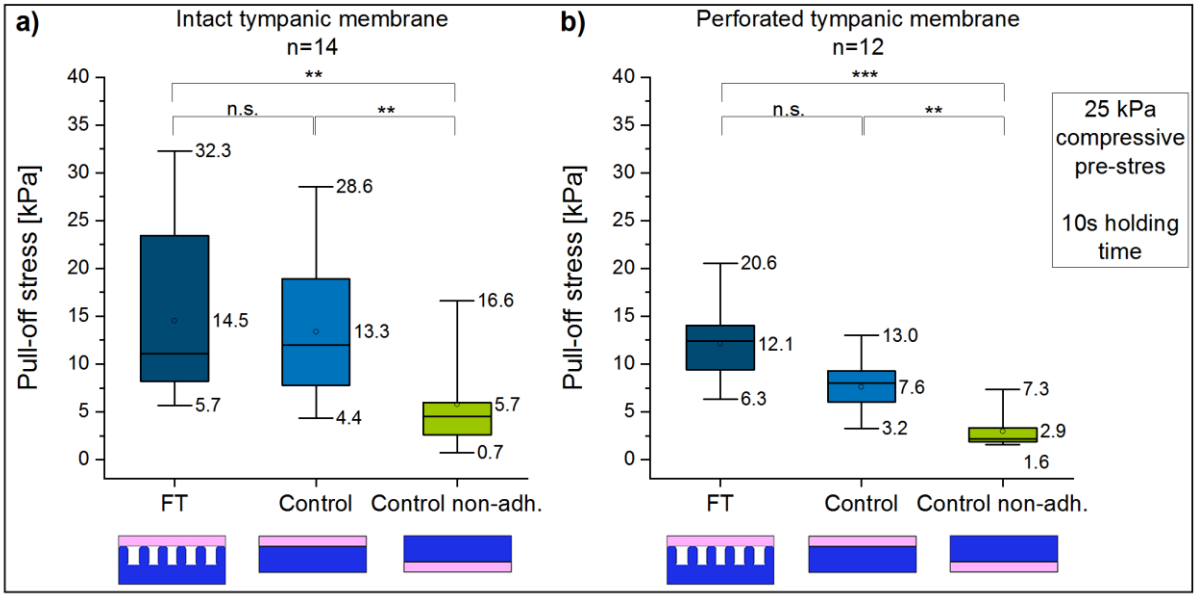

Figure 5.5. Pull-off stress for intact (a) and perforated (b) explanted TMs. Samples were film-terminated microstructures (FT, dark blue boxes) and unstructured control films with their adhesive side (Control, light blue boxes) and their non-adhesive (non-adh., green boxes) side in contact. Number n indicates independent measurements. ** indicates $p < 0.01$.*** indicates $p < 0.001$; n.s.= non-significant.

Our results on intact TMs (**Figure 5.5a**) demonstrated that the adhesive strength of the film-terminated microstructure patches was significantly higher compared to the non-adhesive, unstructured control ($p = 0.002$) but not higher than the adhesive side of the control sample. The mean pull-off stress of microstructured patches was 14.5 ± 8.8 kPa, with a maximum of 32.3 kPa and a minimum of 5.7 kPa. Mean value for the adhesive control was 13.3 ± 7.2 kPa and 5.7 ± 4.6 kPa for the non-adhesive control. The mean pull-off stress of the film-terminated microstructured patches was approximately 9 % higher, but not statistically significant,

compared to the adhesive control (p = 1). An explanation for the large deviation probably relates to large variations of the explanted TMs and the conditions of the ex situ adhesion measurements.

On the perforated TM (**Figure 5.5b**), the pull-off stress values were overall reduced compared to the intact condition. In the adhesive and non-adhesive control sample adhesion decreased by 43 % and 49 %, which is comparable to the loss of contact area due to the perforation; by contrast, microstructured patches suffered only a 17 % reduction. The adhesion of the film-terminated microstructure (p-value 0.002) and the adhesive, unstructured control (p-value 0.006) was significantly higher than the non-adhesive control. The difference between the microstructured adhesive patches and the adhesive control samples were higher than before (14.5 to 13.3 kPa vs. 12.1 to 7.6 kPa), but again not statistically significant (p = 0.14).

Physiological effects on the hearing performance

The results of the click ABR recordings demonstrated that the hearing threshold significantly increased after perforation from 12 dB SPL to 34 dB SPL in both groups, which translates into an increase of 283 % (p-value 0.003 and 0.01 respectively). Covering the perforation with patches led to a statistically non-significant decrease of the threshold in both groups with microstructured patches as well as unstructured control patches (**Figure 5.6a, b**).

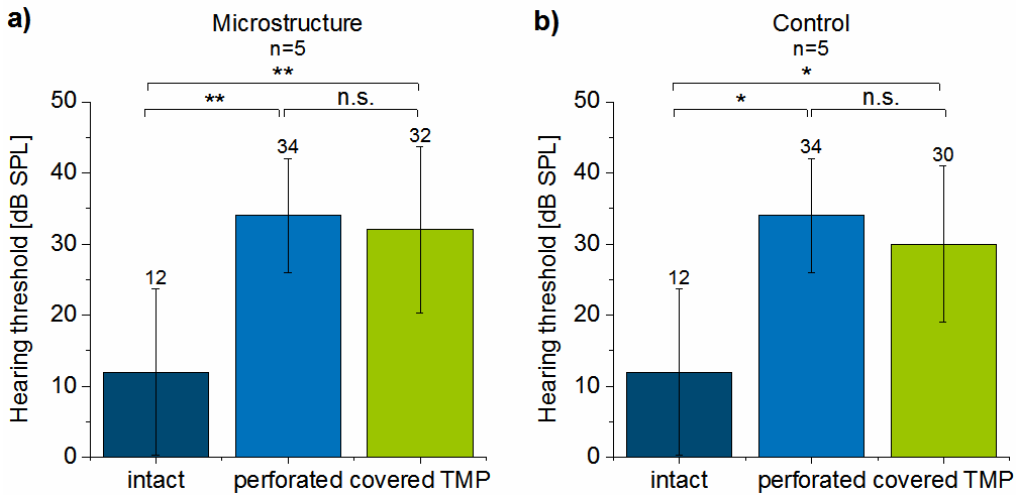

Figure 5.6 Analysis of the effects of perforation and covering of the TMP with microstructured (a) or control (b) patches on the hearing threshold, recorded by click-ABR in contrast to intact

condition. The hearing threshold significantly increased after perforation from 12 to 34 dB SPL in both cases. After applying microstructured patches (a), the threshold decreased non-significantly to 32 dB SPL. After applying control patches (b), the threshold decreased non-significantly to 30 dB SPL. * indicates $p< 0.05$ ** indicates $p< 0.01$; n.s.= non-significant.

The click-ABR is testing however the cumulative hearing activation overlapping the induced activation of all frequencies included in the click applied. The technique is therefore not sufficiently sensitive for judging the hearing improvement at individual frequencies through patch application. Therefore, to analyze the effects of closing the perforation in a more sensitive and frequency-specific manner, DPOAE recordings were performed after ABR measurements. The results of the in vivo DPOAE measurements in anesthetized mice with intact, perforated TM were compared after the closure of the perforation with the two different patches, i) the film-terminated microstructured patch and ii) the unstructured adhesive control (**Figure 5.7a, b**). Through this, a difference between the lower frequencies (10-15 kHz) and the higher frequencies (15-18 kHz) could be measured.

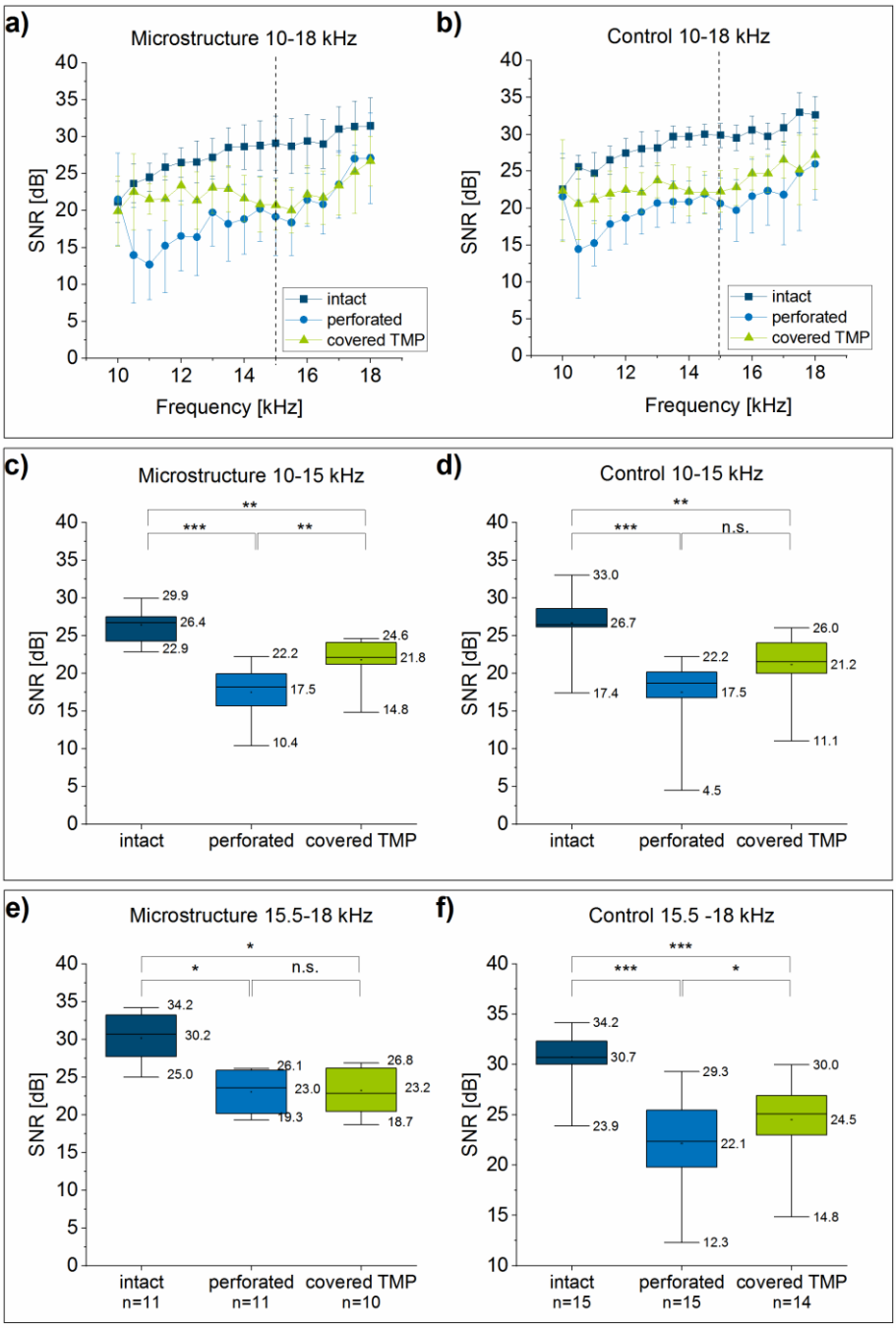

Figure 5.7. Hearing function in intact, perforated and patched condition as measured by DPOAE. DPOAEs after treatment with microstructured patches (a, green data) showed an increase in the lower frequency range, whereas the control (b) enhanced all frequencies compared to the perforated condition. c-d: Averaged signal-to-noise ratios (SNRs) point to a significant increase in DPOAE signals after patching compared to the untreated perforated TM between 10-15 kHz using the microstructure patches (c). Averaged SNRs were not significantly enhanced after applying control patches (d). e-f: Averaged SNRs in between 15.5-

18 kHz. Microstructure patches lead to a non-significant increase in SNRs (e) whereas in this frequency range, the application of control patches led to a significant increase in SNRs (f). * indicates $p < 0.05$, ** indicates $p < 0.01$ and *** indicates $p < 0.001$, n.s.= non-significant. The number of replicates is indicated below the plots in e and f.

The averaged DPOAEs between 10 and 15 kHz demonstrated an improvement after applying microstructured patches (**Figure 5.7c**). Here, the DPOAE signals dropped from 26.4 ± 2.3 dB in intact condition, by ~34 %, to 17.5 ± 3.8 dB after perforation ($p = 1.27*10^{-6}$). The application of film-terminated microstructure led to a highly significant increase to 21.8 ± 2.9 dB (Figure 7 c) corresponding to + 25 % ($p = 0.006$). By contrast, in the group treated with control adhesives (**Figure 5.7d**), the same proportional decrease was followed by an increase by ~ 21 % to 21.2 ± 4 dB, which is statistically not significant ($p = 0.06$). In the higher frequency range, from 15.5 to 18 kHz (**Figure 5.7 e, f**), the DPOAE signals decreased after perforation by ~ 24 % from 30.1 ±3.3 dB to 23 ± 2.8 dB for the microstructure and by ~ 28 % from 30.7 ±2.4 dB to 22.1 ±4.9 dB for the control group. The application of the film-terminated microstructure led to a non-significant improvement from 23 to 23.2 dB being ~+ 0.7 % of the DPOAEs ($p = 1$), whereas the application of control films led to a significant increase by about 10% from 22.1 to 24.5 dB ($p = 0.02$). In none of these measurements, full recovery of the DPOAE levels to intact levels was achieved by patching in the acute herein presented conditions.

Since mass and damping are essential parameters to be considered in analyzing the vibratory characteristics of a structure, we also investigated the effects of applying microstructured and control patches (in the thin and additionally coarser dimensions ~ 300 µm total thickness) on the intact membrane and gained more information on the influence of patching on the sound conduction of the TM (**Figure S1, in the supplementary information (SI)**). In all cases, the DPOAE signals were significantly reduced after patch application, especially for the coarser, more massive patches. When applied on the perforated membrane (**Figure S2, in the SI),** the coarser patches had no significant effect on the hearing function in comparison to the perforated condition.

From the surgeon's perspective, handling and application of the microstructured patches was more precise than for the controls, possibly because the pressure was more easily distributed through the more compliant structure onto the thin TM. Additionally, the microstructure adhered less to the thin forceps allowing easier adjustments of its position.

5.5 Discussion

In an attempt to improve current therapeutic strategies for surgical interventions on ruptured tympanic membranes, we investigated a novel silicone microstructured patch in experiments with artificial surfaces and in a mouse model. Three main aspects will be discussed in turn: roughness of the tympanic membrane, adhesive properties of the patch and its effect on hearing performance.

Roughness characterization of the murine TM

The height profiles in Figure 2 b and c are, to our knowledge, the first reported roughness data for tympanic membranes of mice. The eardrum replicas are believed to closely match the conditions of the real murine membrane although slight material shrinkage could have affected the results.[112] The data showed relatively smooth surfaces for the TM (R_a ~ 0.14 µm and R_z ~ 1.18 µm), in comparison, for example, to the roughness of human skin reported in literature (R_a ~ 13-16 µm and R_z ~ 61-71 µm).[77] It should however be noted that singular values of R_a or R_z are insufficient descriptors of complex rough surfaces; a full analysis of the surface roughness using a power spectrum, as was performed for skin e.g. by Kovalev et al. (2014), was beyond the scope of the present paper.[107]

As a model surface, we chose an epoxy replica of frosted glass, whose roughness profile was comparable but did not fully match that of the eardrum. The epoxy exhibited a more homogeneously distributed roughness than the tympanic membrane, with higher R_z roughness values.

Adhesion properties of the patches

Against the epoxy model surface, our film-terminated microstructures demonstrated, for all tested parameters, higher adhesion in comparison to unstructured controls (Figure 3). This very likely reflects the previously studied crack trapping mechanism,[42,206] possibly in combination with the reduced effective modulus which facilitates adaptation to surface roughness. The advantage of the microstructure was especially pronounced (almost by a factor 2) for the smaller pre-stress value (11 kPa). For the larger pre-stress (23 kPa), on the other hand, the improvement was only about 27 %. A possible explanation is the very soft top layer, which adapts to the surface topography leading to complete contact and a maximum pull-off stress when the pre-stress is sufficiently high.[57,58] The high adhesion for small pre-stress could be beneficial for future application in humans, as smaller forces exerted by the surgeon will lower the likelihood of damaging the TM.

As a next step, we evaluated the adhesion of the patches on explanted tympanic membranes of mice. This experiment was performed, to our best knowledge, for the first time in the literature and required the design of a dedicated ex vivo measurement set-up. First, it was found that the adhesion values were generally lower for the perforated TM compared to the intact TM, presumably due to the reduction in actual contact area. An additional effect could be the reduced tension of the *pars tensa* after perforation, which would lead to a less defined contact and make the countersurface more compliant.[233]

Second, the adhesion performances of the microstructure and the control were very similar, the difference was not statistically significant for both the intact and the perforated condition.

A third observation is the generally lower adhesion to the eardrum than to the epoxy model surface. This is not surprising as the two substrate materials differ greatly in elastic modulus and geometric complexity (i.e. the concave curvature of the eardrum vs. a nominally flat epoxy surface). A related aspect was that the two test setups used differed in stiffness. Still our approach follows common practice in standardized testing of medical adhesives, where adhesion is measured against steel substrates and empirical correlations to skin adhesion are assumed.[234,235]

In more quantitative terms, the top layer thickness necessary to accommodate the roughness characterized by R_z can be estimated. Following Davis et al.[170] and Fischer et al.[112], adhesion will be insensitive to roughness above a critical film thickness given approximately by:

$$h_{crit} \approx R_z^2 \cdot \frac{E_{eff}}{W_{ad}} \quad (1)$$

where E_{eff} is the effective modulus and W_{ad} the work of adhesion, assumed to be $50\ mJ\ m^2$. For a film made of MG7-1010 with a Young's modulus of 250 kPa[185] on the tympanic membrane ($R_z = 1.18$ µm), $h_{crit} \approx 7\ \mu m$, which is well below the thickness of the top layer (~25 µm). In contrast, for the rougher epoxy substrate, $h_{crit} \approx 32\ \mu m$, which is close to the top layer thickness. These results indicate that the adhesion on the epoxy substrates must benefit from the compliance of the underlying microstructure whereas that on the explanted TM is solely associated with accommodation by the soft top layer, as in the control sample. Although the present results for microstructured patches did not confirm improved adhesion to murine eardrums, microstructures are expected to benefit in clinical applications where adhesion must be ensured to rougher human TMs. Work along these lines is currently in progress.

Another important argument in favor of our microstructured patches is the experience gained in the animal experiments that indicated that these patches proved easier to apply to the murine TM. The patches allowed for better gripping, were easier to handle and less prone to rolling-up. This can be explained by comparing the bending stiffness of both samples (calculations shown in Supplementary). The calculated value of bending stiffness is almost 2.3 times higher for the microstructure than the control sample (see Figure S3 and Section 1 in the SI). Also, the more even distribution of the compressive pre-stress improves the integrity of the remaining TM and ensures homogeneous adhesion without causing macroscopic damage of the sensitive membrane during removal. The film-terminated design offers the advantage, over bare micropillars, of proper sealing of the perforation especially along the perforation margins. This restores, at least partially, the acoustic and protective properties of the TM.

One further advantage of the film-terminated microstructures could be the insertion of inflammation- and infection-suppressing agents, e.g. cortisone or antibiotics between the pillar portions. The porosity of the top layer would allow diffusion through the material directly to the desired target location. This could result in an engineered release system allowing drug application over a predetermined time.[236,237]

Functional effects on hearing ability

To our knowledge, we report here for the first time that appropriately designed adhesive patches have a positive impact on the hearing ability during the healing phase. DPOAE signals were significantly improved immediately following application of microstructured or control patches (**Figure 5.7**). The hearing threshold using click-ABR remained largely unaffected (**Figure 5.6**) due to the characteristics of click tones used in ABRs containing a wide range of frequencies applied simultaneously.

The frequency-specific analysis of DPOAE demonstrated that microstructured patches enhanced especially the lower frequencies (up to 15 kHz), whereas control patches improved the higher frequency range (between 15.5 and 18 kHz) (**Figure 5.7**). After translation to the much thicker human eardrum (thickness ~120 µm compared to ~5 µm for the mouse), these damping effects are expected to be much reduced in the final clinical application. Overall, the results will need to be newly evaluated in humans due to different dimensions of the eardrum.

The patches cannot fully restore the function of the damaged eardrum in the mouse model. This is very likely due to the added mass, which influences the acoustic impedance and dampens sound conduction. This effect was proven by the reduction in DPOAE levels after applying patches to intact TMs (Figure S1). In evaluating these effects, the correlation of DPOAE signals with the state of the TM requires further discussion. In general, the signal level is strongly dependent on the anterograde and retrograde middle-ear transmission and is hence influenced by mechanical changes in the outer ear and middle ear, such as increased mass or stiffness. As a result, the middle ear constitution influences the DPOAE quality twice, by affecting the incoming tones in the inward-direction and the returning DPOAE signals in

the outward direction.[218] DPOAEs are therefore valuable in detecting not only sensorineural but also conductive hearing loss[216] and are routinely used in clinical diagnosis.[238–240] In their study on gerbils, Dong et al.[218] analyzed the effects of TM perforations and altered middle ear transmission conditions on the generation of DPOAEs. DPOAEs were found to be measurable up to perforation sizes covering about half the tympanic membrane. DPOAE thresholds were not totally restored to normal after 4 weeks of incubation, especially at higher frequencies (>10 kHz). The fact that DPOAE signals did not totally recover even after closure of the TM perforation was ascribed to an incompletely restored middle ear transmission.

The immediate improvement of the auditory function in mice, as suggested by our study, would be advantageous for the treatment of patients, who would also benefit from a free ear canal during the healing phase. According to most studies of the healing time of TMs, we expect a retention time of more than 4 weeks of the patch on the perforated membrane.[241–243] In the study of Farhadi et al.[155], collagen-covered PDMS patches applied to long-standing, small perforations in 10 patients had an overall success rate of 70 % after one month. These patches had to be fixated by gel foam, which led to an inevitable conductive hearing loss.

Although less quantifiable, the surgeon's experience with the microstructured patches will be an important factor in their clinical success. The generally positive perception with regard to ease of handling, coupled with the potential benefits to the patient during and after the healing period, enhances the chances of a successful translation of these novel microstructured patches into clinical practice.

5.6 Conclusions

We present, for the first time, the design and fabrication of microstructured, film-terminated silicone patches for application on tympanic membrane perforations. These structures were tested first on relatively rough artificial rigid surfaces, where they demonstrated higher pull-off stresses compared to the unstructured controls. The adhesion of both types of patches, tested on murine explanted tympanic membranes using a customized setup, was similar for

both samples. We foresee, however, a positive effect of microstructured patches on human tympanic membranes, which exhibit greater roughness. Additionally, the patches allow proper sealing of the perforation and may avoid the entrance of pathogens into the middle ear. In a living animal model, the hearing function, investigated by DPOAE signals, was partially restored immediately after patch application. The microstructured patches allowed for better gripping by the surgeon and were easier to handle. They offer great potential for future treatment of patients suffering from a TMP. Further studies of these novel silicone patches, regarding their effects on healing and long-time behavior, are underway to ensure safe and effective clinical treatment of TMPs.

5.7 Supporting Information

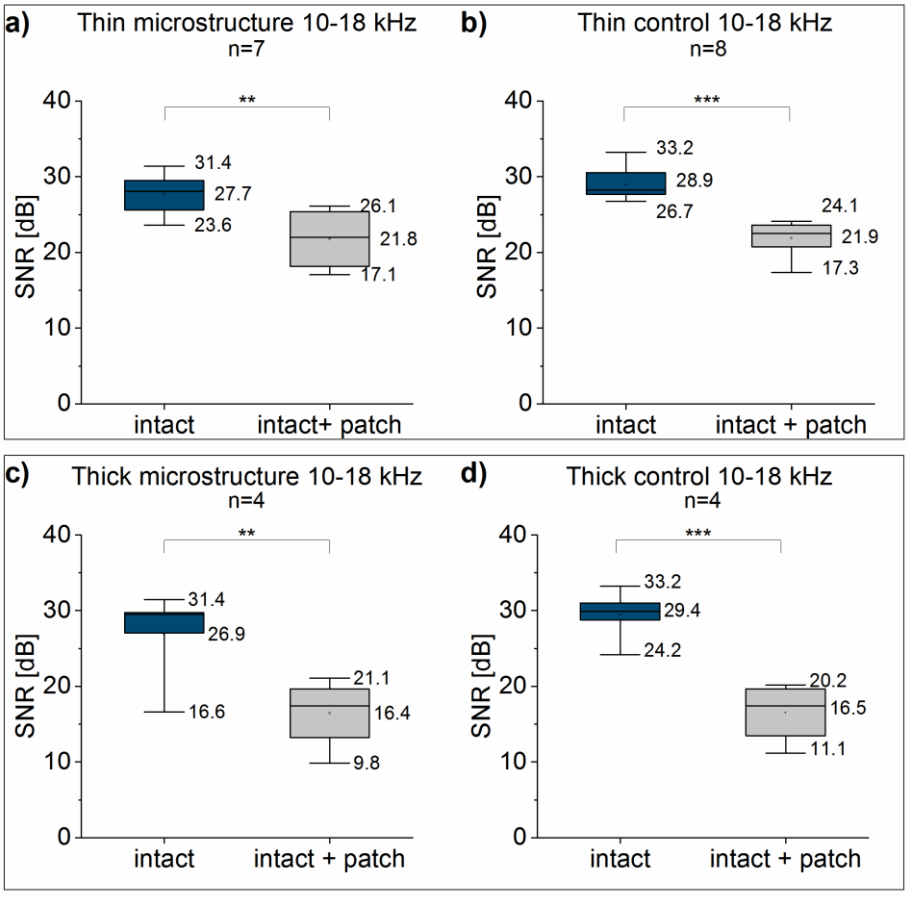

Figure S1. Analysis of the hearing function via DPOAE measurements over the frequency range of 10-18 kHz only on intact condition: The DPOAE signals on intact membranes without a patch (intact) and after application of thin (a, b) or thick (c, d) microstructure and

unstructured control patches (intact + patch). The DPOAE signals were significantly decreased after application of patches on the intact TM in all cases. ** indicates $p < 0.01$, *** indicates $p < 0.001$. The number of replicas is indicated above each plot.

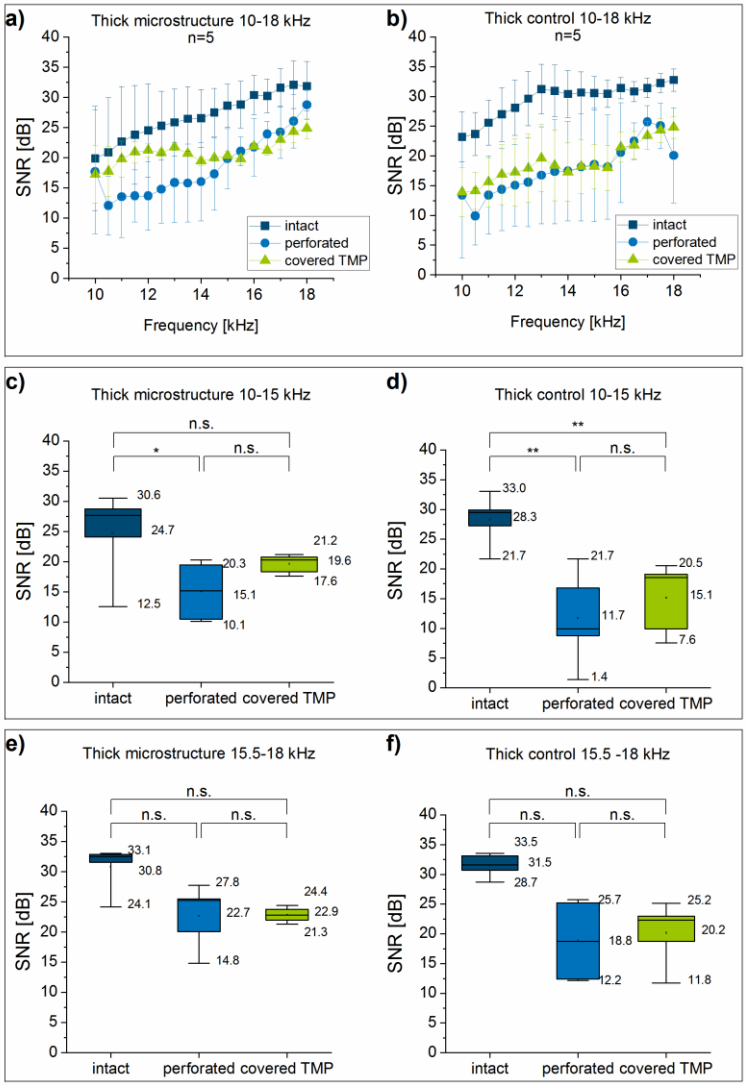

Figure S2. Analysis of the hearing function by DPOAE measurements after the application of thick microstructured patches (a, c, e) and related unstructured thick control patches (b, d, f) in comparison to the intact and perforated condition. The average measurements demonstrated significantly lower DPOAE signals in the frequency range from 10-15 kHz after perforation that could not be increased by patching of the perforation, neither by thick microstructures or thick control patches (c, d) .In the higher frequency range, no significant change in any conditions could be observed, also (e, f). * indicates $p < 0.05$, ** indicates $p < 0.01$ and n.s.= non-significant. The number of replicas is indicated in a and b (n=5).

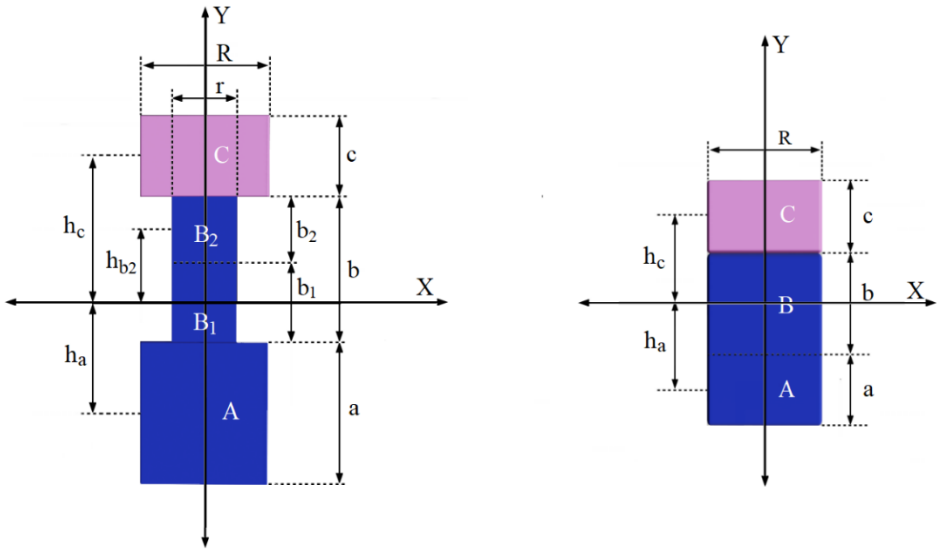

Figure S3. Schematic representation of the film-terminated microstructure (left) and control sample (right) in the coordinate system $x - y$ for calculating the plane strain bending stiffness. Portions marked in blue and pink correspond to the silicones Sylgard 184 and SSA MG7-1010, respectively. Sections A, B_1, B_2, and C were used to calculate individual moments of inertia (see Section 1). The width of the designs within its periodic boundary conditions is R, the width (diameter) of the fibrils is r, the height of each section is a, b_1, b_2, and c, and the distances of the center of mass for each section to the neutral axis X are, h_{b1}, h_{b2}, h_c.

Section 1. Calculation of the bending stiffness

The (plane strain) bending stiffness, k of the film-terminated microstructure and the control is EI, where E is the Young's modulus and I is the second moment of inertia, as illustrated in Figure S3. To calculate the second moment of inertia, both designs were sectioned into several areas with I_i, where i refers to the individual sections of the designs. Subsequently, these values were summed up using the parallel axis theorem.

The individual second moment of inertia for sections A, B_1, B_2, and C are given as:

$$I_{B1} = \frac{b_1^3 r}{12}, \tag{S1}$$

$$I_{B2} = \frac{b_2^3\, r}{12} + A_{B2}\,.\,h_{b2}^2, \tag{S2}$$

$$I_A = \frac{a^3\, R}{12} + A_A\,.\,h_a^2, \tag{S3}$$

$$I_C = \frac{c^3\, R}{12} + A_C\,.\,h_c^2, \tag{S4}$$

where a, b_1, b_2, c, r, R are the width and length; h_a, h_{b2}, and h_c are the distances from the neutral axis to the center of mass of the respective areas; and A_A, A_{B2}, and A_C are the areas of each section, as illustrated in Figure S3. From eq. S1-4, the bending stiffness is given as:

$$k = E_A I_A + E_{B1} I_{B1} + E_{B2} I_{B2} + E_C I_C, \tag{S5}$$

where E_A, E_{B1}, E_{B2}, and E_C are the Young's moduli of each section. Hence, the bending stiffness of the film-terminated microstructure is $5.68 \times 10^{-12}\ \mathrm{Nm}^2$ by considering that modulus for Sylgard 184 is $E_A = E_{B1} = E_{B2} = 2.7\ \mathrm{MPa}$ and for SSA MG7-1010 is $E_C = 250\ \mathrm{kPa}$. Similarly, the bending stiffness of the control specimen can be calculated that gives $2.45 \times 10^{-12}\ \mathrm{Nm}^2$, which is about 40% of the bending stiffness of the microstructure.

Chapter 6

Patent: Krafttolerante Mikrostruktur

Chapter 6. Krafttolerante Mikrostruktur‡

(12) NACH DEM VERTRAG ÜBER DIE INTERNATIONALE ZUSAMMENARBEIT AUF DEM GEBIET DES PATENTWESENS (PCT) VERÖFFENTLICHTE INTERNATIONALE ANMELDUNG

(19) Weltorganisation für geistiges Eigentum
Internationales Büro

(43) Internationales Veröffentlichungsdatum
25. August 2022 (25.08.2022)

WIPO | PCT

(10) Internationale Veröffentlichungsnummer
WO 2022/175150 A1

(51) Internationale Patentklassifikation:
A61B 17/30 (2006.01) *A61F 2/16* (2006.01)
A61B 17/28 (2006.01) *C09J 7/00* (2018.01)
A61F 9/007 (2006.01)

(21) Internationales Aktenzeichen: PCT/EP2022/053205

(22) Internationales Anmeldedatum:
10. Februar 2022 (10.02.2022)

(25) Einreichungssprache: Deutsch

(26) Veröffentlichungssprache: Deutsch

(30) Angaben zur Priorität:
10 2021 103 895.2
18. Februar 2021 (18.02.2021) DE

(71) Anmelder: **LEIBNIZ-INSTITUT FÜR NEUE MATERIALIEN GEMEINNÜTZIGE GMBH** [DE/DE]; Campus D2 2, 66123 Saarbrücken (DE).

(72) Erfinder: **KRUTTWIG, Klaus**; Rohrbacher Str. 44, 69115 Heidelberg (DE). **MOREIRA LANA, Gabriela**; Graf-Johann-Straße 6, 66121 Saarbrücken (DE). **MOH, Karsten**; Kiefernstr. 4, 66440 Blieskastel-Brenschelbach (DE). **ARZT, Eduard**; Schinkelstraße 9, 66123 Saarbrücken (DE).

(74) Anwalt: **PATENTANWÄLTE GIERLICH & PISCHITZIS PARTNERSCHAFT MBB**; Gerbermühlstraße 11, 60594 Frankfurt am Main (DE).

(81) Bestimmungsstaaten *(soweit nicht anders angegeben, für jede verfügbare nationale Schutzrechtsart)*: AE, AG, AL, AM, AO, AT, AU, AZ, BA, BB, BG, BH, BN, BR, BW, BY, BZ, CA, CH, CL, CN, CO, CR, CU, CZ, DE, DJ, DK, DM,

(54) **Title:** FORCE-TOLERANT STRUCTURE

(54) **Bezeichnung:** KRAFTTOLERANTE STRUKTUR

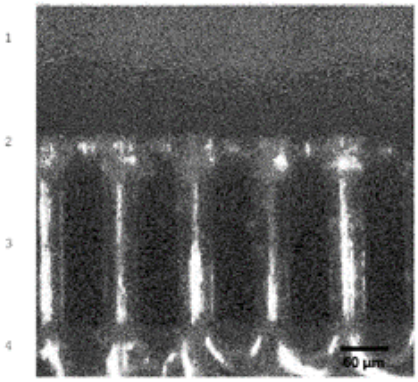

Fig. 1

(57) **Abstract:** The invention relates to a structure which enables the force transmitted to an object by the structure to be checked, a maximum force not being exceeded in a particular region. The structure comprises a support layer, wherein: a plurality of protrusions are arranged on said support layer, each of which comprises at least one trunk with an end face pointing away from the support layer; at least one further layer can be arranged on the end faces, which further layer is designed as a film; and said layer comprises as a surface at least one layer which has a lower modulus of elasticity than the respective protrusion.

(57) **Zusammenfassung:** Die Erfindung betrifft eine Struktur, welche eine Kontrolle der durch die Struktur auf ein Objekt übertragenen Kraft erlaubt, wobei in einem bestimmten Bereich eine maximale Kraft nicht überschritten wird. Die Struktur umfasst eine Träger-

[Fortsetzung auf der nächsten Seite]

WO 2022/175150 A1

‡ This chapter was published on 25.08.2022 under the international publication number WO002022175150A1 at the German Patent and Trade Mark Office.

WO 2022/175150 A1

DO, DZ, EC, EE, EG, ES, FI, GB, GD, GE, GH, GM, GT, HN, HR, HU, ID, IL, IN, IR, IS, IT, JM, JO, JP, KE, KG, KH, KN, KP, KR, KW, KZ, LA, LC, LK, LR, LS, LU, LY, MA, MD, ME, MG, MK, MN, MW, MX, MY, MZ, NA, NG, NI, NO, NZ, OM, PA, PE, PG, PH, PL, PT, QA, RO, RS, RU, RW, SA, SC, SD, SE, SG, SK, SL, ST, SV, SY, TH, TJ, TM, TN, TR, TT, TZ, UA, UG, US, UZ, VC, VN, WS, ZA, ZM, ZW.

(84) Bestimmungsstaaten *(soweit nicht anders angegeben, für jede verfügbare regionale Schutzrechtsart)*: ARIPO (BW, GH, GM, KE, LR, LS, MW, MZ, NA, RW, SD, SL, ST, SZ, TZ, UG, ZM, ZW), eurasisches (AM, AZ, BY, KG, KZ, RU, TJ, TM), europäisches (AL, AT, BE, BG, CH, CY, CZ, DE, DK, EE, ES, FI, FR, GB, GR, HR, HU, IE, IS, IT, LT, LU, LV, MC, MK, MT, NL, NO, PL, PT, RO, RS, SE, SI, SK, SM, TR), OAPI (BF, BJ, CF, CG, CI, CM, GA, GN, GQ, GW, KM, ML, MR, NE, SN, TD, TG).

Veröffentlicht:

— *mit internationalem Recherchenbericht (Artikel 21 Absatz 3)*

schicht, wobei auf dieser Trägerschicht eine Vielzahl von Vorsprüngen angeordnet sind, die mindestens jeweils einen Stamm mit einer von der Trägerschicht wegweisenden Stirnfläche umfassen, wobei auf den Stirnflächen mindestens eine weitere Schicht angeordnet sein kann, welche als Film ausgebildet ist, wobei diese Schicht als Oberfläche mindestens eine Schicht umfasst, welche einen geringeren Elastizitätsmodul aufweist als der jeweilige Vorsprung.

6.1 Beschreibung

6.1.1 Gebiet der Erfindung

Die Erfindung betrifft eine Struktur, welche eine Kontrolle der durch die Struktur auf ein Objekt übertragenen Kraft erlaubt, wobei in einem bestimmten Bereich eine maximale Kraft nicht überschritten wird.

Häufig gibt es bei empfindlichen Substraten das Problem, dass beim Aufbringen auf diese Substrate eine bestimmte Kraft nicht 10 überschritten werden darf, um das Substrat oder das aufzubringende Objekt nicht zu beschädigen. Gleiches gilt auch für das Belasten von empfindlichen Objekten, beispielsweise bei Greifern .

Bekannte Systeme zur Dämpfung und Kraftbeschränkung sind beispielsweise Schäume.

Die Adhäsion auf rauen Oberflächen ist häufig problematisch. Insbesondere im biologischen Bereich zeigen viele Klebstoffe nur unzureichende Eigenschaften. Gleichzeitig besteht auch das Problem, dass Klebstoffe nur unzureichend kompatibel sind mit biologischen Oberflächen.

Eine Alternative bieten trockenadhäsive Oberflächen, wie bspw. Geckostrukturen, welche ohne die Vermittlung durch Klebstoffe eine Adhäsion auch an rauen Oberflächen zeigen können. Allerdings verschmutzen solche Strukturen leicht.

Bei operativen Eingriffen am menschlichen Körper werden, insbesondere im mikrochirurgischen Bereich, häufig Instrumente zum Greifen, Halten oder zur Positionierung von Geweben oder Materialien, die mit Geweben in Kontakt kommen, verwendet. Häufig sind diese Instrumente Pinzetten, Greifer oder Klemmen. Die Verwendung dieser Instrumente kann zu einer Schädigung von Geweben oder empfindlichen Materialien führen, unter anderem durch eine zu starke Druckausübung zum Beispiel bei der Handhabung einer Pinzette. Typische Beispiele für operative Eingriffe betreffen den Bereich der Glaskörperchirurgie am Auge, wo dünne Gewebe gehandhabt werden müssen, oder auch die Positionierung von Intraokularlinsen in der Kataraktchirugie. Im Bereich der Hals-Nasen- und Ohrenheilkunde werden Silikonstreifen für die Behandlung von Trommelfellperforationen mit Klemmen gehandhabt. Für die Behandlung von Trommelfellperforationen sollten adhäsive Elemente mittels definierter Kraft aufgebracht werden, um eine optimale Adhäsion von zum Beispiel Pflastern zu ermöglichen, ohne darunterliegende Gewebe zu schädigen. Derzeit stehen keine Instrumente zur Verfügung, um diese Aufgabe so zu lösen, dass eine definierte Kraft erzielt und das Risiko einer weiteren, zu starken Kraftübertragung minimiert wird.

Es ist bisher nicht möglich die Kraft zum Aufbringen exakt zu definieren. Wenn die Pinzette zu stark gedrückt wird, findet eine Schädigung des Gewebes statt. Eine definierte Kraftaufbringung ist nicht möglich. Wird zu wenig Spannung ausgeübt führt dies zu einer unzureichenden Adhäsion, wogegen zu große Spannung zu einer Gewebeschädigung führt.

Bislang ist es mit konventionellen GreifSystemen nicht möglich, insbesondere Mikrobauteile schnell und präzise zu handhaben. Vakuumsysteme und mechanische Greifer haben eine untere Grenze von ca. 100 µm für die zu handhabende Bauteilgröße. Auch erfordern Vakuumgreifer eine hinreichende Druckdifferenz und erlauben keinen Einsatz im Vakuum.

Das Problem von kontrollierter Kontaktabfederung von Bauteilen besteht auch noch in anderen Gebieten. Zahlreiche Trümmerteile befinden sich in den Erdumlaufbahnen, die mit Satelliten, der Internationalen Raumstation und anderen Körpern kollidieren können. Um diesen Weltraummüll, der sich z.T. mit hoher Relativgeschwindigkeit bewegt, einzusammeln, müssen die Objekte abgebremst und/oder aktiv in eine niedrigere Umlaufbahn gebracht oder direkt in die Atmosphäre zurückgeführt werden, wo sie beim Wiedereintritt verbrennen. Derzeit gibt es keine technischen Lösungen für das Problem, aber eine technische

Machbarkeit des Einfangens dieser Teile mit Netzen wird diskutiert. Dazu muss das Netz annähernd die gleiche Geschwindigkeit wie das einzufangende Objekt haben. Dafür sind die gezielte Steuerung und der Aufwand von Treibstoff nötig. Daher besitzen diese derzeitigen technischen Lösungen deutliche Nachteile, die mittels der hier vorliegenden Erfindung verbessert werden.

6.1.2 Aufgabe

Der Erfindung liegt die Aufgabe zugrunde eine Struktur bereitzustellen, welche eine Kontrolle der durch die Struktur auf ein Objekt übertragenen Kraft erlaubt und insbesondere noch eine verbesserte Haftung auf einem Objekt mit rauer Oberfläche erlaubt .

6.1.3 Lösung

Diese Aufgabe wird durch die Erfindungen mit den Merkmalen der unabhängigen Ansprüche gelöst. Vorteilhafte Weiterbildungen der Erfindungen sind in den Unteransprüchen gekennzeichnet. Der Wortlaut sämtlicher Ansprüche wird hiermit durch Bezugnahme zum Inhalt dieser Beschreibung gemacht. Die Erfindungen umfassen auch alle sinnvollen und insbesondere alle erwähnten Kombinationen von unabhängigen und/oder abhängigen Ansprüchen.

Die Aufgabe wird gelöst durch eine Struktur, wobei die Struktur eine Trägerschicht umfasst, wobei auf dieser Trägerschicht eine Vielzahl von Vorsprüngen (Pillars) angeordnet sind, die mindestens jeweils einen Stamm mit einer von der Trägerschicht wegweisenden Stirnfläche umfassen, wobei auf den Stirnflächen mindestens eine weitere Schicht angeordnet sein kann, welche als Film ausgebildet ist, wobei diese Schicht als Oberfläche mindestens eine Schicht umfasst, welche einen geringeren Elastizitätsmodul aufweist als der jeweilige Vorsprung. Die Variante mit der weiteren Schicht ist eine bevorzugte Ausführungsform.

Dieser Aufbau der Struktur erlaubt es, bei Einwirken einer Kraft auf die Struktur, die Weitergabe dieser Kraft durch die Struktur zu kontrollieren, zumindest in einem bestimmten Bereich.

Wirkt eine Kraft auf die weitere Schicht, wirkt die Kraft auch durch diese Schicht hindurch auf die Vorsprünge. Im Gegensatz zu einem massiven Körper können die Vorsprünge Energie, beispielsweise durch Knickung oder Beugung, aufnehmen und auch bei Entlastung wieder in ihre ursprüngliche Form zurückkehren. Überraschenderweise wurde nun gefunden, dass bei einer solchen Struktur gerade in diesem Bereich der Energieaufnahme die durch die Struktur auf ein Objekt übertragene Kraft auf einen bestimmten Wert begrenzt ist. In diesem Bereich wird daher nur eine bestimmte maximale Kraft auf das Objekt übertragen. Es kommt zu einer Dämpfung. Die erfindungsgemäße Struktur erlaubt es daher, dass die Struktur um eine bestimmte Wegstrecke nachgeben kann, ohne dass eine erhöhte Kraft durch die Struktur übertragen wird. Erst wenn die Vorsprünge keine Energie mehr aufnehmen können, verhält sich die erfindungsgemäße Struktur analog zu einer massiven Schicht. Auf diese Weise erlaubt die Struktur die Kontaktierung mit einem deutlich höheren Toleranzbereich als eine massive Schicht.

Dies gilt auch, wenn eine Vorrichtung ohne weitere Schicht verwendet wird. Die Kraft wirkt dann direkt auf die Vorsprünge, welche die Energie entsprechend aufnehmen.

Die Größe dieser innerhalb dieses Toleranzbereichs übertragenen maximalen Kraft kann durch die verwendeten Materialien und den Aufbau der Struktur, z.B. Anzahl, Form und Aspektverhältnis der Vorsprünge, festgelegt werden. Im einfachsten Fall berechnet sich die limitierende Kraft aus der Euler-Bernoulli-Gleichung für die elastische Knickung:

$$F_{crit} = \frac{n^2 \pi^2 EI}{h^2}$$

Mit dem Elastizitätmodul E, der Höhe des Vorsprungs h, dem Flächenträgheitsmoment I, das proportional zu d^4 ist, wobei d den Durchmesser eines Vorsprungs bezeichnet, und einer numerischen Konstante n. Für eine genauere Rechnung muss dieser Ausdruck noch mit den Flächenanteil der Fillars multipliziert werden.

Die Erfindung betrifft daher eine Kontaktierungsvorrichtung umfassend die erfindungsgemäße Struktur, wobei die erfindungsgemäße Struktur zum Kontaktieren einer Oberfläche dient. Die erfindungsgemäße Struktur erlaubt es, dass beim Kontaktieren der Oberfläche eine größere Krafttoleranz möglich ist. So kann insbesondere eine Kraft bis zur maximalen Kraft, toleriert werden, welche nicht zu einer Verringerung der Adhäsionskraft führt. Dies reduziert auch die auf das kontaktierte Objekt übertragene Kraft. Dies wirkt sich auch darauf aus, mit welcher Geschwindigkeit bezogen auf die Kontaktierungsvorrichtung Objekte kontaktiert werden, so dass es zu einer Trockenadhäsion kommt.

Die Kontaktierungsvorrichtung kann auch mehrere zusammenwirkende erfindungsgemäße Strukturen aufweisen, um beispielsweise ein Objekt gleichzeitig mit mehreren erfindungsgemäßen Strukturen zu kontaktieren.

Bevorzugt handelt es sich um eine Greifvorrichtung umfassend die erfindungsgemäße Struktur. Gerade bei Greifvorrichtungen kann es leicht zu einer zu starken Belastung des Objekts kommen, insbesondere wenn die Greifvorrichtung manuell bedient werden. Die Greifvorrichtung kann beispielsweise eine Pinzette, eine Zange, eine Klemme oder ein Stempel sein.

Unter Verwendung der erfindungsgemäßen Struktur können so weniger präzise Vorrichtungen zur Handhabung von empfindlichen Objekten verwendet werden, insbesondere mit der weiteren Schicht.

Die bevorzugte Ausführungsform der erfindungsgemäßen Struktur weist abhängig von der weiteren Schicht außerdem optional eine steuerbare Adhäsion auf, sodass zusätzlich zur Dämpfung auch eine Adhäsion des Objekts an der Kontaktierungsvorrichtung erreicht werden kann. Die erfindungsgemäße Struktur verliert auch bei Verbiegen nicht ihre Adhäsion.

Die bevorzugt als Film ausgebildete weitere Schicht verbindet die verschiedenen Vorsprünge. Der Film selbst kann dabei verschiedene Schichten umfassen, wobei die äußerste Schicht, welche auf der den Vorsprüngen abgewandten Seite die Oberfläche des Films bildet, einen geringeren Elastizitätsmodul als die Vorsprünge aufweist. Diese Schicht bildet die Schicht, auf welche im Falle der Krafteinwirkung die Kraft einwirkt.

In senkrechter Richtung umfasst die bevorzugte erfindungsgemäße Struktur an der Position eines Vorsprungs daher ausgehend von der Trägerschicht mindestens zwei Bereiche mit unterschiedlichem Elastizitätsmodul, nämlich mindestens den Vorsprung und die darauf angeordnete weitere Schicht. Diese weitere Schicht und die Stirnfläche eines Vorsprungs bilden eine Grenzfläche zwischen zwei Bereichen mit unterschiedlichem Elastizitätsmodul. Abhängig von dem Herstellungsverfahren können die Grenzflächen auch dünne Schichten von Verbindungshilfsmitteln umfassen.

Innerhalb eines Bereichs ist der Elastizitätsmodul bevorzugt konstant.

Ein Vorsprung selbst kann auch noch weitere Bereiche aufweisen, welche einen unterschiedlichen Elastizitätsmodul aufweisen. In diesem Fall bezieht sich der geringere Elastizitätsmodul der weiteren Schicht immer auf den Bereich des Vorsprungs mit dem höchsten Elastizitätsmodul.

Die in einer bevorzugten Ausführungsform vorhandene weitere Schicht weist einen geringeren Elastizitätsmodul auf als der Vorsprung, auf dem sie angeordnet ist. Durch diesen Aufbau wird erreicht, dass die äußerste Schicht der Struktur besonders weich ist. Dadurch ist

die Schicht elastischer und kann sich besser auch an raue und/oder weiche Oberflächen anpassen.
Bei einer insgesamt sehr weichen Struktur kann sich diese auch sehr gut an gekrümmte Oberflächen anpassen.
Die erfindungsgemäßen Strukturen zeigen besonders gute Adhäsion an Oberflächen mit einer Rautiefe Rz von mindestens 30 µm, bevorzugt mindestens 40 µm, insbesondere in direktem Vergleich zu glatten Oberflächen mit einer Rautiefe von 0,1 µm. Die Struktur zeigt daher eine besonders gute Adhäsion an Oberflächen mit einer Rautiefe Rz von bis zu 100 µm, insbesondere bis zu 80 µm, ganz besonders bis zu 70 µm.
In einer weiteren Ausführungsform der Erfindung ist die Grenzfläche zwischen weiterer Schicht und Stirnfläche parallel zur Oberfläche der weiteren Schicht bezogen auf den jeweiligen Vorsprung .
In einer Ausführungsform der Erfindung beträgt das Verhältnis der minimalen senkrechten Dicke der weiteren Schicht oberhalb des Vorsprungs im Verhältnis zur Höhe des Vorsprungs weniger als 3, bevorzugt weniger als 1, insbesondere weniger als 0,5, insbesondere weniger als 0,3. Dadurch wirken sich die Vorsprünge unterhalb der Schicht besonders stark auf die Adhäsion aus. Das optimale Verhältnis kann auch vom Verhältnis der Elastizitätsmodule, sowie der Geometrie der Grenzfläche abhängen.
Die minimale senkrechte Dicke der weiteren Schicht kann auch von der Verwendung der Struktur abhängen.
Die vorteilhaften Parameter für Elastizitätsmodul, Größenverhältnis und Geometrie der Grenzfläche können durch Simulationen und Messungen bestimmt werden.
In einer bevorzugten Ausführungsform der Erfindung sind die Vorsprünge auf der Trägerschicht säulenartig ausgebildet. Dies bedeutet, dass es sich um bevorzugt senkrecht zur Trägerschicht ausgebildete Vorsprünge handelt, welche einen Stamm und eine Stirnfläche aufweisen, wobei der Stamm und die Stirnfläche einen beliebigen Querschnitt aufweisen können (beispielsweise kreisförmig, oval, rechteckig, quadratisch, rautenförmig, sechseckig, fünfeckig, etc.).
Bevorzugt sind die Vorsprünge so ausgebildet, dass die senkrechte Projektion der Stirnfläche auf die Grundfläche des Vorsprungs mit der Grundfläche eine Überlappungsfläche bildet, wobei die Überlappungsfläche und die Projektion der Überlappungsfläche auf die Stirnfläche einen Körper aufspannt, welcher vollständig innerhalb des Vorsprungs liegt. In einer bevorzugten Ausführungsform der Erfindung umfasst die Überlappungsfläche mindestens 50 % der Grundfläche, bevorzugt mindestens 70 % der Grundfläche, besonders bevorzugt umfasst die Überlappungsfläche die gesamte Grundfläche. Die Vorsprünge sind daher bevorzugt nicht geneigt, können es aber sein.
In einer bevorzugten Ausführungsform ist die Stirnfläche parallel zur Grundfläche und zur Oberfläche ausgerichtet. Falls die Stirnflächen nicht parallel zur Oberfläche ausgerichtet sind und daher verschiedene senkrechte Höhen aufweisen, wird als senkrechte Höhe des Vorsprungs die mittlere senkrechte Höhe der Stirnfläche angesehen.
In einer bevorzugten Ausführungsform der Erfindung weist der Stamm des Vorsprungs bezogen auf seinen mittleren Durchmesser ein Aspektverhältnis von Höhe zu Durchmesser von 1 bis 100, bevorzugt von 1 bis 10, besonders bevorzugt von 1,5 bis 5 auf.
In einer Ausführungsform liegt das Aspektverhältnis bei größer 1, bevorzugt bei mindestens 1,5, bevorzugt bei mindestens 2, bevorzugt bei 1,5 bis 15, besonders bevorzugt bei 2 bis 10.

Unter dem mittleren Durchmesser wird dabei der Durchmesser des Kreises verstanden, der die gleiche Fläche wie der entsprechende Querschnitt des Vorsprungs aufweist, gemittelt über die gesamte Höhe des Vorsprungs.
In einer weiteren Ausführungsform der Erfindung liegt das Verhältnis der Höhe eines Vorsprungs zum Durchmesser bei einer bestimmten Höhe über die gesamte Höhe des Vorsprungs immer bei 1 bis 100, bevorzugt bei 1 bis 10, besonders bevorzugt bei 1,5 bis 5. In einer Ausführungsform liegt dieses Aspektverhältnis bei mindestens 2, bevorzugt bei 2 bis 5. Dabei wird unter Durchmesser der Durchmesser des Kreises verstanden, der die gleiche Fläche wie der entsprechende Querschnitt des Vorsprungs bei der bestimmten Höhe aufweist.
Die Vorsprünge können verbreiterte Stirnflächen aufweisen, sogenannte „mushroom"-Strukturen. Es ist auch möglich, dass die weitere Schicht über die Stirnfläche hinausragt und so eine „mushroom"-Struktur bildet.
In einer bevorzugten Ausführungsform weisen die Vorsprünge keine verbreiterten Stirnflächen auf.
In einer bevorzugten Ausführungsform liegt die senkrechte Höhe aller Vorsprünge in einem Bereich von 1 µm bis 2 mm, bevorzugt 10 µm bis 1 mm, insbesondere 10 µm bis 500 µm, bevorzugt in einem Bereich von 10 µm bis 300 µm.
In einer bevorzugten Ausführungsform liegt die gesamte senkrechte Dicke der weiteren Schicht umfassend alle enthaltenen Schichten oberhalb einer Stirnfläche in einem Bereich von 1 µm bis 1 mm, bevorzugt 1 µm bis 500 µm, insbesondere 1 µm bis 300 µm, bevorzugt in einem Bereich von 1 µm bis 200 µm, insbesondere in einem Bereich von 5 µm bis 100 µm, ganz besonders 5 µm bis 60 µm.
Bevorzugt weist die weitere Schicht bezogen auf mind. 50 % der Projektion der Grundfläche eines Vorsprungs auf die Oberfläche der weiteren Schicht eine senkrechte Dicke in dem vorstehenden Bereich oder einem der bevorzugten Bereiche auf. Bevorzugt ist die Dicke auch die durchschnittliche Dicke der gesamten weiteren Schicht über die gesamte Struktur.
Die kleinste Dicke der weiteren Schicht oberhalb eines Vorsprungs ist bevorzugt immer kleiner als die maximale senkrechte Höhe des Vorsprungs.
In einer bevorzugten Ausführungsform liegt die senkrechte Dicke der Trägerschicht (Backinglayer) in einem Bereich von 1 µm bis 2 mm, bevorzugt 20 µm bis 500 µm, insbesondere 20 µm bis 150 µm. In einer bevorzugten Ausführungsform beträgt die Dicke der Trägerschicht 20 bis 60 µm.
In einer bevorzugten Ausführungsform entspricht die Grundfläche von der Fläche her einem Kreis mit einem Durchmesser zwischen 0,1 µm bis 5 mm, bevorzugt 0,1 µm und 2 mm, insbesondere bevorzugt zwischen 1 µm und 500 µm, besonders bevorzugt zwischen 1 µm und 100 µm. In einer Ausführungsform ist die Grundfläche ein Kreis mit einem Durchmesser zwischen 0,3 µm und 2 mm, bevorzugt 1 µm und 100 µm.
Der mittlere Durchmesser der Stämme liegt bevorzugt zwischen 0,1 µm bis 5 mm, bevorzugt 0,1 µm und 2 mm, insbesondere bevorzugt zwischen 10 µm und 100 µm. Bevorzugt ist die Höhe und der mittlere Durchmesser entsprechend dem bevorzugten Aspektverhältnis angepasst.
In einer bevorzugten Ausführungsform ist bei verbreiterten Stirnflächen die Oberfläche der Stirnfläche eines Vorsprungs, bzw. die Oberfläche der weiteren Schicht, mindestens 1,01 mal, bevorzugt mindestens 1,5 mal so groß wie die Fläche der Grundfläche eines Vorsprungs. Sie kann beispielsweise um den Faktor 1,01 bis 20 größer sein.

In einer weiteren Ausführungsform ist die verbreiterte Stirnfläche zwischen 5% und 100% größer als die Grundfläche, besonders bevorzugt zwischen 10% und 50% der Grundfläche.
In einer bevorzugten Ausführungsform beträgt der Abstand zwischen zwei Vorsprüngen weniger als 2 mm, insbesondere weniger als 1 mm, ganz besonders weniger als 500 µm oder weniger als 150 µm. Dabei wird der Abstand als die kürzeste Entfernung zwischen zwei Vorsprüngen verstanden.
Die Vorsprünge sind bevorzugt regelmäßig periodisch angeordnet.
In einer bevorzugten Ausführungsform der Erfindung weisen die Vorsprünge eine Höhe von 5 bis zu 500 µm, bevorzugt bis zu 400 µm auf. Die weitere Schicht weist oberhalb der Stirnflächen eine gesamte senkrechte Dicke von 3 bis 100 µm auf. Der mittlere Abstand der säulenförmigen Vorsprünge liegt zwischen 1 und 50 µm, insbesondere 5 und 50 µm. Die Dicke der Trägerschicht liegt zwischen 30 und 200 µm, insbesondere 50 und 200 µm. Der Durchmesser liegt abhängig vom Abstand der Vorsprünge bei 5 bis 100 µm. Bevorzugt sind die Vorsprünge hexagonal angeordnet.
Besonders bevorzugt liegt die Dichte der Vorsprünge bei 10000 bis 1000000 Vorsprüngen/cm^2.
Die gesamte Dicke der Struktur umfassend soweit vorhanden die weitere Schicht, die Vorsprünge und die Trägerschicht liegt bevorzugt zwischen 50 µm und 500 µm. Die Dicke der einzelnen Bestandteile wird entsprechend angepasst.
In einer Ausführungsform der Erfindung liegt die gesamte Dicke der Struktur zwischen 40 und 150 µm, insbesondere 40 und 90 µm. Bei dieser dünnen Struktur ist es bevorzugt, dass die Vorsprünge mindestens 30 % der gesamten Höhe der Struktur einnehmen, bevorzugt mindestens 40 %.
Die Elastizitätsmodule aller Bereiche des Vorsprungs und der optionalen weiteren Schichten liegen bevorzugt bei 40 kPa bis 2,5 MPa. Bevorzugt liegt der Elastizitätsmodul von weichen Bereichen, d. h. insbesondere der weiteren Schicht mit geringerem Elastizitätsmodul, bei 40 kPa bis 800 kPa, bevorzugt 50 kPa bis 500 kPa, besonders bevorzugt 50 bis 150 kPa. Bevorzugt liegt davon unabhängig der Elastizitätsmodul der Bereiche mit hohem Elastizitätsmodul, z. B. der Vorsprünge sowie z. B. der Trägerschicht, bei 1 MPa bis 2,5 MPa, bevorzugt bei 1,2 MPa bis 2 MPa. Bevorzugt liegen für alle weicheren und härteren Bereiche die Elastizitätsmodule in den vorstehend angegebenen Bereichen (gemessen mit Nanointender).
Das Verhältnis der Elastizitätsmodule zwischen dem geringsten Elastizitätsmodul und dem Bereich mit dem höchsten Elastizitätsmodul liegt bevorzugt bei unter 1:100, insbesondere bei unter 1:80, bevorzugt bei unter 1:70, davon unabhängig mindestens bei 1:2, bevorzugt mindestens 1:3.
In einer bevorzugten Ausführungsform liegt der Elastizitätsmodul der Vorsprünge und der Trägerschicht, sowie gegebenenfalls ein Bereich der weiteren Schicht, bei 1 MPa bis 2,5 MPa, bevorzugt bei 1,2 MPa bis 2 MPa, während für die Bereiche mit geringerem Elastizitätsmodul der Elastizitätsmodul bei 40 kPa bis 800 kPa, bevorzugt 50 kPa bis 500 kPa, besonders bevorzugt bei 50 bis 150 kPa liegt (gemessen mit Nanointender).
Die Verwendung eines so weichen Materials für die Vorsprünge und die Trägerschicht erlaubt die Herstellung von dickeren aber elastischeren Strukturen, welche ähnliche Adhäsionswerte aufweisen wie steifere Strukturen, während sie aber deutlich flexibler sind. Durch das Verbinden über einen Film werden die Vorsprünge zusätzlich stabilisiert. So wird verhindert, dass die weichen Vorsprünge kollabieren. Gleichzeitig sind dickere Strukturen einfacher herzustellen und leichter handhabbar.

Durch die Stabilisierung durch einen Film wird auch die Struktur selbst stabilisiert. Dies ist beispielsweise wichtig, wenn die Struktur neben der Adhäsion auch Zugkräfte parallel zur Kontaktfläche aushalten soll. Beispielweise beim Aufbringen auf zu schließende Wunden oder Verletzungen von Trommelfellen. Dies erlaubt darüber hinaus eine Verringerung des Elastizitätsmoduls der Vorsprünge und der Trägerschicht, ohne Verlust der Stabilität, insbesondere der Vorsprünge.
In einer weiteren Ausführungsform beschreiben die vorstehend angegebenen Verhältnisse das Verhältnis der Elastizitätsmodule der weiteren Schicht (weich) und der Vorsprünge (hart). Außerdem ist diese Schicht einfach sauber, bzw. steril, zu halten, da sich keinerlei Verschmutzung in den Zwischenräumen ansammeln kann. Insbesondere bei der Verwendung auf dem Trommelfell wird dadurch eine Infektionsbarriere gegen Mikroorganismen aufgebaut. Darüber hinaus führt diese „Abdichtung" auch zu einer Verbesserung der Hörleistung bei perforiertem Trommelfell.
Dadurch erscheint die Oberfläche der Struktur in dieser Ausführungsform geschlossen und einheitlich. Dadurch kann sie auch einfacher modifiziert werden, um für Anwendungen angepasst zu werden. Eine Behandlung der Oberfläche wirkt sich dann nicht auf die Strukturierung innerhalb der Beschichtung aus.
So kann die Oberfläche mit bekannten Verfahren funktionalisiert oder behandelt werden.
Die Zwischenräume zwischen den Vorsprüngen innerhalb der Struktur sind bevorzugt nicht ausgefüllt. Es ist auch möglich, dass die Zwischenräume zwischen den Vorsprüngen ausgefüllt sind, wobei das Material einen geringeren Elastizitätsmodul als die Vorsprünge und die Trägerschicht aufweist.
Die Vorsprünge können aus vielen unterschiedlichen Materialien bestehen, bevorzugt sind Elastomere, besonders bevorzugt vernetzbare Elastomere. Die Bereiche mit höherem Elastizitätsmodul können auch Duroplaste umfassen.
Die Vorsprünge sowie die weitere Schicht können daher folgende Materialien umfassen:
epoxy- und/oder silikonbasierte Elastomere, Polyurethane, Epoxidharze, Acrylatsysteme, Methacrylatsysteme, Polyacrylate als Homo- und Copolymere, Polymethacrylate als Homo- und Copolymere (PMMA, AMMA Acrylnitril/Methylmethacrylat), Polyurethan (meth) acrylate, Silikone, Silikonharze, Kautschuk, wie R-Kautschuk NR Naturkautschuk, IR Poly-Isopren-Kautschuk, BR Butadienkautschuk, SBR Styrol-Butadien-Kautschuk, CR Chloropropen-Kautschuk, NBR Nitril-Kautschuk, M-Kautschuk (EPM Ethen- Propen-Kautschuk, EPDM Ethylen-Propylen-Kautschuk), Ungesättigte Polyesterharze, Formaldehydharze, Vinylesterharze, Polyethylene als Homo- oder Copolymere, sowie Mischungen und Copolymere der vorgenannten Materialien. Bevorzugt sind auch Elastomere, welche zur Verwendung im Bereich Verpackung, Pharma und Lebensmittel von der EU (gemäß EU-VO Nr. 10/2011 vom 14.01.2011, veröffentlicht am 15.01.2011) oder EDA zugelassen sind oder silikonfreie UV-härtbare Harze aus der PVD und CVD- Verfahrenstechnik. Dabei steht Polyurethan(meth)acrylate für Polyurethanmethacrylate, Polyurethanacrylate, sowie Mischungen und/oder Copolymere davon.
Es kann sich auch um Hydrogele, beispielsweise auf Basis von Polyurethanen, Polyvinylpyrrolidon, Polyethylenoxid, Poly-2-ac- rylamido-2-methyl-l-propanesulfonsäure, Silikonen, Polyacrylamiden, hydroxylierten Polymethacrylaten oder Stärke, handeln .
Bevorzugt sind epoxy- und/oder silikonbasierte Elastomere, Polyurethan (meth) acrylate, Polyurethane, Silikone, Silikonharze (wie UV-härtbares PDMS), Polyurethan(meth)acrylate, Kautschuk (wie EPM, EPDM).

Besonders bevorzugt sind vernetzbare Silikone wie beispielsweise Polymere auf Basis Vinyl-terminierter Silikone.
Insbesondere für die weitere Schicht, welche in Kontakt mit der Oberfläche steht, sind von den vorstehend genannten die epoxy- und/oder silikonbasierte Elastomere, Polyurethan(meth)acrylate, Polyurethane, Silikone, Silikonharze (wie UV-härtbares PDMS), Polyurethan(meth)acrylate, Kautschuk (wie EPM, EPDM), insbesondere vernetzbare Silikone wie beispielweise Polymere auf Basis Vinyl-terminierter Silikone, bevorzugt.
Es können auch die vorstehend genannten Hydrogele oder druckempfindliche Klebstoffe für die weitere Schicht verwendet werden.
Bevorzugt ist die weitere Schicht eine viskoelastische Schicht.
In einer Ausführungsform der Erfindung umfasst die weitere Schicht mindestens eine Schicht mit einem höheren Elastizitätsmodul (hart), bevorzugt dem Elastizitätsmodul der Vorsprünge, sowie darauf die Schicht mit dem geringeren Elastizitätsmodul. Die untere Schicht (Stützschicht) stabilisiert die Schicht mit dem geringeren Elastizitätsmodul (Adhäsionsschicht). Dadurch können für diese Schicht besonders weiche Materialien genommen werden, ohne dass die Schicht zwischen den Vorsprüngen einsinkt .
In dieser Ausführungsform liegen die Dicke der Stützschicht zwischen 1 und 100 µm und die Dicke der Adhäsionsschicht zwischen 5 und 100 µm, bevorzugt liegen die Dicke der Stützschicht zwischen 1 und 50 µm und die Dicke der Adhäsionsschicht zwischen 10 und 50 µm, ganz besonders bevorzugt ist die Stützschicht zwischen 1 und 20 µm dick und die Adhäsionsschicht zwischen 1 und 20 µm dick.
In einer weiteren bevorzugten Ausführungsform der Erfindung weist die weitere Schicht nur einen geringeren Elastizitätsmodul auf (Adhäsionsschicht). Zwar kommt es dann zu einem gewissen Einsinken der Schicht zwischen den Vorsprüngen, aber aufgrund der hohen Elastizität der Schicht ist eine Anpassung an raue Oberflächen immer noch sehr gut möglich.
In dieser Ausführungsform liegt die Dicke der weiteren Schicht zwischen 5 und 100 µm, bevorzugt zwischen 10 und 50 µm.
In einer weiteren Ausführungsform wird die Oberfläche der weiteren Schicht behandelt. Dadurch können die Eigenschaften der Oberfläche beeinflusst werden. Dies kann durch physikalische Behandlung wie Plasmabehandlung, bevorzugt mit Ar/O_2-Plasma, geschehen .
Es können auch kovalente oder nicht kovalente Bindungen zu Additiven auf der Oberfläche ausgebildet werden, beispielsweise um eine bestimmte Kompatibilität mit den Zellen zu erreichen. Bevorzugt sind Additive zur Unterstützung der Zelladhäsion, wie z. B. Poly-L-Lysin, Poly-L-Ornithin, Collagen oder Fibronectin. Solche Additive sind aus dem Bereich der Zellkultur bekannt.
Andere Modifikationen sind die Beschichtung mit fluorierten Gruppen, wie Fluorsilanen oder das Aufbringen von Metallschichten, beispielsweise durch Bedampfung. Als Metalle kommen dabei insbesondere Edelmetalle wie, Gold, Silber und Platin, in Betracht .
Gerade bei der Anwendung im medizinischen Bereich kann es auch vorteilhaft sein, Stoffe in mindestens einen Teil der Struktur einzulagern, welche dann langsam abgegeben werden. Dies können beispielsweise Arzneimittel, wie Antibiotika sein, oder auch Hilfsstoffe zur Unterstützung der Zelladhäsion oder des Zellwachstums .
In einer weiteren Ausführungsform sind die Vorsprünge und die Trägerschicht aus dem gleichen Material.
In einer weiteren Ausführungsform der Erfindung ist die weitere Schicht mit dem geringeren Elastizitätsmodul von der Struktur ablösbar ausgeführt, bevorzugt ist die gesamte weitere Schicht der Struktur ablösbar. Ablösbar bedeutet dabei, dass insbesondere keine kovalenten

Bindungen zwischen der ablösbaren Schicht und der restlichen Struktur bestehen, beispielsweise zwischen den Vorsprüngen und der weiteren Schicht. Die Bindung basiert nur auf nichtkovalenten Bindungen.
In einer bevorzugten Ausführungsform der Erfindung umfasst die weitere Schicht ausgehend von den Stirnflächen, eine Schicht mit geringem Elastizitätsmodul zur Bindung an die Stirnflächen, eine Stützschicht, sowie die Schicht mit geringerem Elastizitätsmodul zur Adhäsion an eine Oberfläche.
Die innere Schicht mit geringerem Elastizitätsmodul dient zur Adhäsion an die Vorsprünge und ist nur durch die Adhäsionskräfte verbunden. Dadurch ist es möglich, dass der Teil der Struktur mit den Vorsprüngen abgetrennt und wiederverwendet werden kann.
Durch den Kontakt mit der Oberfläche wird die äußerste Schicht der Struktur leicht verschmutzt und kann daher nach dem Ablösen nicht wiederverwendet werden, beispielsweise bei medizinischen Anwendungen. Wenn die weitere Schicht mit dieser Schicht einfach ausgetauscht werden kann, kann der Teil der Struktur mit den Vorsprüngen einfach wiederverwendet werden, indem nur eine neue weitere Schicht aufgebracht wird. Eine beschichtete Stützschicht ist einfacher herzustellen, als der Teil der Struktur mit den Vorsprüngen.
In einer weiteren Ausführungsform der Erfindung ist die weitere Schicht ablösbar und weist ausgehend von den Vorsprüngen folgenden Aufbau auf: innere Adhäsionsschicht, Stützschicht und äußere Adhäsionsschicht. Die innere Stützschicht dient zur Stabilisierung der ablösbaren weiteren Schicht, um ein Abreißen beim Ablösen zu vermeiden. Auch ist die Schicht dann besser handhabbar. Die Adhäsionsschicht zu den Vorsprüngen hin sorgt für eine Adhäsion der weiteren Schicht an die Vorsprünge.
In dieser Ausführungsform weist die weitere Schicht eine gesamte Dicke von 50 bis 300 µm auf, bevorzugt 50 bis 150 µm.
Bevorzugt ist dabei eine Dicke der inneren Adhäsionsschicht von 5 bis 100 µm, bevorzugt 10 bis 50 µm. Davon unabhängig weist die Stützschicht eine Dicke von 5 bis 100 µm, bevorzugt von 10 bis 50 µm auf. Davon unabhängig weist die äußere Adhäsionsschicht eine Dicke von 10 bis 50 µm auf.
In einer bevorzugten Ausführungsform liegt der Elastizitätsmodul der Stützschicht bei 1 MPa bis 2,5 MPa, bevorzugt bei 1,2 MPa bis 2 MPa, während die Adhäsionsschichten einen Elastizitätsmodul von 40 kPa bis 800 kPa, bevorzugt 50 kPa bis 500 kPa, besonders bevorzugt 50 bis 150 kPa aufweisen.
Die Maße der Mikrostruktur entsprechen den vorstehenden Angaben für die anderen Ausführungsformen.
Diese Ausführungsform mit der ablösbaren weiteren Schicht erlaubt es auch, eine Mikrostruktur aus einem steiferen Material zu verwenden und ebenfalls eine verbesserte Adhäsion zu erreichen .
Bevorzugt liegt bei dieser Ausführungsform der Elastizitätsmodul der Vorsprünge und der Trägerschicht bei 1 MPa bis 4 MPa, bevorzugt 1 MPa bis 3 MPa, besonders bevorzugt bei 1 MPa bis 2,5 MPa, insbesondere bevorzugt bei 1,2 MPa bis 2 MPa.
In einer weiteren Ausführungsform umfasst die Struktur noch weitere Schichten, welche gegebenenfalls ablösbar sind. So können die Oberflächen durch ablösbare Folien vor dem Einsatz geschützt werden. Auch können weitere stabilisierende Schichten auf der Trägerschicht angeordnet sein.
Die Trägerschicht weist bevorzugt eine geringere Dicke als die maximale Höhe der auf ihr angeordneten Vorsprünge auf.

Da die Trägerschicht, wenn sie aus dem gleichen Material wie die Vorsprünge besteht, ein Material mit einem höheren Elastizitätsmodul umfasst, kann mit der Dicke der Trägerschicht auch die Elastizität der gesamten Struktur beeinflusst werden.
Die erfindungsgemäße Struktur ist bevorzugt zur Adhäsion auf weichen Substraten ausgebildet.
Die erfindungsgemäße Struktur ist insbesondere zur Adhäsion auf biologischen Geweben ausgebildet. Dazu kann sie beispielsweise als Folie ausgeführt sein. Sie kann auch in Kombination mit zu befestigenden Vorrichtungen ausgeführt sein. Dies können beispielsweise Verbandsmaterialen sein, aber auch Elektroden oder andere medizinische Vorrichtungen, wie Implantate, insbesondere Implantate, welche nicht dauerhaft an Knochen verankert werden sollen, oder weiche Implantate. Dies können beispielsweise Iri- simplantate sein. Die Erfindung betrifft daher auch ein Implantat umfassend eine erfindungsgemäße Struktur, beispielsweise auf mindestens einem Teil der Oberfläche des Implantats.
Die Erfindung betrifft außerdem die Verwendung einer vorstehend genannten Struktur zur Adhäsion auf biologischen Geweben. Dies können beliebige Gewebe sein, wie Haut, aber auch innere Gewebe, wie Organoberflächen, Oberflächen von Wunden oder Trommelfelle. Bei der Anbringung auf Haut kann dies gesundes oder geschädigtes Gewebe sein. Die Struktur kann zur Befestigung, wie zum Beispiel für Sensoren, Verbände, Pflaster, Infusionen oder ähnliches eingesetzt werden. Die Struktur kann aber auch auf geschädigtes Gewebe aufgebracht werden, wie oberflächliche Verletzungen, wie Wunden, Brandwunden, Druckstellen, chronische Wunden oder ähnliches. Die Struktur erlaubt die Kombination einer gut verträglichen Oberfläche bei gleichzeitiger Adhäsion auf dem biologischen Gewebe. Die Struktur kann so auch als Wachstumssubstrat für die Zellkultivierung oder für das neue zu bildende Gewebe dienen. Auch kann durch die innere offene Struktur der Struktur Flüssigkeit abfließen oder Luft zirkulieren .
Durch die Adhäsion der Struktur haftet die Struktur sehr gut an der Oberfläche des Trommelfells und erlaubt es sogar, unter Spannung aufgebracht zu werden, oder Spannung aufzubringen. Aufgrund ihrer Struktur haftet sie auch auf den umgebenden Geweben und nicht nur auf dem Trommelfell. Gegebenenfalls kann die derart ausgebildete Struktur unterschiedliche Bereiche mit unterschiedlicher Adhäsion umfassen. Dies kann beispielsweise über das Material, die Schichtdicke der weiteren Schicht, aber auch einfach durch die Verteilung der Vorsprünge innerhalb der Struktur erfolgen.
Durch ihre innere Strukturierung haftet die Struktur gut an dem Gewebe, auf das sie aufgebracht wird. Dies kann neben dem Trommelfell auch das umgebende Gewebe sein. Es wird kein flüssiger Bestandteil zum Aufbringen der Struktur benötigt, welcher in das Ohr hineinfließen kann.
Die Struktur kann abhängig von den verwendeten Materialien auch transparent sein, sodass ohne Ablösen der Zustand des Gewebes unterhalb der Struktur untersucht werden kann, beispielsweise um die Verheilung festzustellen.
Die Struktur kann einfach wieder abgelöst werden.
Vor dem Einsatz kann die Struktur auch physikalisch oder chemisch behandelt werden, bevorzugt zur Sterilisation. Dies kann beispielsweise eine Autokiavierung sein, beispielsweise durch Heißluftsterilisation oder Wasserdampfsterilisation bei 50 bis 200 °C, insbesondere 100 bis 150 °C, bei einem Druck von 1 bis 5 bar für 5 Minuten bis 3 Stunden. Bei einer solchen Autokla- vierung (121 °C, 2 bar, 20 Minuten) konnte keine signifikante Veränderung der Haftspannung beobachtet werden.

Weitere Verfahren zur Sterilisation sind beispielsweise Gammastrahlen oder Ethylenoxidsterilisation (ETO).
In einer weiteren Ausführungsform kann die Oberfläche beispielsweise mit Poly-L-Lysin, Poly-L-Ornithin, Collagen, Fibronectin, Gelatine, Laminine, Keratin, Tenascin oder Perlecan behandelt werden. Solche Additive sind aus dem Bereich der Zellkultur bekannt.
Die Erfindung betrifft außerdem die Verwendung der erfindungsgemäßen Struktur als Dämpfungselement.
Die Erfindung betrifft außerdem die Verwendung der erfindungsgemäßen Struktur in einer Kontaktierungsvorrichtung, insbesondere einer Greifvorrichtung.
Abhängig von der Verwendung der Greifvorrichtung und deren Ausbildung, kann auch die oberste Schicht mit einem geringeren Elastizitätsmodul mit einer weiteren dünnen Beschichtung versehen sein. Dies kann beispielsweise auch eine dünne Metallschicht, beispielsweise, Gold, Silber oder Platin sein. Diese kann beispielsweise durch Bedampfung aufgebracht werden.

Oberfläche kann aber auch durch Oberflächenmodifikation, Plasmabehandlung so angepasst werden, dass insbesondere die adhäsiven Eigenschaften reduziert werden. Oberflächenmodifikation umfasst beispielsweise Modifikation mit fluorierten Gruppen, beispielsweise Fluorsilanen.
Die erfindungsgemäße Struktur wird bevorzugt zur Kontaktierung von Objekten verwendet. Sie ist bevorzugt auf einer Oberfläche angeordnet. Sie ist daher bevorzugt Teil einer Vorrichtung.
Die Erfindung betrifft außerdem eine Vorrichtung zu dem Abbremsen von Objekten, insbesondere von Weltraumschrott umfassend eine erfindungsgemäße Struktur. Durch den Toleranzbereich der Struktur können Objekte größerer Geschwindigkeitsdifferenz auf die Struktur einwirken und ggf. in ihr haften bleiben.
Bei einer bevorzugten Ausführungsform ist die weitere Schicht bevorzugt eine viskoelastische Schicht. Dann ist es auch möglich, dass die Objekte diese Schicht durchschlagen und in der Trägerschicht stecken bleiben. Die viskoelastische Schicht schließt sich bei kleinen Objekten wieder und kann so einfach regeneriert werden. Größere Objekte bleiben an der Schicht haften .
Die Erfindung betrifft außerdem ein Verfahren zur Herstellung einer Ausführungsform der erfindungsgemäßen Struktur.
Im Folgenden werden einzelne Verfahrensschritte näher beschrieben. Die Schritte müssen nicht notwendigerweise in der angegebenen Reihenfolge durchgeführt werden, und das zu schildernde Verfahren kann auch weitere, nicht genannte Schritte aufweisen.
Dazu wird in einem ersten Schritt ein Templat zur Abformung der Vielzahl an Vorsprüngen bereitgestellt.
In dieses Templat wird das Material für die Vorsprünge eingebracht, bevorzugt als Flüssigkeit. Gegebenenfalls kann das Material auch bereits mindestens teilweise gehärtet werden.
Danach wird das Material für die Trägerschicht, d.h. die Oberfläche, auf der die Vorsprünge angeordnet sind, auf das Templat aufgebracht und gehärtet. Besonders bevorzugt ist dies das gleiche Material wie für die Stämme der Vorsprünge, so die Trägerschicht und die Stämme auch in einem Schritt hergestellt werden, beispielsweise, indem direkt eine größere Menge an Material eingebracht wird.
In einem nächsten Schritt werden die Trägerschicht und die Vorsprünge aus dem Templat gelöst.

Es kann notwendig sein, das Templat vor dem Befüllen zu inerti- sieren, beispielsweise durch Fluorsilane.
Des Weiteren kann es notwendig sein, die Vorsprünge aufzurichten, beispielsweis durch mechanische Einwirkung wie Streichen oder Bürsten.
Außerdem wird das Material für eine der weiteren Schichten auf einer Oberfläche verteilt, beispielsweise durch Spin coating. Danach wird diese Schicht gehärtet. Dies kann mehrfach mit unterschiedlichen Materialien wiederholt werden.
Zur Anbindung an die Vorsprünge wird härtbares Material auf die oberste Schicht aufgebracht und verteilt, beispielsweise durch Spin coating. Dann wird die Mikrostruktur mit den Vorsprüngen so auf diese Schicht gelegt, dass die Stirnflächen die Schicht kontaktieren. Danach wird die gesamte Struktur gehärtet. Dadurch wird die weitere Schicht fest mit den Vorsprüngen verbunden. Danach wird die Struktur von der Oberfläche gelöst.
Abhängig von Material und Struktur kann es erforderlich sein, zwischen dem Aufträgen der verschiedenen Materialien eine Plasmabehandlung durchzuführen, bevorzugt Sauerstoffplasma oder Luftplasma. Dadurch kann die Beeinflussung der unterschiedlichen Schichten bei der Härtung minimiert werden. Auch wird die Haftung verbessert.
Es kann auch erforderlich sein, die Stirnflächen der Mikrostruktur vor dem Auflegen einer Plasmabehandlung zu unterziehen. Wenn beispielsweise die Kontaktfläche der Mikrostruktur besonders klein ist.
Gerade wenn die erste Schicht, die aufgetragen wird sehr weich ist, kann es zu Problemen beim Ablösen kommen.
In einer weiteren Ausführungsform wird auf ein Releaseliner eine Schicht aus dem Material für die weitere Schicht aufgetragen und gehärtet. Bei diesem Verfahren wird daher zuerst die weitere Schicht auf einem Releaseliner aufgetragen und gegebenenfalls gehärtet. Danach werden abhängig von der Art der Struktur, welche hergestellt wird, weitere Schichten aufgetragen. Dies können weitere weiche Schichten oder auch Stützschichten sein. Die Schichten können jeweils gehärtet werden.
Danach wird die Mikrostruktur aufgebracht. Es kann erforderlich sein, dass vorher eine nicht gehärtete Schicht aufgebracht wird, welche dann erst nach dem Aufbringen der Mikrostruktur gehärtet wird.
Bei dem Releaseliner handelt es sich bevorzugt um Materialien mit einer Beschichtung aus fluorierten Silikonen oder fluorierten Silanen. Es kann sich beispielsweise um eine Folie mit einer entsprechenden Beschichtung handeln.
Der Releaseliner sollte eine möglichst glatte Oberfläche aufweisen, da jede Unebenheit auf der obersten Schicht abgeformt wird.
Weitere Einzelheiten und Merkmale ergeben sich aus der nachfolgenden Beschreibung von bevorzugten Ausführungsbeispielen in Verbindung mit den Unteransprüchen. Hierbei können die jeweiligen Merkmale für sich alleine oder zu mehreren in Kombination miteinander verwirklicht sein. Die Möglichkeiten, die Aufgabe zu lösen, sind nicht auf die Ausführungsbeispiele beschränkt. So umfassen beispielsweise Bereichsangaben stets alle - nicht genannten - Zwischenwerte und alle denkbaren Teilintervalle.
Dieses Projekt wurde im Rahmen der Fördervereinbarung Nr. 842614" ERC-2018-PoC durch das Forschungs- und Innovationsprogramm Horizon 2020 der Europäischen Union finanziert.
Die Ausführungsbeispiele sind in den Figuren dargestellt. Im Einzelnen zeigt:

Fig.	1	Aufnahme einer erfindungsgemäßen Struktur (1: Epoxidsubstrat mit Hautrauigkeit; 2: Toplayer MG1010; 3: Pillarstrukturen; 4: Backinglayer);

Fig.	2	Schematische Darstellung einer erfindungsgemäßen Struktur (links) und einer Referenzprobe mit gleicher Dicke (rechts, Referenz 1);
Fig.	3	Messung der Druckvorspannung (Preload Stress) im Verhältnis zur relativen Auslenkung; Die Ziffern bezeichnen die unterschiedlichen Phasen; Das Substrat ist EVR;
Fig.	4	Aufnahmen der erfindungsgemäßen Struktur zu den unter schiedlichen Phasen aus Figur 3;
Fig.	5	Schematische Darstellung verschiedener Proben;
Fig.	6	Messung der Druckvorspannung (Al) und Ablösespannung(A2) relativ zur Auslenkung für verschiedene Proben gegen ein raues Substrat; Vorsprünge entsprechen Figur 5c.
Fig.	7	Messung der Druckvorspannung (Bl) und Ablösespannung(B2) relativ zur Auslenkung für verschieden Proben gegen ein glattes Substrat;
Fig.	8	Schematische Darstellung der Messvorrichtung.

Fig. 1 zeigz eine Aufnahme einer erfindungsgemäßen Struktur umfassend ein Backinglayer 4, die Vorsprünge 3, auf denen ein Toplayer aus MG1010 3 angeordnet ist. Die Vorrichtung ist in Kontakt mit einem Substrat 1. Diese ist ein Epoxidsubstrat mit Hautrauigkeit.
Zur Herstellung der Struktur wurde zunächst eine Struktur mit Vorsprüngen hergestellt. Zunächst wurde eine Silikonabformung eines entsprechend geformten Wafers hergestellt. Diese weist ein Negativ für eine Struktur mit hexagonal regelmäßig angeordneten säulenförmigen Vorsprüngen mit einem Durchmesser von 60 µm und einer Höhe von 180 µm auf. Der Wafer (Siliziumwafer) wird in einer Petrischale platziert und mit dem Material für die Form der Mikrostruktur gefüllt (PDMS, Elastosil M4601 B A/B, Wacker, Riemerling, Deutschland; Verhältnis 9:1 nach Gewicht) . Nach Entgasen wird eine Glasscheibe aufgelegt und mindestens für 2 Stunden bei 75 °C gehärtet. Die gehärtete Form wird dann abgetrennt. Der Wafer weist die spätere Mikrostruktur auf.
Die hergestellte Form wurde mit Fluorsilan ((Tridecafluoro- 1,1,2,2-tetrahydrooctyl)trichlorsilan, 40 pL Lösung, 97 %) unter Vakuum (2 mbar) silanisiert.
Zur Herstellung des Films wird das Soft skin adhesive elastomer (MG7-1010 Dow Corning, USA; 1:1) auf einen Releaseliner (Si— liconature, SILFLU S 50 M 1R8802 Clear) aufgetragen und bei unterschiedlichen Geschwindigkeiten ein Spin coating durchgeführt, um unterschiedliche Dicken zu erhalten (jeweils für 120 s). Der Film wird danach für 1 Stunde bei 95 °C gehärtet. Die erhaltenen Filme hatten eine Dicke von 30 µm.
Zum Verbinden der Struktur wird ein MDX-4 Film (4000 rpm/120 s) auf eine Glasplatte aufgetragen und die vorher hergestellte Mikrostruktur mit den Stirnflächen ihrer Vorsprünge darin eingetaucht. Diese Struktur wird dann auf den MG7-1010-Film platziert und im Ofen bei 95 °C für eine Stunde gehärtet.
Figur 2 zeigt schematische Darstellungen zweier in den Versuchen verwendeter Substrate. Das erfindungsgemäße Substrat weist ein Backinglayer aus MDX4 und einer Dicke von 80 µm auf. Die Vorsprünge sind aus dem gleichen Material und haben eine Höhe von 180 µm. Darauf ist eine Schicht aus MG7-1010 mit einer Dicke von 30 µm.
Als Vergleich wurde außerdem Referenz 1 hergestellt. Bei dieser Struktur entspricht die Dicke der MDX4-Schicht der Dicke des Backing layers und der Vorsprünge. Auf dieser Schicht ist eine

MG7-1010-Schicht angeordnet, welche ebenfalls 30 µm dick ist. Beide Proben sind in Figur 2 dargestellt.
Beide Proben wurden gegen einen Intender als Substrat mit einer kreisförmigen Kontaktfläche von 7.26 mm2 vermessen, welches eine Epoxyabformung von Vitroskin mit einer mittleren Rauheit von Ra 13 µm war. Dieses Substrat wurde als EVR bezeichnet.
Figur 8 zeigt einen schematischen Aufbau der Messapparatur. In der Grafik beschreibt s die Position des Tisches in z-Richtung. Der Tisch fährt in positive z-Richtung, damit Probe und Substrat in Kontakt kommen. Sobald eine bestimmte Druckvorspannung erreicht wurde, wird die Position für eine definierte Haltezeit gehalten. Die Messgrößen, wie die induzierten Kräfte, werden mittels einer Kraftmessdose erfasst und sind von einem Bildschirm ablesbar. Die Probe wird mithilfe eines Klebesubstrats auf einem Glasobjektträger befestigt, der mit einer Schraubenvorrichtung an der Probenhalterung auf dem Tisch befestigt wird. Um die Probenposition zu variieren, kann der Tisch mitsamt der Probe auch in x- und y-Richtung verschoben werden. Die Lage und der Kontakt der Probe können mittels optischer Elemente, wie das Prisma, Kamera 1 und 2 beobachtet und justiert werden.
Der Tisch wurde in positive z-Richtung mit einer Anfahrtsgeschwindigkeit von 30 pm/s auf das Substrat zu bewegt, bis eine Druckvorspannung von 70 + 20 mN (beziehungsweise 10+4 kPa) eingestellt war. Nachdem der Kontakt von Probe zum Substrat für eine definierte Haltezeit von entweder einer oder dreißig Sekunden aufrechtgehalten wurde, wurde die Probe vom Substrat abgelöst. Dafür wurde der Tisch mit einer Abzugsgeschwindigkeit von 10 pm/s in negative z-Richtung gefahren. Der Messaufbau beinhaltet eine Kraftmessdose (max. 3N, Tedea-Huntleigh 1004, Vishay Precision Group, Basingstoke,GB), die auf das Erfassen niedriger Ablösekräfte ausgerichtet ist. Vom System wurden die induzierten Normalkräfte F in z-Richtung relativ zur Zeit t und zur Position des Tisches sz aufgezeichnet. In die Probenhalterung wurde zur optischen Erfassung der Probenposition und damit der Kontakt zwischen Probe und Substrat beobachtet werden konnte, ein Prisma integriert. Dieses ermöglichte es mithilfe zweier Kameras (Kamera 1 und 2) (DMK23UX236, The Imaging Source, Deutschland) die Messungen an einem Computerbildschirm zu verfolgen und aufzuzeichnen. Zur Justage der Kontaktfläche zwischen Probe und Testsubstrat wurde ein Goniometer verwendet.
Die Probe und das Substrat wurden mit einer Geschwindigkeit von 30 pm/1 aufeinander zubewegt, bis zu einer bestimmten maximalen Kraft, entsprechend eine bestimmten Druckvorspannung.
Figur 3 zeigt in verschiedenen Messungen, welche Druckvorspannung jeweils gemessen wurde, wenn der Intender jeweils um 10 pm weiter auf die Probe eindringt (relative Auslenkung). Jeder Punkt ist eine einzelne Messung. Jede Probe wurde an drei verschiedenen Positionen vermessen (Die Fehlerbalken entsprechen der Standardabweichung).
Figur 4 zeigt Aufnahmen der erfindungsgemäßen Struktur innerhalb der jeweiligen Kreise in der Figur 3. In Bereich 1 (Figur 4 Abbildung 1) ist die Probe und das Substrat in Kontakt. Aufgrund des viskoelastischen Films passt sich die Kontaktfläche an die Rauheit des Intenders an. In Bereich 2 (Figur 4 Abbildungen 2a und 2b) führt die zunehmende Kompression zu einer Beugung und Knickung der Vorsprünge innerhalb der Struktur. Dadurch steigt die gemessene Druckvorspannung nicht weiter an. Dies ist ein krafttoleranter Bereich, d.h. bei zunehmendem Druck bleibt die gemessene Druckvorspannung konstant. In Bereich 3 (Figur 4 Abbildung 3) sind die Vorsprünge völlig gebeugt und der krafttolerante Bereich endet. In Bereich 4 (Figur 4, Abbildung 4) steigt die Druckvorspannung ähnlich der Referenzstruktur (Referenz 1) an. Die gepresste Struktur verhält sich wie ein unstrukturierter Festkörper.

Figur 5 zeigt eine schematische Darstellung von weiteren Strukturen. Die oberen beiden Proben entsprechend den Strukturen aus Figur 2. Als dritte Struktur wird eine Struktur mit Vorsprüngen ohne aufgebrachten Film verwendet. Das Material ist MDX4.
Als Substrat wurde wieder EVR verwendet. Als zweites Substrat wurde eine Abformung mit einer Rauheit ähnlich von Glas (Ra 0,01 µm) und einer Fläche von 6,1 mm^2 verwendet.
Die Strukturen wurden mit 30 pm/s aufeinander zubewegt bis eine bestimmte maximale Kraft entsprechend einer bestimmten Druckvorspannung erreicht wurde (Figur 6 Al für EVR und Figur 7Bl für das Glassubstrat). Jeder der Punkte zeigt das Ergebnis einer Messung. Die Auslenkung wurde für jede Messung um 10 µm erhöht.
Für die Adhäsionsmessung (Figur 6, A2 und Figur 7 B2) wurde die Probe nach 1 Sekunde Haltezeit mit einer Geschwindigkeit von 10 µm/s bis zur vollständigen Ablösung vom Substrat wegbewegt. Die Ablösekraft wurde gemessen und in eine maximale Ablösespannung in Relation zur Kontaktfläche umgerechnet. Jede Probe wurde an drei verschiedenen Positionen vermessen (Die Fehlerbalken entsprechen der Standardabweichung). Die Probe „Vorsprünge" ist das System der Erfindung ohne terminale Schicht.
Aus den Messungen ist gut zu erkennen, dass die erfindungsgemäßen Proben einen krafttoleranten Bereich aufweisen. In diesem Bereich nimmt der Druck auf das Substrat bei zunehmender Auslenkung nicht mehr zu. Gleichzeitig ist zu erkennen, dass die gemessene Adhäsion auch in diesem Bereich relativ konstant ist. Die Eulerknickung führt daher im Gegensatz zu den Vorsprüngen nicht dazu, dass die Adhäsion abnimmt oder nur sehr schlecht ist. Dies vergrößert den krafttoleranten Bereich.
Die kritische Belastung (P_b) , bei welcher sich Vorsprünge beginnen zu knicken, lässt sich durch die Euler-Bernoulli-Gleichung für säulenförmigen Vorsprünge abschätzen:

$$P_b = n * a\pi^2 EI\ /h^2$$

Dabei steht E für den Elastizitätsmodul, $I = \pi r^4/4$ ist das zweite Trägheitsmoment eines säulenförmigen Vorsprungs mit Radius r, h ist die Höhe eines Vorsprungs und α ist eine Konstante und kann für Vorsprünge mit zwei befestigten Enden mit dem Wert 1 angenommen werden (α entspricht der Konstante n^2 der vorherigen Formel). Für die Probe in Figur 3 mit ca. 582 Vorsprüngen in 7,26 mm^2 und einem Elastizitätsmodul von MDX4 von 1,9 MPa, I mit 6,26 x 10~7 mm^4 und eine Höhe von 180 µm ergibt sich ein P_b von 214,2 mN, was einer Druckvorspannung von 28,41 kPa entspricht. Dies korrespondiert sehr gut mit dem Beginn des krafttoleranten Bereichs von 28,415 kPa, der experimentell bestimmt wurde. Die Ausführungsform mit der weiteren Schicht ermöglicht es somit, eine Kraft jenseits der limitierenden Kraft der Euler-Bernoulli-Gleichung ohne Verlust der Adhäsion zu tolerieren .
Filmterminierte Systeme weisen gegenüber reinen Vorsprüngen eine verbesserte Adhäsion, insbesondere auf rauen Oberflächen auf. Beim Ablösen können die Vorsprünge einen Teil der Energie aufnehmen. Beim Ablösen zeigt sich, dass die Referenzprobe eine lineare Zunahme der Ablösespannung, abhängig von der Auslenkung aufweist. Für erfindungsgemäße Probe zeigt dagegen einen sehr steilen Anstieg in Abhängigkeit von der relativen Auslenkung. Im krafttoleranten Bereich bis zu einer relativen Auslenkung von ca. 100 µm, nimmt die Ablösespannung in Abhängigkeit von der angewandten Kompression stark zu. Selbst im Bereich jenseits des krafttoleranten Bereichs, nimmt die Ablösespannung, wenn auch schwächer, zu.
Für die Probe mit reinen Vorsprüngen zeigt sich, dass die angewandte Kompression zu einer starken Abnahme der Adhäsion führt. Allerdings ist ebenfalls ein krafttoleranter Bereich in Bezug auf die Vorspannung messbar.

Wie in den Figuren 6 und 7 gezeigt, ist die Referenzprobe auf dem glatten Substrat etwas besser.
Die Ergebnisse zeigen, dass bei Belastung einer erfindungsgemäßen Probe über den reinen Kontakt hinaus, die auf das Substrat wirkende Belastung in einem Bereich konstant bleibt. Durch die Stabilisierung durch den Film, mit dem die Vorsprünge bevorzugt fest verbunden sind, bleibt die Struktur bei Belastung stabilisiert und kollabiert nicht. Durch die Wahl des Materials des Films und der Vorsprünge und des Backing layers, sowie dem Aspektverhältnis der Vorsprünge, können die Eigenschaften der Struktur beeinflusst werden. Bei Kompression können die Vorsprünge durch Beugung Energie speichern. Zusammen mit einem viskoelastischem Film wird eine sehr gute Adhäsion an rauen Substraten erzielt. Beim Ablösen wird die gespeicherte Energie im Gegensatz zu Referenzproben vorteilhaft freigesetzt, sodass die Haftung der Struktur verbessert wird. Dies deutet auf einen synergetischen Effekt aus einem Zusammenwirken von Vorsprüngen und Film hin. Die Vorsprünge führen zu einem dämpfenden Effekt, welcher dazu führt, dass bei zunehmender einwirkender Kraft, die auf das Substrat wirkende Kraft konstant bleibt. Allerdings weist die Struktur mit Film einen größere Krafttoleranz auf.
Alle Proben konnten mehrfach belastet werden, ohne dass es zu einer Ablösung des Films kam.

6.2 Patentansprüche

1. Struktur umfassend eine Trägerschicht, wobei auf dieser Trägerschicht eine Vielzahl von Vorsprüngen angeordnet ist, die mindestens jeweils einen Stamm mit einer von der Oberfläche wegweisenden Stirnfläche umfassen.
2. Struktur nach Anspruch 1, dadurch gekennzeichnet, dass auf der Stirnfläche mindestens eine weitere Schicht angeordnet ist, welche als Film ausgebildet ist, wobei diese Schicht als Oberfläche mindestens eine Schicht umfasst, welche einen geringeren Elastizitätsmodul aufweist als der jeweilige Vorsprung.
3. Struktur nach Anspruch 1 oder 2, dadurch gekennzeichnet, dass die Vorsprünge ein Aspektverhältnis von größer 1 aufweisen .
4. Struktur nach einem der Ansprüche 1 bis 3, dadurch gekennzeichnet, dass der Elastizitätsmodul der Vorsprünge sowie der Trägerschicht bei 1 MPa bis 2,5 MPa liegt und der Elastizitätsmodul der Schicht mit geringerem Elastizitätsmodul bei 40 kPa bis 800 kPa liegt.
5. Kontaktierungsvorrichtung umfassend eine Struktur nach einem der Ansprüche 1 bis 4.
6. Kontaktierungsvorrichtung nach Anspruch 5, dadurch gekennzeichnet, dass die Kontaktierungsvorrichtung mehrere zusammenwirkende Strukturen nach einem der Ansprüche 1 bis 4 aufweist.
7. Kontaktierungsvorrichtung nach einem der Ansprüche 5 oder 6, dadurch gekennzeichnet, dass die Kontaktierungsvorrichtung eine Greifvorrichtung ist.
8. Verwendung der Struktur nach einem der Ansprüche 1 bis 4 als Dämpfungselement.
9. Vorrichtung zum Abbremsen von Objekten umfassend eine Struktur nach einem der Ansprüche 1 bis 4.

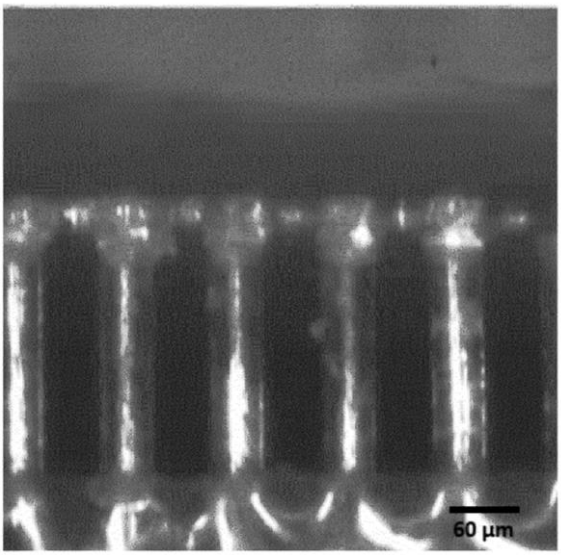

Figure 6.1: Aufnahme einer erfindungsgemäßen Struktur (1: Epoxidsubstrat mit Hautrauigkeit; 2: Toplayer MG1010; 3: Pillarstrukturen; 4: Backinglayer)

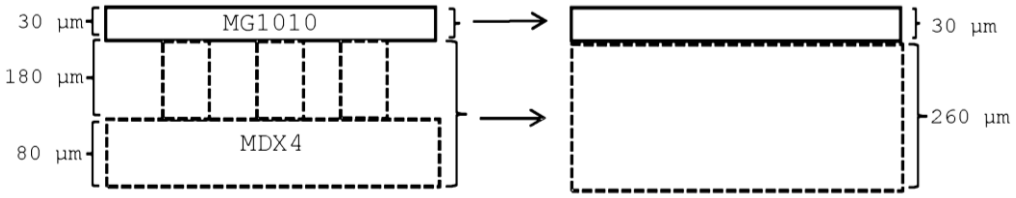

Figure 6.2: Schematische Darstellung einer erfindungsgemäßen Struktur (links) und einer Referenzprobe mit gleicher Dicke (rechts, Referenz 1)

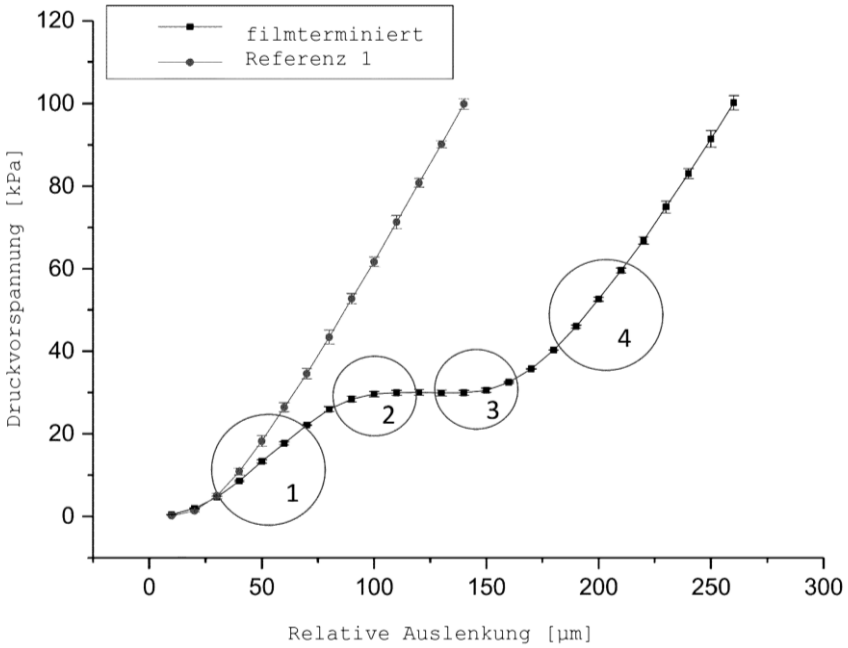

Figure 6.3: Messung der Druckvorspannung (Preload Stress) im Verhältnis zur relativen Auslenkung; Die Ziffern bezeichnen die unterschiedlichen Phasen; Das Substrat ist EVR

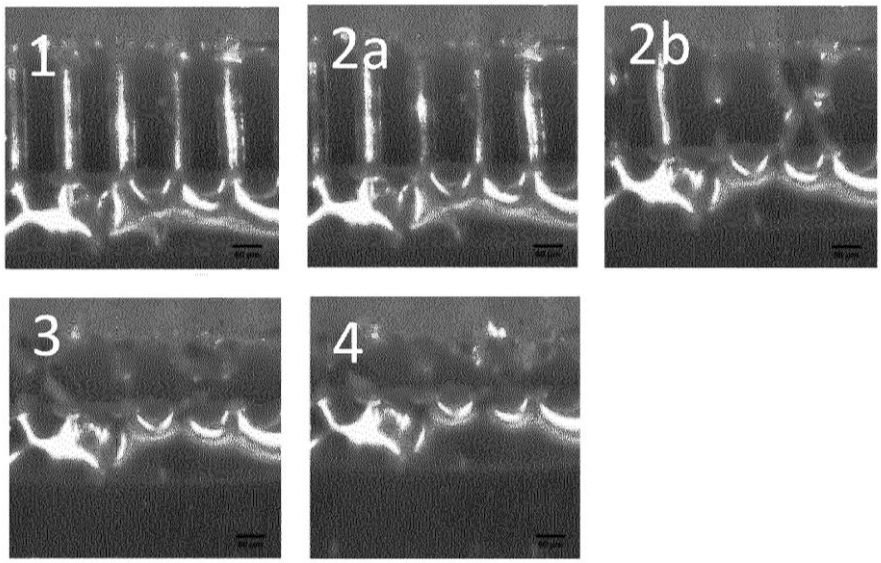

Figure 6.4: Aufnahmen der erfindungsgemäßen Struktur zu den unter schiedlichen Phasen aus Figur 3

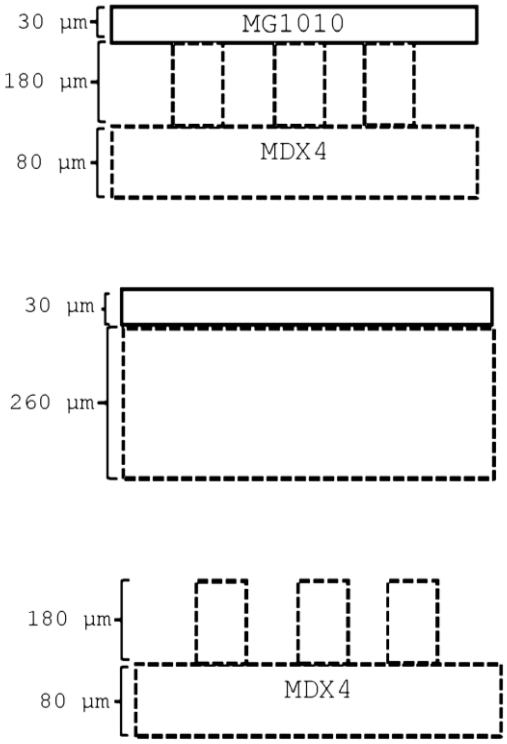

Figure 6.5: Schematische Darstellung verschiedener Proben

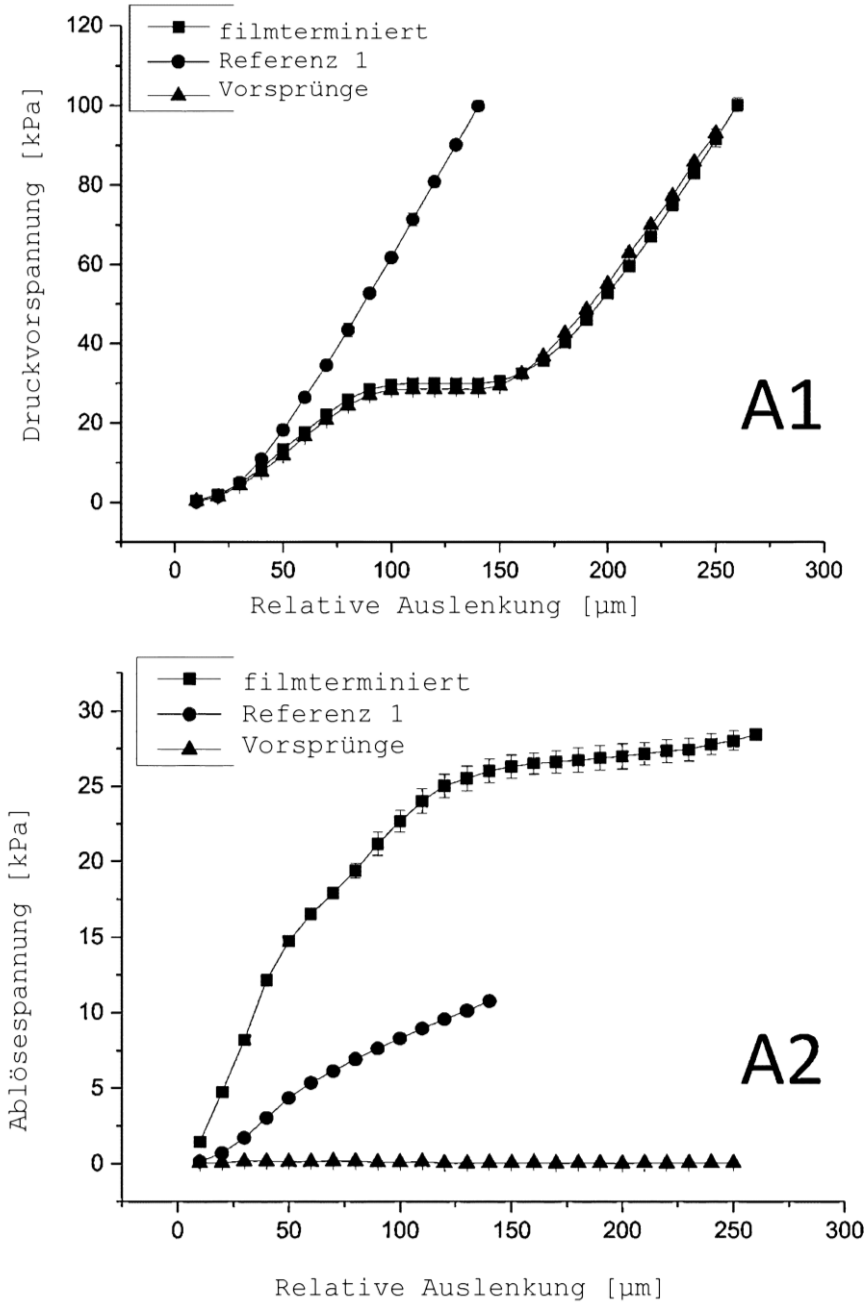

Figure 6.6: Messung der Druckvorspannung (Al) und Ablösespannung(A2) relativ zur Auslenkung für verschiedene Proben gegen ein raues Substrat; Vorsprünge entsprechen Figur 5c.

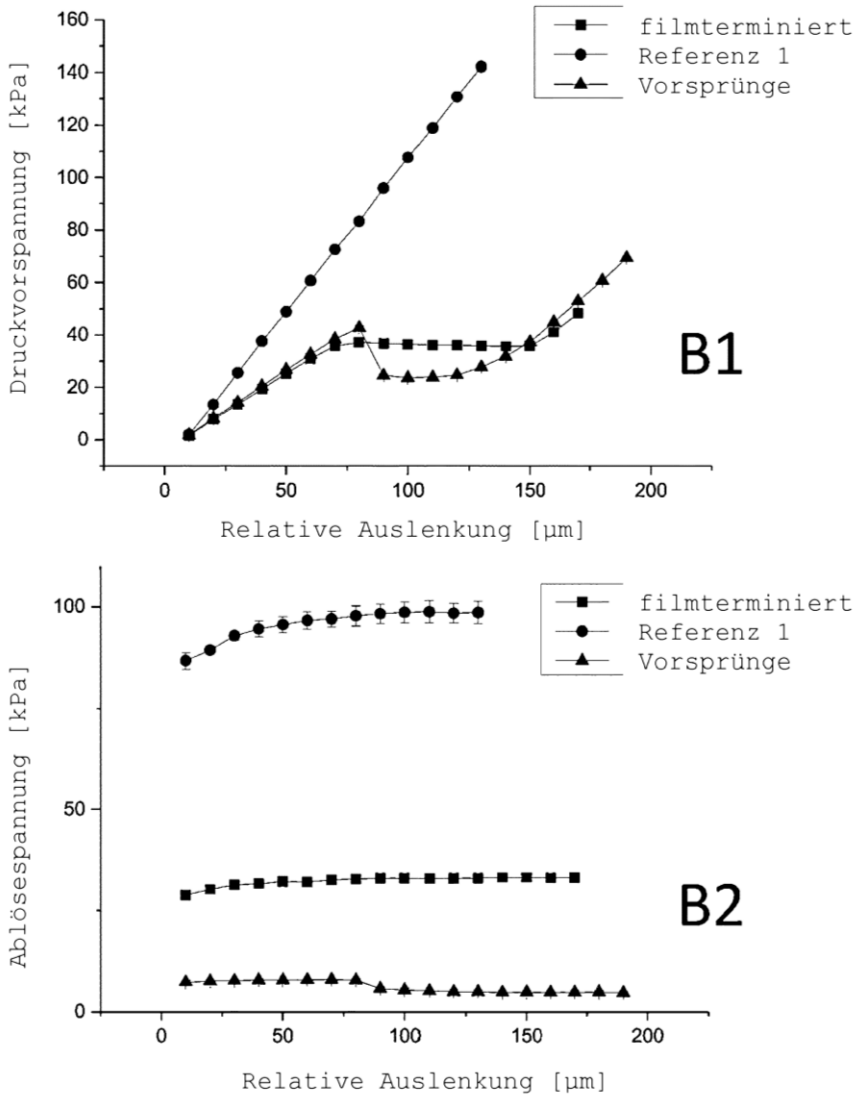

Figure 6.7: Messung der Druckvorspannung (Bl) und Ablösespannung(B2) relativ zur Auslenkung für verschieden Proben gegen ein glattes Substrat

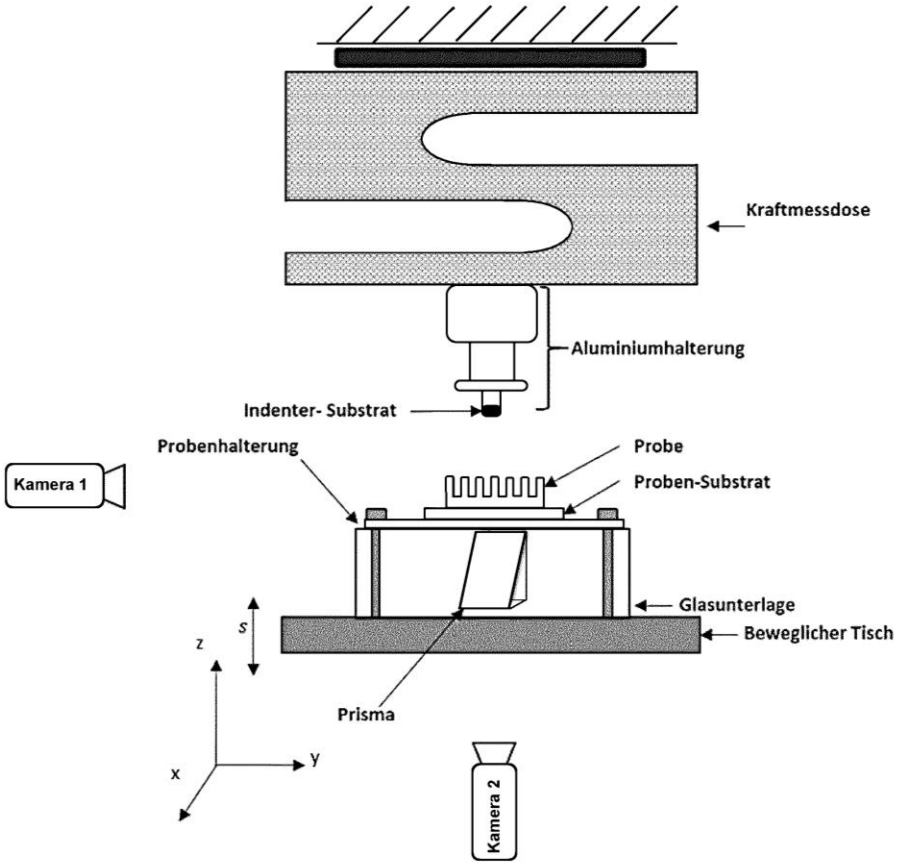

Figure 6.8: Schematische Darstellung der Messvorrichtung

Chapter 7. Discussion and outlook

Adhesives are highly demanded in biomedicine: for skin applications, reliable attachment without damaging the skin is of utmost importance, while for treating eardrum perforations, a less invasive alternative for the surgical approach will improve patients' quality of life, accelerate treatment time and reduce costs. Those demands were addressed in this work by proposing the use of a bioinspired microstructured adhesive, the film-terminated fibrillar system. This design has interesting features to overcome challenging characteristics of biological surfaces, such as roughness.

In **Chapter 4,** we report the adhesion of the film-terminated microstructure against different rough surfaces. First, against a glass-smooth surface, the influence of the compressive preload was analyzed, and a "tolerance range" of compression was observed. The force plateau observed in the measurements is linked to the buckling instability of the fibrils. Instead of going through a detachment mechanism, as commonly used for the simple fibrils, the sample with a terminating layer can be further compressed without transferring energy to the countersurface, like a "**cushioning effect**", and, most importantly, without losing adhesion performance. This effect was identified as an interesting feature for the application of the microstructure in biomedical products, as it protects the countersurface against damage.

Then, evaluating adhesion to randomly distributed roughness, the microstructure presented improved adhesion to surfaces of skin-like roughness (R_z = 50 μm) compared to unstructured control samples. The improved **tolerance to roughness** was attributed to better conformity of the microstructure to the surface topography and the graded character of the system due to the soft terminal layer.

We also investigated adhesion on model sinusoidal surfaces with features near the roll-off wavelengths for the measured "skin-like" surface. This surface feature, determined by power spectrum density analysis (PSD), defines the range in which elastic energy to contact the countersurfaces is relevant. Based on that, we proposed a **theoretical model** to show that the subsurface microstructure reduces the influence of the stiffer background, making the structure altogether more compliant.

The **lateral threshold** for a good adhesion on the sinusoidal surfaces was determined empirically as $\lambda > 4D$, being λ the wavelength of the countersurface and D the diameter of the fibrils. If the geometrical condition is fulfilled, adhesion can be tuned by increasing the contact area through compressive preload.

The influence of the **terminal layer thickness** was also investigated; experimental results showed that the thinner terminal layer yields lower pull-off stress compared to the thicker terminal layer. With FE simulations of contact formation, it was found that thinner layers present higher local stress concentrations, which explains the comparatively earlier detachments.

The systematic investigation of the film-terminated fibrillar structure on different surfaces is a valuable contribution to adhesion science and mechanics research. Considering roughness as one of the main challenging features in biological surfaces, the proposed film-terminated design shows promising results. Nonetheless, further work to understand the adhesion to the skin is necessary, especially considering the further hindering parameter such as viscoelasticity of the countersurface or presence of humidity.

Regarding the second biomedical application, the treatment of **eardrum perforations**, a further step has been taken toward clinical applications and product development and the outcome is reported in **Chapter 5**.

Miniaturized film-terminated samples were fabricated for animal testing. The adhesion was first investigated in a model surface of R_z = 2.5 μm, roughness comparable to that of the mouse TMs of 1.18 μm. The latter was determined by imprinting negative replicas of explanted eardrums. The **adhesion to the rigid surfaces** showed advantageous performance of the microstructure in comparison to unstructured control samples, similar to the work presented in Chapter 4.

The **explanted eardrums** were used to evaluate the adhesion of the patches using a custom-made setup. Here, since other effects take part, such as the softness, the concave shape of the membrane, and the less pronounced roughness, the adhesion was not statistically

significantly different between microstructures and control samples. We expect, however, that the positive effect of the microstructure on adhesion to the rougher eardrums in humans will be beneficial.

Then, we measured **hearing properties** *in vivo* of mice with TMs in different conditions: intact, perforated and perforated with an adhesive patch on. Using DPOAE signals, we were able to verify an **immediate improvement** in hearing function after applying the patch and closing the perforation. The simple closure of the perforation through the continuous terminal layer has another practical advantage, as it avoids entrance of pathogens to the middle ear. Moreover, the microstructured patch shows better handling, reported by our experienced ENT surgeon. Also, the effect of damping extra preload by fibril buckling, as mentioned in Chapter 4, protects the membrane against further damage.

Further work towards clinical application has been done for the "eardrum patch" project, such as *in vitro* experiments to verify cell growth on the adhesive's surface and the investigation of the healed membrane after 9 and 14 days. These reports are in preparation and were not included in this work. The lab-scale experiments, *in vitro* and *in vivo* tests, are crucial steps for developing biomedical products. Thanks to the successful collaboration with the ENT Clinic of the Saarland University, an essential part of this path was achieved and is presented in this thesis. This project is quite advanced on the path to a medical product; **clinical tests** are foreseen after concluding the biological tests mentioned above, and adapting the patch size for a human eardrum.

Finally, we reported in **Chapter 6** the patent claim of the "**force tolerance**" effect observed by applying a compressive load to the film-terminated microstructure. As discussed in Chapter 4 and Chapter 5, this is an essential feature of the system to **protect the countersurface** against damage while applying the adhesive, but also unravels novel applications, for instance, the collection of space debris.

Chapter 8. Conclusions

In this work, bioinspired microstructured adhesives were explored to meet urgent needs in biomedicine. The film-terminated fibrillar design is a powerful tool to overcome the challenges of sticking to complex surfaces such as the human body, as indicated if Figure 8.1. The most important conclusions of this work are listed:

- Unlike flat unstructured samples, the film-terminated structure has improved tolerance to **roughness** typical of skin. Specific parameters for optimal performance were investigated, such as terminal layer thickness and relationship to the countersurface specifications. A theoretical model was presented to convey the mechanical behavior of the microstructure.
- Under compressive load, the subsurface fibrils undergo mechanical instability without loss in adhesion. The "**force-tolerance**" effect protects the countersurface against damage during application and reveals a novel functionality for medical patches to be applied on sensitive or injured surfaces.
- The application of the microstructured adhesive as an alternative **treatment for eardrum perforations** showed promising results *ex vivo* and *in vivo*. The film-terminated samples ensure wound closure, attach to the mouse eardrum, have easy handling for the surgeon, and provide immediate improvement of hearing properties after application.

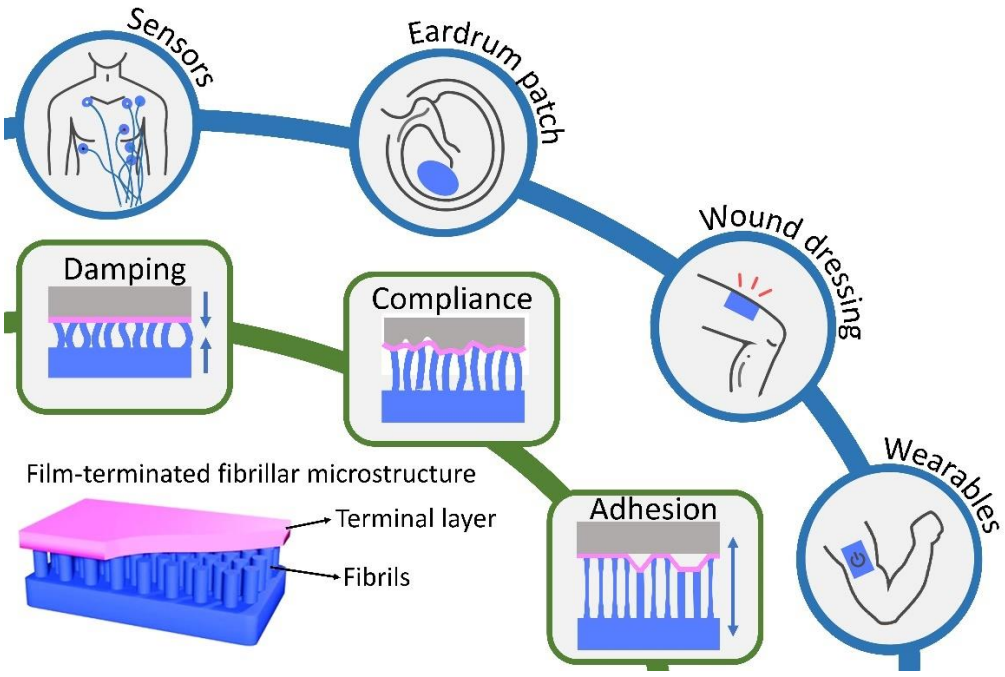

Figure 8.1: Graphical summary of the present work. Film-terminated microstructured adhesives were investigated regarding damping, compliance to roughness and adhesion, showing promissing performance for medical applications.

There are still many challenges to be tackled in developing medical devices for skin, such as viscoelasticity and the presence of water. Not to mention, many possibilities to expand the functionality of the proposed microstructure are available, for instance, the integration of electronic devices for wearables. Concerning the application for eardrum perforations, clinical tests are in sight. The product is expected to change the paradigm of delicate wound care, replacing current cost-intensive practices with modern treatments using smart materials for better patient care.

Chapter 9. List of Publications

Peer-reviewed publications used as chapters

- Moreira Lana, G.; Zhang, X.; Müller, C.; Hensel, R.; Arzt, E. Film-terminated fibrillar microstructures with improved adhesion on skin-like surfaces. ACS Appl. Mater. Interfaces 2022. https://pubs.acs.org/doi/10.1021/acsami.2c12663
- Moreira Lana, G., Sorg, K., Wenzel, G.I., Hecker, D., Hensel, R., Schick, B., Kruttwig, K. and Arzt, E. (2021), Self-Adhesive Silicone Microstructures for the Treatment of Tympanic Membrane Perforations. Adv. NanoBiomed Res., 1: 2100057. https://doi.org/10.1002/anbr.202100057

Other peer-reviewed publications

- Katharina Sorg, Larissa Heimann, Gabriela Moreira Lana, Achim Langenbucher, Bernhard Schick, Eduard Arzt, Gentiana Ioana Wenzel, "Optoacoustically induced auditory brainstem responses in the mouse model enhanced through an absorbing film," J. Biomed. Opt. 26(9) 098001 (3 September 2021) https://doi.org/10.1117/1.JBO.26.9.098001

Presentations

- Moreira Lana, Gabriela. Bioinspired adhesives for medical applications. Workshop "Designed Materials and Microstructures" – 5-7 October 2022. UCSB Santa Barbara, Ca, USA
- Moreira Lana, G., Sorg, K., Wenzel, G.I., Hensel, R., Schick, B., Arzt, E. Functional microstructured adhesives - on the path to clinical applications. Oral presentation. ESMED General Assembly (European Society of Medicine), 4-6 August 2022, Virtual
- Moreira Lana, G. The role of fibrils in film-terminated microstructured adhering to skin-like rough surfaces. Structural Materials Seminar, 25 February 2022, UCSB, Santa Barbara, Ca, USA
- Moreira Lana, G. The role of fibrils in film-terminated microstructured adhering to skin-like rough surfaces. Oral presentation. The Adhesion Society 45th Annual Meeting, February 22, 2022, San Diego, Ca, USA
- Moreira Lana, G., Sorg, K., Wenzel, G.I., Hecker, D., Hensel, R., Schick, B., Kruttwig, K. and Arzt, E. Self-Adhesive Silicone Microstructures for the Treatment of Tympanic Membrane Perforations. Poster. Virtual Adhesion Science Gathering 2021. September 22-24, 2021. Virtual
- Moreira Lana, G. Enhanced adhesion properties of film-terminated microstructures on different roughness substrates. Oral presentation. The Adhesion Society 44th Annual Meeting, February 23, 2021, Virtual

- Sorg, Katharina; Heimann, Larissa; Moreira Lana, Gabriela; Stahn, Patricia; Engel, Jutta; Arzt, Eduard; Langenbucher, Achim; Schick, Bernhard; Wenzel, Gentiana. Increase of optoacoustic-induced auditory brainstem response amplitudes using an absorbing patch. In: European Conferences on Biomedical Optics, SPIE; 2021
- Sorg, Katharina; Heimann, Larissa; Lana, Gabriela Moreira; Stahn, Patricia; Engel, Jutta; Arzt, Eduard; Langenbucher, Achim; Schick, Bernhard; Wenzel, Gentiana. Increase of optoacoustic-induced auditory brainstem response amplitudes using an absorbing patch. In: European Conferences on Biomedical Optics 2021 (ECBO), June 6, 2021, Munich . Optical Society of America; 2021: ETu5B.2.

Patent applications

- K. Kruttwig, G. Moreira Lana, K. Moh, E. Arzt. ‘‘Krafttolerante Mikrostruktur’’, DE10 2021 103 895.2. Priority Date 18.01.2021

List of Figures

Chapter 10. References

1. Landsburg, S. E. *The Armchair Economist (revised and updated May 2012): Economics & Everyday Life*. (Simon and Schuster, 2007).

2. Kendall, K. *Molecular adhesion and its applications. The Sticky Universe*. (2001).

3. Pocius, A. V & Dillard, D. *Adhesion Science and Engineering - Surfaces, Chemistry and applications*. (Elsevier, 2002).

4. Arzt, E., Quan, H., McMeeking, R. M. & Hensel, R. Functional surface microstructures inspired by nature – from adhesion and wetting principles to sustainable new devices. *Prog. Mater. Sci.* (2021).

5. Hensel, R., Moh, K. & Arzt, E. Engineering Micropatterned Dry Adhesives: From Contact Theory to Handling Applications. *Adv. Funct. Mater.* **28**, (2018).

6. *Gecomer für die Medizin Markt- und Anwendungsfeldanalyse*. (2020).

7. Hwang, I. *et al.* Multifunctional Smart Skin Adhesive Patches for Advanced Health Care. *Adv. Healthc. Mater.* **7**, 1–20 (2018).

8. Karp, J. M. & Langer, R. Dry solution to a sticky problem. *Nature* **477**, 42–43 (2011).

9. Lee, C., Choi, C. H. & Kim, C. J. Superhydrophobic drag reduction in laminar flows: a critical review. *Exp. Fluids* **57**, 1–20 (2016).

10. Brian, D. & Bhushan, B. Shark-skin surfaces for fluid-drag reduction in turbulent flow: a review. *Phil. Trans. R. Soc. A.* **368**, 4775–4806 (2010).

11. Barthlott, W. & Neinhuis, C. Purity of the sacred lotus, or escape from contamination in biological surfaces. *Planta* 1–8 (1997).

12. Sullivan, T. N., Meyers, M. A. & Arzt, E. Scaling of bird wings and feathers for efficient flight. 1–9 (2019).

13. Zahouani, H. *et al.* Characterization of the mechanical properties of a dermal equivalent compared with human skin in vivo by indentation and static friction tests. *Ski. Res. Technol.* **15**, 68–76 (2009).

14. Nachtigall, W. *Biological mechanisms of attachment - The comparative morphology and bioengineering of organs, linkage, suction and adhesion*. (Springer, 1974).

15. Autumn, K. *et al.* Adhesive force of a single gecko foot-hair. *Lett. to Nat.* **405**, (2000).

16. Higham, T. E., Russell, A. P., Niewiarowski, P. H., Wright, A. & Speck, T. The Ecomechanics of Gecko Adhesion: Natural Surface Topography, Evolution, and Biomimetics. *Integr. Comp. Biol.* **59**, 148–167 (2019).

17. Arzt, E., Gorb, S. & Spolenak, R. From micro to nano contacts in biological attachment devices. *Proc. Natl. Acad. Sci. U. S. A.* **100**, 10603–10606 (2003).

18. Persson, B. N. J. On the mechanism of adhesion in biological systems. *J. Chem. Phys.* **118**, 7614–7621 (2003).

19. Northen, M. T., Greiner, C., Arzt, E. & Turner, K. L. A gecko-inspired reversible adhesive. *Adv. Mater.* **20**, 3905–3909 (2008).

20. Hertz H. Journal für die reine und angewandte mathematik. **91**, (1981).

21. Johnson, K. L., Kendall, K. & A. D. Roberts. Surface energy and the contact of elastic solids. *Proc. R. Soc. London. A. Math. Phys. Sci.* **324**, 301–313 (1971).

22. Yao, H. & Gao, H. Mechanics of robust and releasable adhesion in biology: Bottom-up designed hierarchical structures of gecko. *J. Mech. Phys. Solids* **54**, 1120–1146 (2006).

23. Chung, J. Y. & Chaudhury, M. K. Roles of discontinuities in bio-inspired adhesive pads. *J. R. Soc. Interface* **2**, 55–61 (2005).

24. Aksak, B., Hui, C. Y. & Sitti, M. The effect of aspect ratio on adhesion and stiffness for soft elastic fibres. *J. R. Soc. Interface* **8**, 1166–1175 (2011).

25. Tinnemann, V., Arzt, E. & Hensel, R. Switchable double-sided micropatterned adhesives for selective fixation and detachment. *J. Mech. Phys. Solids* **123**, 20–27 (2019).

26. Shahsavan, H. & Zhao, B. Conformal adhesion enhancement on biomimetic microstructured surfaces. *Langmuir* **27**, 7732–7742 (2011).

27. Del Campo, A., Greiner, C., Álvarez, I. & Arzt, E. Patterned surfaces with pillars with controlled 3D tip geometry mimicking bioattachment devices. *Adv. Mater.* **19**, 1973–1977 (2007).

28. Fischer, S. C. L. *et al.* Bioinspired polydimethylsiloxane-based composites with high shear resistance against wet tissue. *J. Mech. Behav. Biomed. Mater.* **61**, 87–95 (2016).

29. Buhl, S., Greiner, C., Del Campo, A. & Arzt, E. Humidity influence on the adhesion of biomimetic fibrillar surfaces. *Int. J. Mater. Res.* **100**, 1119–1126 (2009).

30. Cadirov, N., Booth, J. A., Turner, K. L. & Israelachvili, J. N. Influence of Humidity on Grip and Release Adhesion Mechanisms for Gecko-Inspired Microfibrillar Surfaces. *ACS Appl. Mater. Interfaces* **9**, 14497–14505 (2017).

31. Kim, S., Sitti, M., Hui, C. Y., Long, R. & Jagota, A. Effect of backing layer thickness on adhesion of single-level elastomer fiber arrays. *Appl. Phys. Lett.* **91**, 89–92 (2007).

32. Greiner, C. & Arzt, E. Adhesion of Bioinspired Micropatterned Surfaces : Effects of Pillar Radius , Aspect Ratio , and Preload. **1**, 3495–3502 (2007).

33. Gorb, S. N. & Filippov, A. E. Fibrillar adhesion with no clusterisation: Functional

significance of material gradient along adhesive setae of insects. *Beilstein J. Nanotechnol.* **5**, 837–845 (2014).

34. Fischer, S. C. L., Arzt, E. & Hensel, R. Composite Pillars with a Tunable Interface for Adhesion to Rough Substrates. *ACS Appl. Mater. Interfaces* **9**, 1036–1044 (2017).

35. Heepe, L. & Gorb, S. N. Biologically inspired mushroom-shaped adhesive microstructures. *Annu. Rev. Mater. Res.* **44**, 173–203 (2014).

36. Zhang, X., Wang, Y., Hensel, R. & Arzt, E. A design strategy for mushroom-shaped microfibrils with optimized dry adhesion: Experiments and finite element analyses. *J. Appl. Mech. Trans. ASME* **88**, 1–9 (2021).

37. Fischer, S. C. L. *et al.* Funnel-Shaped Microstructures for Strong Reversible Adhesion. *Adv. Mater. Interfaces* **4**, (2017).

38. Wang, Y., Kang, V., Arzt, E., Federle, W. & Hensel, R. Strong Wet and Dry Adhesion by Cupped Microstructures. *ACS Appl. Mater. Interfaces* **11**, 26483–26490 (2019).

39. Wang, Y., Kang, V., Federle, W., Arzt, E. & Hensel, R. Switchable Underwater Adhesion by Deformable Cupped Microstructures. *Adv. Mater. Interfaces* **7**, (2020).

40. Wang, Y., Zhang, X., Hensel, R. & Arzt, E. Sliding Mechanism for Release of Superlight Objects from Micropatterned Adhesives. *Adv. Mater. Interfaces* **9**, (2022).

41. Bae, W. G., Kim, D. & Suh, K. Y. Instantly switchable adhesion of bridged fibrillar adhesive via gecko-inspired detachment mechanism and its application to a transportation system. *Nanoscale* **5**, 11876–11884 (2013).

42. Glassmaker, N. J., Jagota, A., Hui, C.-Y., Noderer, W. L. & Chaudhury, M. K. Biologically inspired crack trapping for enhanced adhesion. *Proc. Natl. Acad. Sci.* **104**, 10786–10791 (2007).

43. B.N.J., P. Contact mechanics for randomly rough surfaces. *Surf. Sci. Rep.* **61**, 29 (2006).

44. Persson, B. N. J. & Tosatti, E. The effect of surface roughness on the adhesion of elastic solids. *J. Chem. Phys.* **115**, 5597–5610 (2001).

45. Pastewka, L. & Robbins, M. O. Contact between rough surfaces and a criterion for macroscopic adhesion. *Proc. Natl. Acad. Sci. U. S. A.* **111**, 3298–3303 (2014).

46. Glassmaker, N. J., Jagota, A., Hui, C. Y. & Kim, J. Design of biomimetic fibrillar interfaces: 1. Making contact. *J. R. Soc. Interface* **1**, 23–33 (2004).

47. Yao, H. & Gao, H. Gibson-soil-like materials achieve flaw-tolerant adhesion. *J. Comput. Theor. Nanosci.* **7**, 1299–1305 (2010).

48. Gorumlu, S. & Aksak, B. Sticking to rough surfaces using functionally graded bio-inspired microfibres. *R. Soc. Open Sci.* **4**, (2017).

49. Autumn, K., Majidi, C., Groff, R. E., Dittmore, A. & Fearing, R. Effective elastic modulus of isolated gecko setal arrays. *J. Exp. Biol.* **209**, 3558–3568 (2006).

50. Creton, C. Pressure-sensitive adhesives: An introductory course. *MRS Bull.* **28**, 434–439 (2003).

51. Creton, C. Chapter 14 - Tack. in *Adhesion Science and Engineering* 535–576 (2002). doi:10.1016/b978-1-4832-3309-3.50008-6.

52. Liu, J., Hui, C. Y., Jagota, A. & Shen, L. A model for static friction in a film-terminated microfibril array. *J. Appl. Phys.* **106**, (2009).

53. Shen, L., Jagota, A. & Hui, C. Y. Mechanism of sliding friction on a film-terminated fibrillar interface. *Langmuir* **25**, 2772–2780 (2009).

54. Vajpayee, S., Long, R., Shen, L., Jagota, A. & Hui, C. Y. Effect of rate on adhesion and static friction of a film-terminated fibrillar interface. *Langmuir* **25**, 2765–2771 (2009).

55. Nadermann, N., Ning, J., Jagota, A. & Hui, C.-Y. Active Switching of Adhesion in a Film-Terminated Fibrillar Structure. *Langmuir* **26**, 15464–15471 (2010).

56. Jagota, A. & Hui, C. Y. Adhesion, friction, and compliance of bio-mimetic and bio-inspired structured interfaces. *Mater. Sci. Eng. R Reports* **72**, 253–292 (2011).

57. He, Z., Moyle, N. M., Hui, C. Y., Levrard, B. & Jagota, A. Adhesion and Friction Enhancement of Film-Terminated Structures against Rough Surfaces. *Tribol. Lett.* **65**, 1–8 (2017).

58. Shahsavan, H. & Zhao, B. Biologically inspired enhancement of pressure-sensitive adhesives using a thin film-terminated fibrillar interface. *Soft Matter* **8**, 8281–8284 (2012).

59. Shahsavan, H. & Zhao, B. Bioinspired functionally graded adhesive materials: Synergetic interplay of top viscous-elastic layers with base micropillars. *Macromolecules* **47**, 353–364 (2014).

60. Creton, C. & Ciccotti, M. Fracture and adhesion of soft materials: A review. *Reports Prog. Phys.* **79**, (2016).

61. Boyadzhieva, S. Bachelorarbeit: Einfluss von Proteinadsorption, Substratrauheit, Filmdicke und Haltezeit auf die Adhäsion des Silikonelastomers SSA MG 7-9800. (2017).

62. Fischer Lidwina, C. S. New Designs for Bioinspired Microstructures with Adhesion to Rough Surfaces Dissertation. *Doktors der Ingenieurwissenschaften der* (2017).

63. Fischer, S. C. L., Kruttwig, K., Bandmann, V., Hensel, R. & Arzt, E. Adhesion and Cellular Compatibility of Silicone-Based Skin Adhesives. *Macromol. Mater. Eng.* **302**, 1–11 (2017).

64. Abusomwan, U. & Sitti, M. Effect of retraction speed on adhesion of elastomer fibrillar

structures. *Appl. Phys. Lett.* **101**, (2012).

65. Zosel, A. Adhesion and tack of polymers: Influence of mechanical properties and surface tensions. *Colloid Polym. Sci.* **263**, 541–553 (1985).

66. Thiemecke, J. & Hensel, R. Contact Aging Enhances Adhesion of Micropatterned Silicone Adhesives to Glass Substrates. *Adv. Funct. Mater.* **2005826**, 1–11 (2020).

67. Castellanos, G., Arzt, E. & Kamperman, M. Effect of viscoelasticity on adhesion of bioinspired micropatterned epoxy surfaces. *Langmuir* **27**, 7752–7759 (2011).

68. Chen, S. *et al.* Adhesive Tissue Engineered Scaffolds: Mechanisms and Applications. *Front. Bioeng. Biotechnol.* **9**, (2021).

69. Zhu, B., Gong, S. & Cheng, W. Softening gold for elastronics. *Chem. Soc. Rev.* **48**, 1668–1711 (2019).

70. Stadlober, B., Zirkl, M. & Irimia-Vladu, M. Route towards sustainable smart sensors: Ferroelectric polyvinylidene fluoride-based materials and their integration in flexible electronics. *Chem. Soc. Rev.* **48**, 1787–1825 (2019).

71. Kim, D. W. *et al.* Highly Permeable Skin Patch with Conductive Hierarchical Architectures Inspired by Amphibians and Octopi for Omnidirectionally Enhanced Wet Adhesion. *Adv. Funct. Mater.* **29**, 1–9 (2019).

72. Kamyshny, A. & Magdassi, S. Conductive nanomaterials for 2D and 3D printed flexible electronics. *Chem. Soc. Rev.* **48**, 1712–1740 (2019).

73. Jayathilaka, W. A. D. M. *et al.* Significance of Nanomaterials in Wearables: A Review on Wearable Actuators and Sensors. *Adv. Mater.* **31**, 1–21 (2019).

74. Guk, K. *et al.* Evolution of wearable devices with real-time disease monitoring for personalized healthcare. *Nanomaterials* **9**, 1–23 (2019).

75. Stauffer, F. *et al.* Skin Conformal Polymer Electrodes for Clinical ECG and EEG Recordings. *Adv. Healthc. Mater.* **7**, 1–10 (2018).

76. Maiti, R. *et al.* In vivo measurement of skin surface strain and sub-surface layer deformation induced by natural tissue stretching. *J. Mech. Behav. Biomed. Mater.* **62**, 556–569 (2016).

77. Trojahn, C., Schario, M., Dobos, G., Blume-Peytavi, U. & Kottner, J. Reliability and validity of two in vivo measurements for skin surface topography in aged adults. *Ski. Res. Technol.* **21**, 54–60 (2015).

78. Meyers, M. A., Chen, P. Y., Lin, A. Y. M. & Seki, Y. Biological materials: Structure and mechanical properties. *Prog. Mater. Sci.* **53**, 1–206 (2008).

79. Proksch, E., Brandner, J. M. & Jensen, J. M. The skin: An indispensable barrier. *Exp. Dermatol.* **17**, 1063–1072 (2008).

80. Madison, K. C. Barrier function of the skin: 'La Raison d'Être' of the epidermis. *J. Invest. Dermatol.* **121**, 231–241 (2003).

81. Honari, S. Topical therapies and antimicrobials in the management of burn wounds. *Crit. Care Nurs. Clin. North Am.* **16**, 1–11 (2004).

82. Pan, W., Matsuda, B. & Yuk, H. Biocompatible hydrogel ostomy adhesive. *Med. Devices Sensors* **3**, 1–10 (2020).

83. Hansen, D. Skin adhesives for ostomy care applications: Water diffusion in polymer composites & itseffect on adhesion. vol. 26 (2020).

84. Guan, Z., Baker, K. & Sandberg, W. S. Misalignment of disposable pulse oximeter probes results in false saturation readings that influence anesthetic management. *Anesth. Analg.* **109**, 1530–1533 (2009).

85. Haahr, R. G. *et al.* An electronic patch for wearable health monitoring by reflectance pulse oximetry. *IEEE Trans. Biomed. Circuits Syst.* **6**, 45–53 (2012).

86. Tian, L. *et al.* Large-area MRI-compatible epidermal electronic interfaces for prosthetic control and cognitive monitoring. *Nat. Biomed. Eng.* **3**, 194–205 (2019).

87. Duck, G. P., Seung, C. S., Sung, W. K. & Youn, T. K. Development of flexible self adhesive patch for professional heat stress monitoring service. in *Annual International Conference of the IEEE Engineering in Medicine and Biology - Proceedings* vol. 7 VOLS 3789–3792 (Conf Proc IEEE Eng Med Biol Soc, 2005).

88. Huttunen, O. H., Behfar, M. H., Hiitola-Keinänen, J. & Hiltunen, J. Electronic Tattoo with Transferable Printed Electrodes and Interconnects for Wireless Electrophysiology Monitoring. *Adv. Mater. Technol.* **2101496**, (2022).

89. Meziane, N. *et al.* Simultaneous comparison of 1 gel with 4 dry electrode types for electrocardiography. *Physiol. Meas.* **36**, 513–529 (2015).

90. Lee, Y., Kim, J., Koo, J. H., Kim, T. H. & Kim, D. H. Nanomaterials for bioelectronics and integrated medical systems. *Korean J. Chem. Eng.* **35**, 1–11 (2018).

91. Kim, J., Campbell, A. S. & Wang, J. Wearable non-invasive epidermal glucose sensors: A review. *Talanta* **177**, 163–170 (2018).

92. Song, E., Li, J. & Rogers, J. A. Barrier materials for flexible bioelectronic implants with chronic stability - Current approaches and future directions. *APL Mater.* **7**, (2019).

93. Laulicht, B., Langer, R. & Karp, J. M. Quick-release medical tape. *Proc. Natl. Acad. Sci. U. S. A.* **109**, 18803–18808 (2012).

94. Chung, H. U. *et al.* Binodal, wireless epidermal electronic systems with in-sensor analytics for neonatal intensive care. *Science (80-.).* **363**, 6430 (2019).

95. Kwak, M. K., Jeong, H. E. & Suh, K. Y. Rational design and enhanced biocompatibility of

a dry adhesive medical skin patch. *Adv. Mater.* **23**, 3949–3953 (2011).

96. Fuller, K. N. G.; Tabor, D. The effect of surface roughness on the adhesion of elastic solids. *Proc. R. Soc. London. A. Math. Phys. Sci.* **345**, 327–342 (1975).

97. Gujrati, A. *et al.* Comprehensive topography characterization of polycrystalline diamond coatings. *Surf. Topogr. Metrol. Prop.* **9**, (2021).

98. Heldt, E. Oberflächeparameter. *Zeiss* 1 (2016).

99. Martínez, J. F. G., Nieto-Carvajal, I., Abad, J. & Colchero, J. Nanoscale measurement of the power spectral density of surface roughness: How to solve a difficult experimental challenge. *Nanoscale Res. Lett.* **7**, 1–33 (2012).

100. Gadelmawla, E. S., Koura, M. M., Maksoud, T. M. A., Elewa, I. M. & Soliman, H. H. Roughness parameters. *J. Mater. Process. Technol.* **123**, 133–145 (2002).

101. Kumar, R. K., Seetharamu, S. & Kamaraj, M. Quantitative evaluation of 3D surface roughness parameters during cavitation exposure of 16Cr-5Ni hydro turbine steel. *Wear* **320**, 16–24 (2014).

102. Persson, B. N. J., Albohr, O., Tartaglino, U., Volokitin, A. I. & Tosatti, E. On the nature of surface roughness with application to contact mechanics, sealing, rubber friction and adhesion. *Journal of Physics Condensed Matter* vol. 17 (2005).

103. Jacobs, T. D. B., Junge, T. & Pastewka, L. Quantitative characterization of surface topography using spectral analysis. *Surf. Topogr. Metrol. Prop.* **5**, (2017).

104. Gong, Y., Misture, S. T., Gao, P. & Mellott, N. P. Surface roughness measurements using power spectrum density analysis with enhanced spatial correlation length. *J. Phys. Chem. C* **120**, 22358–22364 (2016).

105. Joe, J., Thouless, M. D. & Barber, J. R. Effect of roughness on the adhesive tractions between contacting bodies. *J. Mech. Phys. Solids* **118**, 365–373 (2018).

106. Wang, A. & Müser, M. H. Is there more than one stickiness criterion? *Friction* 4–7 (2022) doi:10.1007/s40544-022-0644-3.

107. Kovalev, A. E., Dening, K., Persson, B. N. J. & Gorb, S. N. Surface topography and contact mechanics of dry and wet human skin. *Beilstein J. Nanotechnol.* **5**, 1341–1348 (2014).

108. Kottner, J. *et al.* Comparison of two in vivo measurements for skin surface topography. *Ski. Res. Technol.* **19**, 84–90 (2013).

109. Bloemen, M. C. T., Van Gerven, M. S., Van Der Wal, M. B. A., Verhaegen, P. D. H. M. & Middelkoop, E. An objective device for measuring surface roughness of skin and scars. *J. Am. Acad. Dermatol.* **64**, 706–715 (2011).

110. Barreau, V. *et al.* Fibrillar Elastomeric Micropatterns Create Tunable Adhesion Even to Rough Surfaces. *Adv. Funct. Mater.* **26**, 4687–4694 (2016).

111. Tang, W. *et al.* Tactile Perception of Skin and Skin Cream. *Tribol. Lett.* **59**, 1–13 (2015).

112. Fischer, S. C. L., Boyadzhieva, S., Hensel, R., Kruttwig, K. & Arzt, E. Adhesion and relaxation of a soft elastomer on surfaces with skin like roughness. *J. Mech. Behav. Biomed. Mater.* **80**, 303–310 (2018).

113. Cho, K. S. Theory of linear viscoelasticity. in *Viscoelasticity of polymers* vol. 241 285–359 (Springer Series in Materials Science, 2016).

114. Cho, K. S. Theory of linear viscoelasticity. in *Viscoelasticity of polymers* vol. 241 285–359 (Springer, 2016).

115. Lamers, E., van Kempen, T. H. S., Baaijens, F. P. T., Peters, G. W. M. & Oomens, C. W. J. Large amplitude oscillatory shear properties of human skin. *J. Mech. Behav. Biomed. Mater.* **28**, 462–470 (2013).

116. Silver, F. H., Freeman, J. W. & Devore, D. Viscoelastic properties of human skin and processed dermis. *Ski. Res. Technol.* **7**, 18–23 (2001).

117. Ní Annaidh, A., Bruyère, K., Destrade, M., Gilchrist, M. D. & Otténio, M. Characterization of the anisotropic mechanical properties of excised human skin. *J. Mech. Behav. Biomed. Mater.* **5**, 139–148 (2012).

118. Holt, B., Tripathi, A. & Morgan, J. Viscoelastic response of human skin to low magnitude physiologically relevant shear. *J. Biomech.* **41**, 2689–2695 (2008).

119. Geerligs, M. *et al.* In vitro indentation to determine the mechanical properties of epidermis. *J. Biomech.* **44**, 1176–1181 (2011).

120. Sugihara, T., Ohura, T., Homma, K. & Igawa, H. H. The extensibility in human skin: variation according to age and site. *Br. J. Plast. Surg.* **44**, 418–422 (1991).

121. Pailler-Mattei, C., Bec, S. & Zahouani, H. In vivo measurements of the elastic mechanical properties of human skin by indentation tests. *Med. Eng. Phys.* **30**, 599–606 (2008).

122. Luebberding, S., Krueger, N. & Kerscher, M. Mechanical properties of human skin in vivo: A comparative evaluation in 300 men and women. *Ski. Res. Technol.* **20**, 127–135 (2014).

123. Agache, P. G., Monneur, C., Leveque, J. L. & De Rigal, J. Original Contributions Mechanical Properties and Young's Modulus of Human Skin in Vivo. *Arch Dermatol Res* **269**, 221–232 (1980).

124. Jacquemoud, C., Bruyere-Garnier, K. & Coret, M. Methodology to determine failure characteristics of planar soft tissues using a dynamic tensile test. *J. Biomech.* **40**, 468–475 (2007).

125. Delalleau, A., Josse, G., Lagarde, J. M., Zahouani, H. & Bergheau, J. M. Characterization of the mechanical properties of skin by inverse analysis combined with an

extensometry test. *Wear* **264**, 405–410 (2008).

126. Cheung, E. & Sitti, M. Adhesion of biologically inspired polymer microfibers on soft surfaces. *Langmuir* **25**, 6613–6616 (2009).

127. Huber, G. *et al.* Evidence for capillarity contributions to gecko adhesion from single spatula nanomechanical measurements. *Proc. Natl. Acad. Sci. U. S. A.* **102**, 16293–16296 (2005).

128. Wang, Y. *et al.* Water as a 'glue': Elasticity-enhanced wet attachment of biomimetic microcup structures. *Sci. Adv.* **8**, 1–8 (2022).

129. De Souza, E. J. *et al.* In vitro adhesion measurements between skin and micropatterned poly(dimethylsiloxane) surfaces. *Proc. 31st Annu. Int. Conf. IEEE Eng. Med. Biol. Soc. Eng. Futur. Biomed. EMBC 2009* **0049**, 6018–6021 (2009).

130. Kaiser, J. S., Kamperman, M., de Souza, E. J., Schick, B. & Arzt, E. Adhesion of biocompatible and biodegradable micropatterned surfaces. *Int. J. Artif. Organs* **34**, 180–184 (2011).

131. Mahdavi, A. *et al.* A biodegradable and biocompatible gecko-inspired tissue adhesive. *Proc. Natl. Acad. Sci. U. S. A.* **105**, 2307–2312 (2008).

132. Lee, H., Lee, B. P. & Messersmith, P. B. A reversible wet / dry adhesive inspired by mussels and geckos. *Nature* **448**, (2007).

133. Baik, S. *et al.* A wet-tolerant adhesive patch inspired by protuberances in suction cups of octopi. *Nature* **546**, 396–400 (2017).

134. Anand, S., Danti, S., Moroni, L. & Mota, C. Regenerative therapies for tympanic membrane. *Prog. Mater. Sci.* **127**, 100942 (2022).

135. Gaihede, M., Liao, D. & Gregersen, H. In vivo areal modulus of elasticity estimation of the human tympanic membrane system: Modelling of middle ear mechanical function in normal young and aged ears. *Phys. Med. Biol.* **52**, 803–814 (2007).

136. Kuypers, L. C., Decraemer, W. F. & Dirckx, J. J. J. Thickness distribution of fresh and preserved human eardrums measured with confocal microscopy. *Otol. Neurotol.* **27**, 256–264 (2006).

137. Sagiv, D., Chin, O. Y., Diaz, R. C. & Brodie, H. A. State of the art regeneration of the tympanic membrane. *Curr. Opin. Otolaryngol. Head Neck Surg.* **28**, 314–322 (2020).

138. Gladstone, H. B., JAckler, R. K. & Varav, K. Tympanic membrane wound healing - An overview. *Otolaryngol. Clin. north Am.* **28**, (1995).

139. Voss, S. E., Rosowski, J. J., Merchant, S. N. & Peake, W. T. How do tympanic-membrane perforations affect human middle-ear sound transmission? *Acta Otolaryngol.* **121**, 169–173 (2001).

140. Griffin, W. L. A retrospective atudy of traumatic tympanic membrane perforations in a clinical practice. *Laryngoscope* **89**, (1979).

141. Broughton, G., Janis, J. E. & Attinger, C. E. Wound healing: An overview. *Plast. Reconstr. Surg.* **117**, 1–32 (2006).

142. Kim, S. W. *et al.* Latent progenitor cells as potential regulators for tympanic membrane regeneration. *Sci. Rep.* **5**, 1–8 (2015).

143. McMinn, R. M. H. & Taylor, M. The cytology of repair in experimental perforations of the tympanic membrane. *Br. J. Surg.* **53**, 222–232 (1966).

144. Hong, P., Bance, M. & Gratzer, P. F. Repair of tympanic membrane perforation using novel adjuvant therapies: A contemporary review of experimental and tissue engineering studies. *Int. J. Pediatr. Otorhinolaryngol.* **77**, 3–12 (2013).

145. Nordvik, O. *et al.* Generic quality of life in persons with hearing loss: A systematic literature review. *BMC Ear, Nose Throat Disord.* **18**, 1–13 (2018).

146. Sorg, K. Biocompatibility studies for novel therapeutic strategies at the tympanic membrane level. (Universität des Saarlandes, 2022).

147. Ghanad, I. *et al.* A Systematic Review of Nonautologous Graft Materials Used in Human Tympanoplasty. *Laryngoscope* (2020) doi:10.1002/lary.28914.

148. Özdamar, K. & Sen, A. Comparison of the anatomical and functional success of fascia and perichondrium grafts in transcanal endoscopic type 1 tympanoplasty. *J. Otolaryngol. - Head Neck Surg.* **48**, 1–7 (2019).

149. PALVA, T. & RAMSAY, H. Myringoplasty and tympanoplasty—results related to training and experience. *Clin. Otolaryngol. Allied Sci.* **20**, 329–335 (1995).

150. Hardman, J., Muzaffar, J., Nankivell, P. & Coulson, C. Tympanoplasty for Chronic Tympanic Membrane Perforation in Children. *Otol. Neurotol.* **36**, 796–804 (2015).

151. Kuo, C. Y. *et al.* Repair of Tympanic Membrane Perforations with Customized Bioprinted Ear Grafts Using Chinchilla Models. *Tissue Eng. - Part A* **24**, 527–535 (2018).

152. Fina, M., Bresnick, S., Bairp, A. & Ryan, A. Improved healing of tympanic membrane perforations with basic fibroblast growth factor. *Growth Factors* **5**, 265–272 (1991).

153. Omae, K. *et al.* Regenerative treatment for tympanic membrane perforation using gelatin sponge with basic fibroblast growth factor. *Auris Nasus Larynx* **44**, 664–671 (2017).

154. Khademhosseini, A. & Langer, R. A decade of progress in tissue engineering. *Nat. Protoc.* **11**, 1775–1781 (2016).

155. Farhadi, M. *et al.* Collagen-immobilized patch for repairing small tympanic membrane perforations : In vitro and in vivo assays. 549–553 (2011) doi:10.1002/jbm.a.33293.

156. Xu, S., Yu, J., Hu, Y., Yang, B. & Yang, N. The effectiveness and safety of growth factors in the treatment of tympanic membrane perforations: a systematic review and meta-analysis of randomized controlled trials. *Eur. Arch. Oto-Rhino-Laryngology* **279**, 1863–1874 (2022).

157. Kozin, E. D. *et al.* Design, fabrication, and in vitro testing of novel three-dimensionally printed tympanic membrane grafts. *Hear. Res.* **340**, (2016).

158. Anand, S. *et al.* Mimicking the Human Tympanic Membrane: The Significance of Scaffold Geometry. *Adv. Healthc. Mater.* **10**, 1–16 (2021).

159. Moscato, S. *et al.* Tympanic membrane collagen expression by dynamically cultured human mesenchymal stromal cell/star-branched poly(ε-Caprolactone) nonwoven constructs. *Appl. Sci.* **10**, (2020).

160. Lee, H., Jang, C. H. & Kim, G. H. A polycaprolactone/silk-fibroin nanofibrous composite combined with human umbilical cord serum for subacute tympanic membrane perforation; An in vitro and in vivo study. *J. Mater. Chem. B* **2**, 2703–2713 (2014).

161. Seonwoo, H. *et al.* Epidermal Growth Factor–Releasing Radially Aligned Electrospun Nanofibrous Patches for the Regeneration of Chronic Tympanic Membrane Perforations. *Adv. Healthc. Mater.* **8**, 1–11 (2019).

162. Immich, A. P. S. *et al.* Improved tympanic membrane regeneration after myringoplastic surgery using an artificial biograft. *Mater. Sci. Eng. C* **73**, 48–58 (2017).

163. Li, L. *et al.* Preparation of gelatin/genipin nanofibrous membrane for tympanic member repair. *J. Biomater. Sci. Polym. Ed.* **29**, 2154–2167 (2018).

164. von Witzleben, M. *et al.* Biomimetic Tympanic Membrane Replacement Made by Melt Electrowriting. *Adv. Healthc. Mater.* **10**, 1–18 (2021).

165. Kaur, K., Singh, H. & Singh, M. Repair of tympanic membrane perforation by topical application of 1 % sodium hyaluronate. **58**, 241–244 (2006).

166. Grotenhuis, N. *et al.* Implementation of the hyaluronic acid fat graft myringoplasty technique , pitfalls and lessons learned. **6489**, (2017).

167. Guruswamy Damodaran, R. & Vermette, P. Tissue and organ decellularization in regenerative medicine. *Biotechnol. Prog.* **34**, 1494–1505 (2018).

168. Boyadzhieva, S. *et al.* A Self-Adhesive Elastomeric Wound Scaffold for Sensitive Adhesion to Tissue. *Polymers (Basel).* **11**, 942 (2019).

169. Moreira Lana, G. *et al.* Self-Adhesive Silicone Microstructures for the Treatment of Tympanic Membrane Perforations. *Adv. NanoBiomed Res.* **1**, 2100057 (2021).

170. Davis, C. S., Martina, D., Creton, C., Lindner, A. & Crosby, A. J. Enhanced adhesion of elastic materials to small-scale wrinkles. *Langmuir* **28**, 14899–14908 (2012).

171. Persson, B. N. J., Albohr, O., Creton, C. & Peveri, V. Contact area between a viscoelastic solid and a hard, randomly rough, substrate. *J. Chem. Phys.* **120**, 8779–8793 (2004).

172. Arzt, E., Quan, H., McMeeking, R. M. & Hensel, R. Functional surface microstructures inspired by nature – From adhesion and wetting principles to sustainable new devices. *Prog. Mater. Sci.* **119**, 1–105 (2021).

173. Eisenhaure, J. & Kim, S. A review of the state of dry adhesives: Biomimetic structures and the alternative designs they inspire. *Micromachines* **8**, 1–38 (2017).

174. Cutting, K. F. Impact of adhesive surgical tape and wound dressings on the skin, with reference to skin stripping. *J. Wound Care* **17**, (2013).

175. Zulkowski, K. Understanding moisture-associated skin damage, medical adhesive related skin injuries and skin tears. *Adv. Ski. wound care* **30**, 372–381 (2017).

176. Drotlef, D. M., Amjadi, M., Yunusa, M. & Sitti, M. Bioinspired Composite Microfibers for Skin Adhesion and Signal Amplification of Wearable Sensors. *Adv. Mater.* **29**, 1–8 (2017).

177. Bae, W. G. *et al.* Enhanced Skin Adhesive Patch with Modulus-Tunable Composite Micropillars. *Adv. Healthc. Mater.* **2**, 109–113 (2013).

178. Noderer, W. L. *et al.* Enhanced adhesion and compliance of film-terminated fibrillar surfaces. *Proc. R. Soc. A Math. Phys. Eng. Sci.* **463**, 2631–2654 (2007).

179. Boyadzhieva, S. *et al.* A self-adhesive elastomericwound scaffold for sensitive adhesion to tissue. *Polymers (Basel).* **11**, 1–15 (2019).

180. Korn, V., Surber, C. & Imanidis, G. Skin Surface Topography and Texture Analysis of Sun-Exposed Body Sites in View of Sunscreen Application. *Skin Pharmacol. Physiol.* **29**, 291–299 (2017).

181. Adabi, S. *et al.* Universal in vivo Textural Model for Human Skin based on Optical Coherence Tomograms. *Sci. Rep.* **7**, 1–12 (2017).

182. Jones, I., Currie, L. & Martin, R. A guide to biological skin substitutes The function of normal skin. *Br. J. Plast. Surg. Br. Assoc. Plast. Surg.* **55**, 185–193 (2002).

183. Bai, Y., Jagota, A. & Hui, C. Y. Frictional auto-roughening of a surface with spatially varying stiffness. *Soft Matter* **10**, 2169–2177 (2014).

184. Kroner, E., Blau, J. & Arzt, E. Note: An adhesion measurement setup for bioinspired fibrillar surfaces using flat probes. *Rev. Sci. Instrum.* **83**, 2–5 (2012).

185. Eubel, J. M. Design und Herstellung eines Haftsystem zur Anwendung auf dem Trommelfell. (Universität des Saarlandes, 2019).

186. Koenig, D. W., Dvoracek, B. & Vongsa, R. In vitro prediction of in vivo skin damage associated with the wiping of dry tissue against skin. *Ski. Res. Technol.* **19**, 453–458

(2013).

187. Chen, S. & Bhushan, B. Nanomechanical and nanotribological characterization of two synthetic skins with and without skin cream treatment using atomic force microscopy. *J. Colloid Interface Sci.* **398**, 247–254 (2013).

188. Sanner, A., Nöhring, W. G., Thimons, L. A., Jacobs, T. D. B. & Pastewka, L. Scale-dependent roughness parameters for topography analysis. *Appl. Surf. Sci. Adv.* **7**, (2022).

189. Jacobs, T. D. B., Junge, T. & Pastewka, L. Quantitative characterization of surface topography using spectral analysis. *Surf. Topogr. Metrol. Prop.* **5**, (2017).

190. Wang, A. & Müser, M. H. On the usefulness of the height-difference-autocorrelation function for contact mechanics. *Tribol. Int.* **123**, 224–233 (2018).

191. Dassault Systems, S. C. ABAQUS 6.14 Documentation. (2014).

192. Stark, S., Begley, M. R. & McMeeking, R. M. The buckling and postbuckling of fibrils adhering to a rigid surface. *J. Appl. Mech. Trans. ASME* **80**, (2013).

193. Kroner, E., Paretkar, D. R., McMeeking, R. M. & Arzt, E. Adhesion of flat and structured PDMS samples to spherical and flat probes: A comparative study. *J. Adhes.* **87**, 447–465 (2011).

194. Kruttwig, K., Moreira Lana, G., Moh, K. & Arzt, E. Krafttollerante Struktur DE10 2021 103 895.2. Priority Date 18.01.2021.

195. Purtov, J., Frensemeier, M. & Kroner, E. Switchable Adhesion in Vacuum Using Bio-Inspired Dry Adhesives. *ACS Appl. Mater. Interfaces* **7**, 24127–24135 (2015).

196. Paretkar, D. *et al.* Bioinspired pressure actuated adhesive system. *Mater. Sci. Eng. C* **31**, 1152–1159 (2011).

197. Wang, A. & Müser, M. H. On the adhesion between thin sheets and randomly rough surfaces. *Friction* (2022) doi:doi.org/10.1007/s40544-022-0644-3.

198. Charyulu, M. K. Theoretical stress distribution in an elastic multi-layered medium. *PhD Dissertation* (1964).

199. Kajita, S. Green's function nonequilibrium molecular dynamics method for solid surfaces and interfaces. *Phys. Rev. E* **94**, 1–9 (2016).

200. Sainsot, P. Analytical stresses in rough contacts. *Proc. Inst. Mech. Eng. Part C J. Mech. Eng. Sci.* **225**, 274–279 (2011).

201. Müller, C. & Müser, M. H. Analytical and numerical results for the elasticity and adhesion of elastic films with arbitrary Poisson's ratio and confinement. *J. Adhes.* **00**, 1–24 (2022).

202. Carbone, G., Lorenz, B., Persson, B. N. J. & Wohlers, A. Contact mechanics and rubber friction for randomly rough surfaces with anisotropic statistical properties. *Eur. Phys. J. E* **29**, 275–284 (2009).

203. Martina, D., Creton, C., Damman, P., Jeusette, M. & Lindner, A. Adhesion of soft viscoelastic adhesives on periodic rough surfaces. *Soft Matter* **8**, 5350–5357 (2012).

204. Kwak, M. K. *et al.* Towards the next level of bioinspired dry adhesives: New designs and applications. *Adv. Funct. Mater.* **21**, 3606–3616 (2011).

205. Tinnemann, V. *et al.* In Situ Observation Reveals Local Detachment Mechanisms and Suction Effects in Micropatterned Adhesives. *Adv. Funct. Mater.* **29**, (2019).

206. Noderer, W. L.; Shen, L.; Vajpayee, S.; Glassmaker, N. J.; Jagota, A. and Hui, C.-Y. Enhanced adhesion and compliance of film-terminated fibrillar surfaces. *Proc. R. Soc. A* 2631–2654 (2007).

207. Shahsavan, H., Arunbabu, D. & Zhao, B. Biomimetic modification of polymeric surfaces: A promising pathway for tuning of wetting and adhesion. *Macromol. Mater. Eng.* **297**, 743–760 (2012).

208. Dursun, E. *et al.* Comparison of paper-patch, fat, and perichondrium myringoplasty ın repair of small tympanic membrane perforations. *Otolaryngol. - Head Neck Surg.* **138**, 353–356 (2008).

209. Berger, G., Finkelstein, Y., Avraham, S. & Himmelfarb, M. Patterns of hearing loss in non-explosive blast injury of the ear. *J. Laryngol. Otol.* **111**, 1137–41 (1997).

210. Mehta, R. P., Rosowski, J. J., Voss, S. E., O'Neil, E. & Merchant, S. N. Determinants of hearing loss in perforations of the tympanic membrane. *Otol. Neurotol.* **27**, 136–143 (2006).

211. Sogebi, O. A., Oyewole, E. A. & Mabifah, T. O. Traumatic tympanic membrane perforations: characteristics and factors affecting outcome. *Ghana Med. J.* **52**, 34–40 (2018).

212. Louw, L. Acquired cholesteatoma pathogenesis: Stepwise explanations. *J. Laryngol. Otol.* **124**, 587–593 (2010).

213. Santa Maria, P. L. *et al.* Functional Outcomes of Heparin-Binding Epidermal Growth Factor-Like Growth Factor for Regeneration of Chronic Tympanic Membrane Perforations in Mice. *Tissue Eng. Part A* **23**, 436–444 (2017).

214. Janssen, T., Niedermeyer, H. P. & Arnold, W. Diagnostics of the cochlear amplifier by means of distortion product otoacoustic emissions. *ORL* **68**, 334–339 (2006).

215. Zhao, F., Wada, H., Koike, T. & Stephens, D. The influence of middle ear disorders on otoacoustic emissions. *Clin. Otolaryngol.* **25**, 3–8 (2000).

216. Tlumak, A. I. & Kileny, P. R. Parameters that affect the measurement of otoacoustic

emissions. *Curr. Opin. Otolaryngol. Head Neck Surg.* **9**, 279–283 (2001).

217. LeBourgeois, H. W., Anand, V. K., McAuley, J. R., Dickman, J. D. & Malphurs, O. Effect of Tympanic Perforations on the Detection of Distortion-product Otoacoustic Emissions. *Ear, Nose Throat J.* **79**, 610–618 (2000).

218. Dong, W., Stomackin, G., Lin, X., Martin, G. K. & Jung, T. T. Distortion product otoacoustic emissions: Sensitive measures of tympanic -membrane perforation and healing processes in a gerbil model. *Hear. Res.* **378**, 3–12 (2019).

219. Zöllner, F. The principles of plastic surgery of the sound-conducting apparatus. *J. Laryngol. Otol.* **69**, 637–652 (1955).

220. Wullstein, H. Funktionelle Operationen im Mittelohr mit Hilfe des freien Spaltlappentransplantates. *Arch. für Ohren-, Nasen-, und Kehlkopfheilkd* 422–435 (1952).

221. Hempel, J. M. *et al.* Traumatic tympanic membrane perforations: Clinical and audiometric findings in 198 patients. *Otol. Neurotol.* **33**, 1357–1362 (2012).

222. Branica, S., Dawidowsky, K., Kovač-Bilić, L. & Bilić, M. Silicon foil patching for blast tympanic membrane perforation: A retrospective study. *Croat. Med. J.* **60**, 503–507 (2019).

223. Boyadzhieva, S. *et al.* Thin film composite silicon elastomers for cell culture and skin applications: Manufacturing and characterization. *J. Vis. Exp.* **2018**, 1–16 (2018).

224. Willott, J. F. Measurement of the Auditory Brainstem Response (ABR) to Study Auditory Sensitivity in Mice. *Curr. Protoc. Neurosci.* **34**, 8.21B.1-8.21B.12 (2006).

225. Rüttiger, L., Zimmermann, U. & Knipper, M. Biomarkers for Hearing Dysfunction: Facts and Outlook. *Orl* **79**, 93–111 (2017).

226. Sorg, K. *et al.* First biocompatibility margins for optical stimulation at the eardrum via 532-nm laser pulses in a mouse model. *J. Biomed. Opt.* **24**, 1 (2019).

227. Schacht, S. A. L., Stahn, P., Hinsberger, M., Schick, B. & Wenzel, G. I. Laser-induced tissue remodeling within the tympanic membrane. *J. Biomed. Opt.* **23**, 1 (2018).

228. Zheng, Q. Y., Johnson, K. R. & Erway, L. C. Assessment of hearing in 80 inbred strains of mice by ABR threshold analyses. *Hear. Res.* **130**, 94–107 (1999).

229. Hecker, D. J. *et al.* A new method to analyze distortion product otoacoustic emissions (DPOAEs) in the high-frequency range up to 18 KHZ using windowed periodograms. *IEEE Trans. Biomed. Eng.* **58**, 2369–2377 (2011).

230. Engel, J. *et al.* Two classes of outer hair cells along the tonotopic axis of the cochlea. *Neuroscience* **143**, 837–849 (2006).

231. Schimmang, T. *et al.* Lack of Bdnf and TrkB signalling in the postnatal cochlea leads to

a spatial reshaping of innervation along the tonotopic axis and hearing loss. *Development* **130**, 4741–4750 (2003).

232. Fell, B. *et al.* α2δ2 controls the function and trans-synaptic coupling of cav1.3 channels in mouse inner hair cells and is essential for normal hearing. *J. Neurosci.* **36**, 11024–11036 (2016).

233. Caminos, L., Garcia-Manrique, J., Lima-Rodriguez, A. & Gonzalez-Herrera, A. Analysis of the mechanical properties of the human tympanic membrane and its influence on the dynamic behaviour of the human hearing system. *Appl. Bionics Biomech.* **2018**, (2018).

234. ISO. Self adhesive tapes - determination of peel adhesion properties. *www.iso.org* 20 (2007).

235. ISO. Self adhesive tapes - Measurement of peel adhesion from stainless steel or from its own backing. 22 (1997).

236. Mikolaszek, B., Kazlauske, J., Larsson, A. & Sznitowska, M. Controlled Drug Release by the Pore Structure in Polydimethylsiloxane Transdermal Patches. *Polymers (Basel).* **12**, 1520 (2020).

237. Yu, K. *et al.* A cochlear implant loaded with dexamethasone and coated with hyaluronic acid to inhibit fibroblast adhesion and proliferation. *J. Drug Deliv. Sci. Technol.* **46**, 173–181 (2018).

238. Blankenship, C. M. *et al.* Optimizing clinical interpretation of distortion product otoacoustic emissions in infants. in *Ear and Hearing* vol. 39 1075–1090 (Lippincott Williams and Wilkins, 2018).

239. Colon, D. *et al.* Early indication of noise-induced hearing loss from PMP use in adolescents: A cross-sectional analysis. *Noise Heal.* **18**, 288–296 (2016).

240. Ohlms, L. A., Lonsbury-Martin, B. L. & Martin, G. K. The clinical application of acoustic distortion products. in *Otolaryngology - Head and Neck Surgery* vol. 103 52–59 (1990).

241. Amadasun, J. E. O. An observational study of the management of traumatic tympanic membrane perforations. *J. Laryngol. Otol.* **116**, 181–184 (2002).

242. Lou, Z., Wang, Y. & Su, K. Comparison of the healing mechanisms of human dry and endogenous wet traumatic eardrum perforations. *Eur. Arch. Oto-Rhino-Laryngology* **271**, 2153–2157 (2014).

243. Saliba, I. Hyaluronic acid fat graft myringoplasty: How we do it. *Clinical Otolaryngology* vol. 33 610–614 (2008).